UNIVERSITY OF OKLAHOMA

GRADUATE COLLEGE

SEISMIC ATTRIBUTE ANALYSES AND ATTENUATION APPLICATIONS FOR DETECTING GAS HYDRATE PRESENCE

A THESIS

SUBMITTED TO THE GRADUATE FACULTY

in partial fulfillment of the requirements for the

Degree of

MASTER OF SCIENCE

By

ROBERTO DOMINIC CLAIRMONT

Norman, Oklahoma

2021

SEISMIC ATTRIBUTE ANALYSES AND ATTENUATION APPLICATIONS FOR DETECTING GAS HYDRATE PRESENCE

A THESIS APPROVED FOR THE

SCHOOL OF GEOSCIENCES

BY THE COMMITTEE CONSISTING OF

Dr. Heather Bedle. Chair

Dr. Yichuan Wang

Dr. Kurt Marfurt

To Robert and Cherylin: the pillars to my strength

ACKNOWLEDGEMENTS

My graduate journey began with a lot of doubt. However, I kept my ambition, my faith and above all, my love for the geosciences and where I saw myself wanting to be. These last 2 years reminded me of all that I have desired to achieve and the type of person I want to become. Being away from home, for so long has not been easy, but I am grateful for the long list of people that have made my journey exciting and memorable.

I want to express my dearest appreciation to my advisor Dr. Heather Bedle. You have made my graduate experience at OU a great and rewarding one. Although you had an idea of where my heart lies in geosciences, you gave me the opportunity to join you as a graduate student and I have only been aiming for the sky ever since. You have allowed me to explore my scientific curiosity which has helped to expand my knowledge and creativity, and for that I am very grateful for you. Thank you for allowing me to put my well-being first and encouraging me to take care of myself throughout it all.

I want to also express a sincere thank you to my committee members. Thank you Dr. Kurt Marfurt for seeing something in me and allowing me to have such a memorable and accomplished graduate student experience. I admire what you have done for many students before me, especially with respect to diversifying the graduate student group in the School of Geosciences. Thank you Dr. Yichuan Wang, for not only allowing me to use your software coding for my thesis work, but for trying your best to support and assist me given the unfortunate circumstances as a result of the pandemic.

I would like to thank Jake Walter of the OGS for helping me ignite an interest in research which led to my passion to pursue graduate school. That 2018 summer internship under your supervision is an important experience that I am delighted to have had.

To my friend and mentor, Folarin Kolawole, thank you very much. You have helped me tremendously to become a better scientist and researcher. Thank you for sharing your passion, drive and knowledge with me; for being selfless, dedicated and a great motivator.

I would like to thank the SDA and AASPI crew for sharing their love, passion and knowledge for the field of geosciences. Thank You, Laura Ortiz, Jose Pedro, Edimar Perico, Alex Vera, Clayton Silver, Julian Chenin, Javier Tellez, Chris Ramos, Carl Buist, David Lubo, Francis Oyebanji, Abidin Caf, Rafael Pires, Zach Williams, Karelia La-Marca. Especially, for all of your constructive feedback.

To my OU friends, Sheridan Mullen, Christina Hamilton, Tanner Shadoan, Delcio Teixeira, Tara Putri, Anna Mbowa, Yara Almilaify, Jamalje Bassue, Hussain Hassan, Nishit Garg, Dalila de Jesus, Visal So, Adnan Solanki (the list does not end here); you all have made my entire 6 years at OU enjoyable, memorable and full of laughter.

I would also like to show much appreciation to the administration team on the 7th floor of the School of Geosciences, including Ashley, Ginger and Leah. A much special appreciation for Rebecca who has been exceedingly helpful and for going out of her way to assist me in more ways than one. Thank You.

To my best friend Derryck Joseph, thanks for surviving without me back home in Trinidad and Tobago for the last 6 years. It has been tough living here without my dear friend and brother

but I know we will always keep the friendship strong. Thank you for being a part of my life, and for welcoming me to your family.

To my “Texas family”, as my mother would say; Barbara, Collin, Tom and Katherine Kennedy, my time here in Oklahoma has been immensely better than one would expect because of you. I appreciate every single thing you all have done for me, from the moment I experienced my first Thanksgiving with you in 2015, to today as I write this. You made your home, my home away from home and I could not ask for more, yet there has always been more. Thank You.

Finally, as I thank my family and my loved ones, I would love to express my deepest gratitude and undying love to my parents. My mother Cherylin and my father Robert. There are no words capable to describe the traits that you both embody and if there are, those words will not do justice. I am highly blessed and favored for having you two in my life, what a blessing.

To journey beyond the extraordinary, is to be blessed with people that are extraordinary.

TABLE OF CONTENTS

LIST OF FIGURES

LIST OF TABLES

ABSTRACT

Although regions of continental margins that consist of subduction zones are not currently prospects for the exploration of oil and gas; they do host a large proportion of the global accumulation of methane hydrates. The last several decades have witnessed an accelerated interest in gas hydrates for multiple reasons. Before our concerns about globing warning, hydrates were thought to be an untapped hydrocarbon resource. Some scientist fear that ocean warming could release methane in these hydrates into the atmosphere, further contributing to climate change. Whether we wish to place offshore oil production platforms, CO_2 sequestration wells, or offshore windmills, gas hydrates and their associated free gas can pose geohazard risks that need to be understood and minimized. Many of these studies have used both well and seismic data among other data types to infer gas hydrates in the subsurface of continental deep-water environments for potential energy exploration. One of the most common ways to detect gas hydrates using seismic data, is via a bottom-simulating reflector (BSR) which indicates the transition of seismic waves from gas hydrate-bearing sediments of the gas hydrate stability zone (GHSZ) to free gas or water filled sediments below due to an attenuation response. Unfortunately, the presence of a BSR does not always indicate the presence of hydrates, nor does the lack of a BSR indicate the absence of hydrates. Because several of these studies that use seismic reflection data do not use a direct measurement for attenuation, the main motivation of this research is to apply a recently developed method that directly measures the seismic attenuation response to help delineate gas hydrates such settings.

Utilizing 2D seismic reflection data acquired in the Pegasus Basin, east of central New-Zealand, I apply attribute analyses using frequency attributes that are traditionally known to image BSRs and indirectly infer attenuation. The attribute analysis was followed by a spectral

decomposition method (continuous wavelet transform) that is expected to perform a better job. Finally, I use a Sparse-Spike Decomposition (SSD) to quantitatively estimate seismic attenuation. I show that while SSD does not directly indicate gas hydrate presence, the attenuation response associated with free gas beneath the GHSZ indicates an overlying gas hydrate or other type of seal.

CHAPTER 1: INTRODUCTION

For the last couple of decades, the academic and industrial community have become even more curious with the potential role of methane/gas hydrates in the petroleum industry. It was only in the late 20th century, specifically the 1990s when naturally occurring methane hydrates were explored for economic gain. So what are gas hydrates? Gas hydrates are naturally occurring trapped biogenic or thermogenic deposits within a crystalline lattice of hydrogen bonded water molecules, with the most common type of molecule within the lattice structure, being that of methane (Sloan, 2003). The physical properties that contribute to their formation in low temperatures and high pressure conditions are linked to their natural occurrences in permafrost and the shallow subsurface of continental deep-water sediments. More specifically, gas hydrate presence within the subsurface, exists in a specific depth zone controlled by these pressure-temperature conditions that follow a "hydrate-water" equilibrium curve. This zone is well known as the Gas Hydrate Stability Zone (GHSZ), and lies between the ocean-bottom interface and the depth at which the geotherm intersects the methane-hydrate water equilibrium curve (See Figure 1-1)

Seismic data often identifies the presence of methane hydrates via a natural phenomenon known as a Bottom-Simulating Reflector (BSR). The BSR is a strong seismic reflector with a negative polarity to that of the seabed, often mimicking its trend and represents the transition from partially hydrate filled sediments to a zone of gas filled and/or water-filled sediments (Singh, 1993). The occurrence of this natural phenomenon has been explored by many seismic interpreters, in applications concerning seismic attribute analyses, spectral decomposition, machine-learning, VSP (vertical seismic profile) analyses and rock physics modeling to name a few. Unfortunately,

the relationship between BSRs and hydrate isn't always consistent, since the presence of the former in seismic data does not always suggest gas hydrate in the subsurface, neither does its absence suggest the absence of hydrates. Alternative methods are therefore crucial to understand gas hydrates.

A combination of laboratory studies together with the aforementioned seismic applications, reveal that the BSRs are associated with the attenuation of the seismic signal influenced by the GHSZ. The apparent changes in the porosity of sediments from a less porous hydrate bearing medium (i.e. the GHSZ) to a more porous non-hydrate medium affects the propagation of the seismic wave. Therefore, the goal of this research is to improve and hence determine whether we can infer gas hydrate presence within the subsurface, using an attenuation-estimation method termed Sparse-Spike Decomposition, on the premise of wavelet estimation developed by Wang and Morozov (2020). This method uses statistical wavelet estimation from seismic traces via the sparse spike decomposition to quantitatively measure attenuation using the quality factor, Q (Wang et al., 2021). Additionally, to aid our inferences of gas hydrates, we apply frequency-related seismic attributes and continuous wavelet transform (i.e. a spectral decomposition method) to better discern the BSRs and provide a more complete and integrated analysis. This is the main focus of Chapter 2.

This research explores the relationship between potential attenuation of seismic signals associated with zones of gas hydrate and free gas accumulation by adhering to several objectives.

1. To improve the detection of BSRs within seismic data.
2. To measure and observe the attenuation response of hydrate systems in specific zones of interest by identifying BSRs based on observational seismic amplitude responses. Therefore, for this study we define and focus on a; (a) Strong-Continuous BSR (SC-BSR)

(Figure 1-2a); (b) Weak-Discontinuous BSR (WD-BSR) (Figure 1-2b); and (c) a Very-Strong Continuous BSR (VSC-BSR) (Figure 1-2c).

3. Identify any similarities/differences when comparing the results of seismic attributes, spectral decomposition method, and the attenuation measurement.
4. Improve the inference of free gas distribution and accumulation in addition to hydrates, using the attenuation method.
5. Observe whether this method can work well in other areas of interests to determine the presence of gas hydrates and free gas accumulation.

REFERENCES

Ruppel, C. D., & Kessler, J. D. (2017). The interaction of climate change and methane hydrates: Climate-Hydrates Interactions. Reviews of Geophysics, 55(1), 126–168. https://doi.org/10.1002/2016RG000534.

Singh, S. C., Minshull, T. A., & Spence, G. D. (1993). Velocity Structure of a Gas Hydrate Reflector. Science, 260(5105), 204–207. https://doi.org/10.1126/science.260.5105.204.

Sloan, E. D. (2003). Fundamental principles and applications of natural gas hydrates. Nature, 426(6964), 353–359. https://doi.org/10.1038/nature02135. Wang, Y., & Morozov, I. B. (2020). A simple approach to nonstationary source waveform estimation in seismic records. GEOPHYSICS, 85(3), V257–V268. https://doi.org/10.1190/geo2019-0133.1.

Wang, Y., & Morozov, I. B. (2020). A simple approach to nonstationary source waveform estimation in seismic records. GEOPHYSICS, 85(3), V257–V268. https://doi.org/10.1190/geo2019-0133.1.

Wang, Y., Morozov, I.B., Bedle, H., & Marfurt, K. J. (2021). Seismic attenuation measurement using sparse strongest reflections in seismic images, submitted to Geophysics, in review.

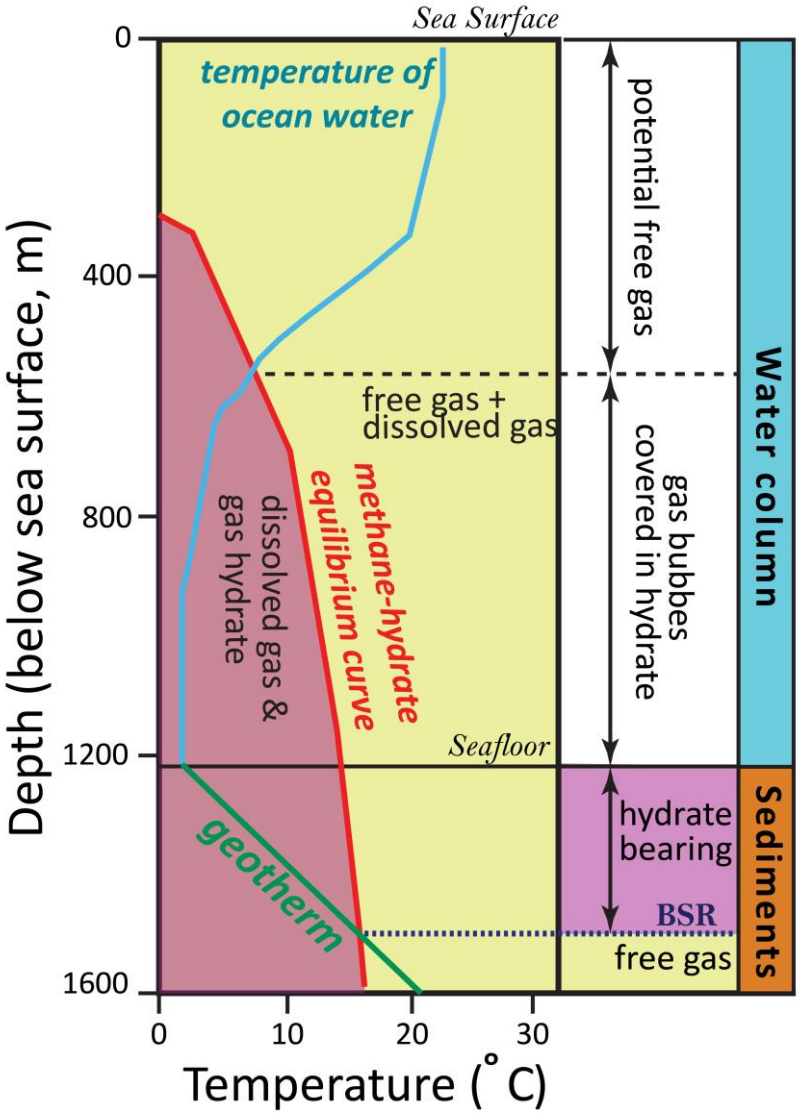

Figure 1-1. Pressure and temperature curves and the associated gas hydrate systems for deep-water marine settings after (Ruppel and Kessler, 2017). The yellow regions define the potential presence of a combination of dissolved gas and free gas, whereas the magenta regions describe the potential presence of gas hydrates with dissolved gas. The BSR is defined as the bottom-simulating reflector which marks the boundary between the hydrate bearing sediments and underlying free gas bearing sediments.

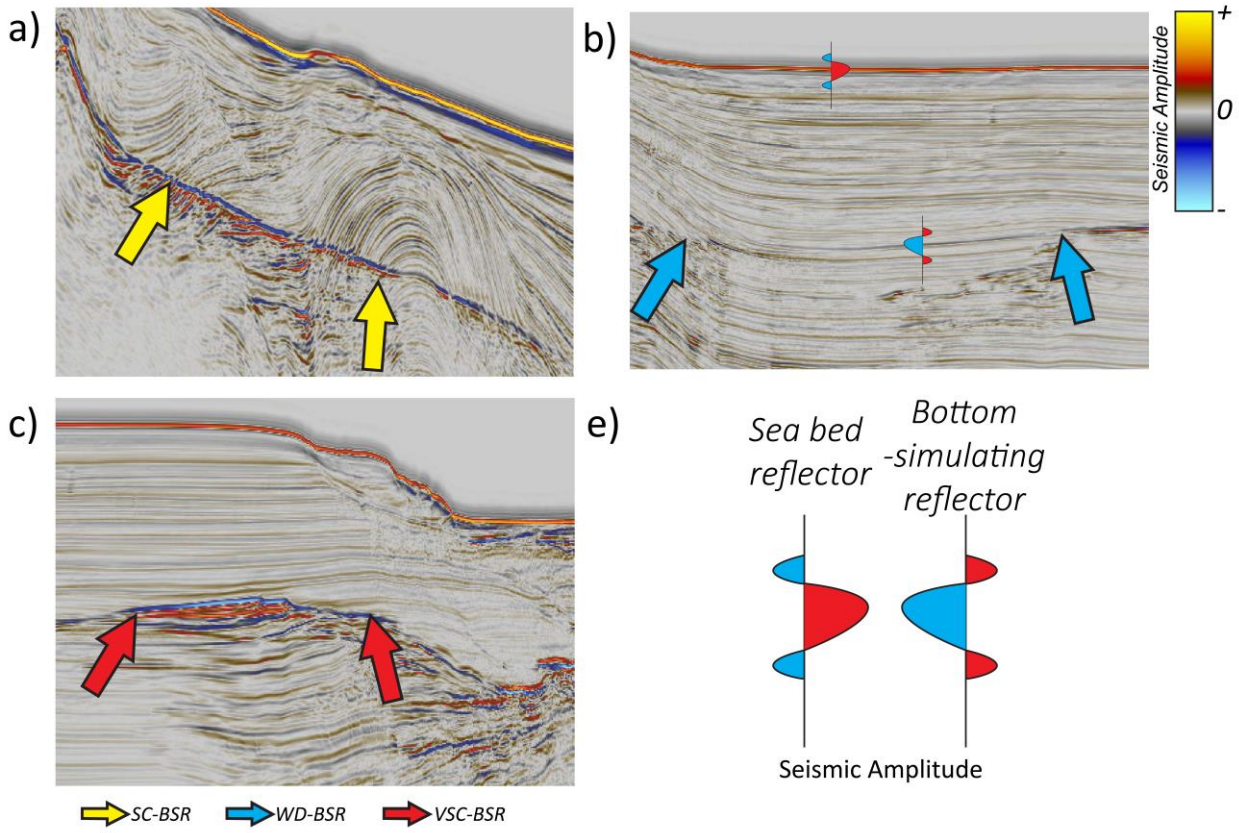

Figure 1-2. Seismic line of the inferred (a) SC-BSR, (b) WD-BSR and (c) VSC-BSR. Notice that the BSRs can cut across stratigraphic layers and (e) has an opposite polarity to that of the sea-bed's seismic amplitude.

CHAPTER 2: SEISMIC ATTRIBUTE ANALYSES AND ATTENUATION APPLICATIONS FOR DETECTING GAS HYDRATE PRESENCE

ABSTRACT

Identifying gas hydrates in the oceanic subsurface using seismic reflection data supported by the presence of a bottom simulating reflector (BSR) is not an easy task, given the wide range of geophysical methods that have been applied to do so. Though the presence of the BSR is attributed to the attenuation response as seismic waves transition from hydrate-filled sediment within the gas hydrate stability zone (GHSZ) to free gas bearing sediment below, few studies have applied a direct attenuation measurement. To improve the detection of gas hydrates and associated features, including the BSR and free gas accumulation beneath the GHSZ, we apply a recently developed method known as Sparse-Spike Decomposition (SSD) that directly measures attenuation from estimating the quality factor (Q) parameter. In addition to performing attribute analyses using frequency attributes and a spectral decomposition method to improve BSR imaging, using a comprehensive analysis of the three methods, we make several key observations. These include: (1) low frequency shadow zones seem to correlate with large values of attenuation; (2) a strong relationship between the amplitude strength of the BSR and the increase of the attenuation response; (3) the interpretation of migration pathways of the free gas using the direct attenuation measurement method; and (4) for the data analyzed, the gas hydrate stability zone itself does not give rise to either impedance or attenuation anomalies that differentiate it from nearby non-hydrate zones. From this last observation, we find that although the SSD method may not directly detect in situ gas hydrates, the same gas hydrates often form an effective seal trapping deeper free gas accumulation which can exhibit a large attenuation response, allowing us to infer the likely presence of the overlying hydrates themselves

INTRODUCTION

Gas hydrates have been gaining quite a lot of momentum in the academic and industrial climate within the last few decades, primarily with respect to its role in the petroleum industry. These gas hydrates, which commonly contain methane gas, are naturally occurring trapped biogenic or thermogenic (Dev & McMechan, 2010) molecules within a crystalline lattice of hydrogen bonded water molecules with most being of biogenic origin (Sloan, 2003). The bioegenic component involves the biodegradation of plant and animal matter buried in the low temperature environment of the seabed. Furthermore, gas hydrates can be defined by three types of chemical structures (i.e. I, II and H), with methane being a main precursor of structure I, which depend on the sizes of the trapped gas molecules (Sloan, 2003; Maslin et al., 2010; Matsumoto et al., 2011). Experiments show that the formation of gas hydrates occurs once the conditions of pressure and temperatures are within what is known as the hydrate stability zone (Dickens & Quinby-Hunt, 1994; Ghiassian & Grozic, 2013), observed in temperature-pressure phase diagrams produce by Dickens & Quinby-Hunt (1994). Beneath this "gas" hydrate stability zone (GHSZ) seismic data can potentially mark the transition via a strong seismic reflector, from partially hydrate filled sediments to a zone of partially gas-filled and/or water-filled sediments (Singh et al., 1993) via a Bottom-Simulating Reflector (BSR). The physical properties that govern their formation in low-temperatures and high pressure conditions are linked to their natural occurrence in permafrost, and the shallow subsurface of continental deep-water environments at depths of up to 500 meters where this BSR can be observed in seismic reflection data. Unfortunately, due to the specific temperature-pressure regimes required to keep gas hydrates in their solid form, any alterations to this can affect the stability of the sea floor and surrounding lithology, creating potential drilling hazards (Diaconescu & Knapp, 2002; Faure et al., 2006)

Implications of gas hydrates

The occurrence of methane hydrates plays an important role in the organic carbon cycle and the effects on global climate. Since methane is a known greenhouse gas which can be oxidized within a time period of a decade into CO_2, there is an alarming impact on the contribution to climate change. Near the bottom of the GHSZ, global warming can influence temperatures of the hydrates to arrive at their melting point within the deep ocean setting (Archer et al., 2009). Melting of these hydrate reservoirs which accelerates the dissolution of the methane and the oxidation process into CO_2, can release about 15-20% of the carbon into the atmosphere (Archer et al., 2009). Additionally, methane hydrates are observed to be a main component in the global carbonic cycle, acting as both a source and a sink for carbon molecules (Kvenvolden, 2002). Although the evidence is convincing, there remains some uncertainty as to the amount of carbon that methane hydrates contribute (Kvenvolden 2002). Therefore, further analysis on terrestrial and marine records will be important to understanding the role of methane hydrates in global climate change (Kvenolden, 2002). Though it may not be a direct contribution to the carbon input, it is also important to mention the potential for escaped methane gas to affect water resources on land, as a result of drilling and hydraulic fracturing. Osborn et al. (2011) showed a correlation between higher concentrations of methane revealed in a significant number of shallow water sources near active drilling natural-gas wells compared to inactive locations, in New York and Pennsylvania.

There is a clear role of methane hydrates in energy industry. Although, regions comprising of continental margins with subduction zones are not, at present, typical prospective regions for oil and gas exploration, these zones host a significant portion of the global supply of methane hydrates (Kroeger et al., 2015). As hydrocarbons are molecules that comprise of different arrangements of bonding between hydrogen and carbon molecules, methane (CH_4) is the simplest

molecule of hydrocarbon that exists, and is chemically stable without the presence of oxygen. This has made it an interesting potential energy resource. One example of the role of gas hydrates in petroleum industry is the 1967 discovery of the Messovakha gas-hydrate field in eastern Siberia. The field showed gas hydrate deposits within a sandy-argillaceous stratum of Middle-Jurassic, Lower and Upper-Cretaceous Paleocene age sediment (Makogen et al., 2007). The Messovakha Field study highlighted the negative environmental impacts in which the climatic carbon footprint can experience elevated levels; the potential for these compounds to be exploited as cleaner sources of energy production, and the effects methane gas emission from the hydrate lattice can have on surrounding sediment stability.

Detecting gas hydrates in the subsurface

As aforementioned, the accumulation of gas hydrates can be discerned in seismic reflection data by anomalous shallow seismic events, termed BSRs that often mimic the trend of the seafloor. BSRs are associated with two types of phenomenon. One is associated with diagenetic boundaries in siliceous sediments, the other is as a result of a negative impedance contrast caused by the transition from the GHSZ (gas hydrate bearing sediments) to the underlying free-gas bearing sediments (Shedd et al., 2012). This common approach of discerning the BSR, is often distinct from the background geology, such that it follows a reflection with a reversed or "negative" polarity to that of the seafloor, and in most cases cross-cuts natural stratigraphic units (Matsumoto et al., 2011). Many studies have been performed on seismic data that have noted that BSRs are not always present in regions where hydrates exist in the GHSZ (Shedd et al., 2012; Hillman et al., 2017; Kroeger et al., 2017). Due to the elusive nature of definitively detecting the presence of

BSRs in seismic reflection data, multiple alternative geophysical methods need to be applied to determine the presence of gas hydrates in deep marine environments.

Previous studies that utilize seismic data

Before we explore the method of attenuation performed in this study, we must first recognize some of the contributions by seismic interpreters in both the attempt and the likely success of improving the interpretation and relationships between BSRs and accumulation of hydrate systems. We observe studies on the hydrate systems associated with strong amplitude continuous BSRs and those of weak amplitude discontinuous BSRs.

Strong, continuous BSRs

The first indication of a BSR in seismic data of continental margins before drilling, located at the Blake-Bahama Outer Ridge (Blake-Ridge) along the east coast of the United States, was initially interpreted as either an erosional surface or diagenetic boundary (Markl et al., 1970). It was further explained that this high amplitude BSR response can be directly related to an accumulation of gas beneath the hydrate bearing sediment zone (Bryan, 1974). Since then many studies have used the presence of the BSR along seismic profiles to support their findings on hydrate accumulation. Continuous BSRs can be described as a continuous coherent anomalous reflector that mimics the seafloor whilst cross cutting stratigraphic units (Shedd et al., 2012). Paganoni et al. (2016) observed the presence of gas hydrate from cores above (structure I) and below (structure II) an identified BSR in seismic, in which this interval also correlated with high resistivity well log data. With the use of a gas hydrate model, one major conclusion of their work suggests that the BSR can also represent the boundary that separates two different hydrate

structures contrary to the expected free gas sediments that many studies have agreed on. Vadakkepuliyambatta et al. (2017) inferred gas accumulation associated with hydrate dissociation of a likely thermogenic source, in addition to interpreting vertical fluid flow of gas chimneys in the seismic reflection data, contributing to the BSR presence. They performed a gas hydrate stability model using bottom-water temperature data to observe the relationship between seasonal alteration in water temperature and the variation in thickness of the GHSZ as a measure of hydrate stability. The aforementioned studies highlight a few of the subsurface characteristics associated with strong-continuous BSRs observed in seismic.

Weak-discontinuous BSRs

Like strong continuous BSRs, weak-discontinuous BSRs can also cross cut stratigraphic units and parallels the seafloor, and can additionally be recognized in seismic as widely spaced seismic events (Shedd et al., 2012) and generally occur within heterogeneous units (Shedd et al., 2012; Hillman et al., 2016). Few studies discuss the importance of the influence that seismic resolution, a result of the source, and acquisition set up can have on imaging BSRs in the subsurface (Wood et al., 2008). In addition to these two factors, Hillman et al. (2017) highlights that the differences in BSR imaging can be controlled by, the occurrence of gas hydrate and free gas and lithological distribution of the formation. The study which compares three distinct seismic datasets reasons that BSRs actually occur discontinuous in nature (Hillman et al., 2017). Irrespective of physical properties, processing with higher fold data, low-frequency shadows can be detected for free-gas inference, as BSRs can be better imaged and characterized having stronger reflections (Alajmi et al., 2020). Together with seismic, hydrate systems models reveal that

discontinuous BSRs are a composite of structure I gas hydrates and can be related to a strongly microbial gas generated source (Kroeger et al., 2017).

Advanced studies of BSRs and gas hydrate relationship

In the case of geophysical techniques, one of the main goals is to determine the presence of gas hydrates within the subsurface with maximum probability, by improving the imaging of the BSR. There are many continuing and promising attempts employed to advance our interpretations and improve the efficiency in exploring for this natural resource. Multi-attribute analysis involving principle component analysis and self-organizing maps of sets of seismic attributes improve the imaging of the BSR, that potentially aids to identifying the occurrence of gas hydrates (Chenin & Bedle, 2020). Furthermore, instantaneous attributes when grouped for self-organizing map clustering better detect strong and weak BSRs, whereas AVA attributes seem to improve discontinuous BSR detection (Chenin & Bedle, 2020). Additionally, Lee et al. (2017) conducted a multi-attribute analysis using the unsupervised K-means clustering algorithm, in addition to acoustic impedance and shear impedance inversion models, to estimate the extent and distribution of a gas hydrate reservoir. Estimations without the use of well logs included well known AVO (Amplitude Versus-Offset) equations (Lee et al., 2017). In another AVO based study, Bedle (2019) combined rock physics modeling with seismic attribute analysis to demonstrate that far angle stack seismic data and a fluid factor attribute revealed the continuity of BSRs, in which full stack data and regular seismic amplitude did poorly in recognizing. This led to the conclusion that for the BSRs associated with the interpreted AVA Class 2n gas hydrates based on the rock physics modeling, subsurface imaging of "weak" or "unseen" BSRs can generally be improved with such method. Few studies have investigated the significance of the frequency aspect of the seismic

signal in relation to the presence of gas hydrates. Herein, we explore a comprehensive approach focused on the patterns of attenuation and therefore test methods that include frequency related seismic attributes, spectral decomposition and a direct attenuation measurement using the quality factor, Q.

Seismic Attenuation

Seismic attenuation describes the decay of energy of a propagating wave through a body of rock or medium within the subsurface. Whilst moving through the subsurface media, the wave can experience significant loss of energy due to factors of geometrical spreading, scattering and absorption. Evidently, amplitudes associated with high-frequency incident waves will attenuate faster than amplitudes associated with low frequency incident waves. Since gas hydrates can reduce the availability of porosity to a pore fluid, it can potentially increase the elastic moduli (Dvorkin et al., 2014) hence significantly stiffening the rock medium. Laboratory studies examine this rigidity of the rock medium to determine the strength of hydrate bearing sand grain/host sediments. Ghiassian & Grozic (2013) show that, according to measured maximum deviatoric stress value, the strength of gas hydrate sediments increased by a factor ranging between 1.8-3.6 as compared to the non-hydrate tests. Using a compressive strength test triaxial apparatus, hydrate saturated sandy sediments increase in strength with increasing pressure and temperature (Hyodo et al., 2011). With a similar type of experimental set up, Madhusudhan et al. (2019) showed the differences in strength gain of hydrate bearing sediments with varying particle sizes and surface areas, inferring a potential for a significant loss in the rock's integrity following hydrate dissociation. Together with the importance of knowing the grain size of the host sediment, this observation also compliments the potential geological hazards associated with the

dissociation/escape of hydrate from the pores of a rock medium. These apparent changes in the porosity also controlled by factors of hydrate pore-filling and compaction (Best et al., 2013) of sediments, induces an attenuation effect as the seismic wave propagates through one medium into the other. Seismic attenuation is therefore a crucial tool in indicating pore structure, fluid content and lithology (Klimentos, 1995; Li et al., 2016), and therefore plays an important role in the approach to discerning BSRs.

Applied Seismic Methods

Frequency attributes

Together with well log correlation, seismic attribute analyses are important tools to characterize the subsurface adjacently away from a well to identify seismic signatures and their petro-physical relationship. Frequency attributes in particular proved to show a relationship between gas hydrates and the seismic response. One of the earliest application of frequency attributes to discern gas hydrate presence was performed to interpret the Blake Ridge Diapir, Blake Ridge, located off the coast of South Carolina. The instantaneous frequency (IF) attribute revealed that low frequency signatures (also termed low-frequency shadow zones - LFSZs) coincide with free gas regions below BSRs with a strong seismic reflection, overlain by a hydrate bearing layer (Taylor et al., 2000). This attribute can be defined as the derivative of the instantaneous phase, which indicates time-dependent frequency information associated with the seismic trace. The instantaneous frequency is capable of highlighting the occurrence of high attenuation influenced by the free gas, in the event that the lithological layers above the BSR exhibit strong reflections

such that the velocity changes is quite significant (Taner et al., 1979; Taylor et al., 2000). It therefore aids in differentiating the gas hydrate bearing sediments from those sediments with pore filled free gas. Utilizing similar seismic attribute analyses, Kim et al. (2015) also discusses a low instantaneous frequency response within free gas regions capped by gas hydrate bearing sediments, however, revealing high instantaneous frequencies when the gas hydrate exists above a non-free gas region. We compute a couple frequency attributes, including instantaneous frequency to show the possibility that it may not always be accurate in its relationship with attenuation and hence gas hydrates. Additionally, since the instantaneous frequency responses do not clearly distinguish the BSRs, gas hydrate and/or free gas bearing sediments, in most cases, from that of the background geology, we perform a spectral decomposition to improve interpretation and analyses.

Spectral Decomposition

Time-frequency decomposition, or spectral decomposition is a method that decomposes seismic data into its frequency and phase components, in which the frequency component measures the relative seismic amplitude within a specific frequency band. The seismic data is transformed from its time to frequency domain. Naturally, its application provides an interpreter with the opportunity to resolve vertical variability in bed thickness (tuning thickness), such that thin beds have distinct characteristics in frequency domain, as well as other geological discontinuities (Partyka et al., 1999). There are a multitude of techniques that have performed the transformation of the recorded seismic traces from time (or depth) to frequency domain to obtain spectrally decomposed volumes. Some of these methods include continuous wavelet transform (Morlet et al. 1982; Goupillaud et al.1984), matching pursuit method (Liu & Marfurt, 2007) and wigner-ville distribution (Wigner, 1932; Auger et al., 1996), to name a few. Although, most

spectral decomposition techniques are designed to detect stratigraphic features and temporal variations in bed thickness, this study utilizes the Continuous Wavelet Transform (CWT) spectral decomposition application to garner the frequency components of the seismic data in the presence of gas hydrates. A benefit of employing this method is its capability to produce quality temporal resolution for high frequencies and quality frequency resolution for lower frequencies (Chakraborty & Okaya, 1995).

Sparse-Spike Decomposition

In attempting to gain better resolution of the seismic data, applied geophysicists and seismic interpreters pay particular attention to measurements associated with the scattering and dispersion of the seismic wave. This results in the decay of wave amplitude, reliant on a couple attenuation parameters (Chopra & Castagna, 2014). These parameters include an attenuation coefficient α and seismic quality factor, Q. The quality factor, Q, measures the degree of dissipation of a material such that high Q values indicate low dissipation/attenuation and lower Q values indicate high dissipation/attenuation of signals. Seismic attenuation is therefore a crucial tool in indicating pore structure, fluid content and lithology (Klimentos, 1995; Li et al., 2016), and therefore plays an important role in the approach to discerning BSR's. The quality factor will therefore be the attenuation parameter observed for the application of this study. Normally, to compensate for the loss of resolution or correct attenuation effects in the seismic data, an inverse Q filtering can be applied for further geophysical analyses (Morozov et al., 2018).

With the continuing need to find and implement geophysical workflows that allow us to detect elusive gas hydrates in the subsurface, herein we focus on uncovering the seismic signature of gas hydrates in deep-water settings using frequency based methods.

AREA OF STUDY

Geologic Setting

The Pegasus Basin is located on the eastern side of the central New Zealand midcontinent, adjacent to the transitional zone where the tectonic regime transforms from the subduction of the Pacific plate beneath the overriding Australian Plate along the Hikurangi Trough, to a strike-slip setting north east of South Island (Figure 2-1). The plate boundary runs in a SSW-NNW direction, from the strike slip zone of the Marlborough area, across the western subducting boundary of the Pegasus Basin, in the region known as Cook Strait, along the Hikurangi Trough, which extends into the northernmost Kermadec Trench. Its geometric shape covers an area of ~ 75000 km^2 (Bland et al., 2015), is defined in the north by the north-east trending East Coast Basin and structural highs to south and northwest, defined by east-west trending Chatam Rise and the Hikarungi Plateau, respectively. The basin consists of 80 million years of passive margin style sedimentation as a result of rift-related thermal subsidence which is now topped by an 8 km thick succession of siliciclastic material (Collier, 2015). The basin fill can be separated into two main sedimentation stages; (1) a 6 km thick deposition of sub-ducting related accretionary wedge material, located on the Pacific Plate, and comprising Neogene deepwater channels, turbidites and mass transport deposits that carried terrestrial sediments derived from the North and South Islands and from neighboring highs (King, 2017); (2) prior to this, an accumulation of >2km thick Late Cretaceous

and Paleogene sediments sourced from the Chatam Rise, commencing at the end of ancient Gondwana subduction between, 105 Myr to 24 Myr ago (King, 2017).

Overall, Bland et al. (2015) discuss four main phases of tectonism that influenced the formation of the Pegasus Basin, including (1) subduction along the ancient Gondwana boundary in the Mesozoic, (2) an ending stage of Early to Late Cretaceous subduction and compressional faulting, (3) a period of Late-Cretaceous to Paleogene thermal subsidence caused by cooling of a fraction of the underlying Hikurangi Plateau then (4) creation of a converging modern plate boundary.

The Pegasus Basin has been a very prominent region of interest for the study of gas hydrate origin and formation. One of the earliest implications for gas hydrate presence within the region, came from the interpretation of BSRs in seismic data in the shallow sedimentary layers of the subsurface (Katz, 1981). Katz (1981) also infers that hydrate presence can be determined by structural conditions (eg. one case being anticlinal vs. synclinal) that give way for the upward migration of gas to the hydrate stability zone where methane hydrates are formed. This can also include faults and fractures that can act as both pathways or seals. Several decades later, further research within the region would result in the gathering of raw data to further investigate this energy resource. Methane gas concentrations from cold seeps were sampled and analyzed in three separate areas along and near the Hikurangi Trough (Faure et al., 2010). A combination of collection methods was employed, and the analysis showed the occurrence of methane concentrations, of primarily biogenic origin, distributed along specific depths within the water column for each study area, neither of which showed methane concentrations at the sea surface (Faure et al., 2010). In 2011 a two-leg plan by research cruise SO-214 under the project name NEMESYS, set out to collect a wide range of data that included both seismic and geo-chemical

data (Bialas, 2011). This project also focused on several methane cold seeps along the Hikurangi Trough, including the Opouawe Bank, which reveal that its anticlinal structure guides upward fluid migration to the GHSZ (Plaza-Faverola et al., 2012; Koch et al., 2016). The presence of gas hydrates is also documented in bathymetric features further seaward, beneath a Frontal Anticline and sandy sediments underlying the Hikurangi channel (Plaza-Faverola et al., 2012; Kroeger et al., 2015). Additionally, in situ hydrate accumulation is constrained to recent to Pleistocene aged sediments supported by the presence of BSRs in seismic data observed within Pleistocene strata (Plaza-Faverola et al., 2012). Our application focuses on the cross sectional region that includes the Frontal Anticline and Hikurangi Channel. The combination of studies that provide strong evidence for regional sub-surface hydrate occurrence and fluid migration makes the Pegasus Basin, a unique area of focus where a multitude of methods can be applied.

Seismic Data

This study primarily utilizes two seismic surveys, the PEG09 and APB13 surveys - both conducted within the Pegasus Basin, for a comparative analysis of the efficiency of the applied methods. The former has been used in many studies compared to the latter, which makes it an ideal survey candidate for exploring a new method (Plaza-Faverola et al., 2012; Kroeger et al., 2015; Bedle, 2019; Clairmont & Bedle, 2019; Chenin & Bedle, 2020). The APB13 survey is used to validate the transferability of the geophysical attenuation method to ensure it provides consistent results across both surveys. The PEG09 survey comprises of 26 multi-channel 2D seismic lines with a total land cover of ~3000km, acquired in 2009 and 2010 by the New Zealand Ministry of Economic Development. Acquisition parameters include receivers placed at 12.5 meter intervals along a 10 km streamer, with shot intervals every 37.5 m, at a sampling rate of 2ms that provide a

record length of 12s in depth. At present, no borehole or exploratory wells exists within the basin. The APB13 survey followed, and was completed within the same area of interest, with higher resolution recorded data. Similar to the PEG09 survey, the APB13 consists of 54 multi-channel 2D seismic profiles that cover a distance of ~4600 km. Acquisition parameters include group intervals of geophones at 12.5 m and shot spacing at 37 m. Record length extends to 10.5s with a sampling rate of 2 ms.

METHODOLOGY

We have discussed a few methods that consistently include seismic data to aid in the detection of gas hydrates within the subsurface of continental margins. Some methods of which additional thermal modelling or velocity analyses were performed, that used only seismic data for interpretation and/or attribute analyses that can include machine learning application, other methods which included additional thermal modelling or velocity analyses. What is often discussed, that explores the relationship between the gas hydrate and the BSR, is an attenuation response influenced by the transition from the GHSZ to free gas below. Laboratory studies have observed attenuation within gas hydrate bearing sediment and free gas bearing sediment to varying degrees, where as many seismic studies have observed attenuation within the free gas zone by using frequency-dependent seismic attributes. Although certain inferences can be made from these seismic attributes, such as instantaneous frequency and reflection strength, they do not provide a direct quantitative measurement of the attenuation response via the Q-factor, and are therefore non-unique. Unfortunately, not many studies explore the direct measurement of the Q-factor in seismic data comprising of gas hydrates. We apply a recent attenuation method developed by Wang & Morozov (2020a), which extracts a statistical wavelet from seismic data and hence does

not require any well-logs. We first use conventional frequency attributes to show how it is not always a reliable method in imaging BSRs and hydrate systems, then with spectral decomposition aim to better image the bottom simulating reflectors with hopes of observing anomalies in the background geology within expected gas hydrate zone. The attenuation method serves to establish the exact location and spatial distribution of the gas hydrates and/or free gas and their quantitative response.

Three areas of interest are identified as zones consisting of; a strong continuous (SC) BSR (Region A) which includes Frontal Anticline, a weak discontinuous (WD) BSR (Region B) and a very strong continuous (VSC) BSR (Region C) which includes a portion of the Hikurangi Channel (Figure 2-2). We distinguish between the SC-BSR and VSC-BSR based on the observable strength of the amplitude reflector. Additionally, the apparent difference in surrounding seismic amplitude signatures (Region A being subtler) offer potential inferences in gas-hydrate related presence. Within each region, we initially examine and interpret the time-series response along seismic Traces 1150, 4500, and 6000, that corresponds to Regions A, B, and C respectively (See Figure 2-3). Observable attenuation effects can only be qualitatively assessed when interpreting the seismogram, as the signals show patterns of “decay”. It is worth mentioning that regular time-amplitude waveforms, or in this case the seismic traces, following the convolution model are not capable of resolving most geological properties or anomalous features that other methods may do well in imaging. We will show the attenuation method used in this study can directly measure and quantitatively interpret attenuation effects.

Seismic Attribute Application: Frequency attributes

Although they provide some benefits to interpretation, we proceeded to compute two frequency-related seismic attributes to briefly analyze and discuss the disadvantages such methods may have when performing a more comprehensive characterization of gas hydrate systems. We apply the instantaneous frequency and sweetness attributes to highlight such disadvantages. As aforementioned, the instantaneous-frequency attribute can be defined as the derivative of the instantaneous phase, which indicates time-dependent frequency information associated with the seismic trace. We use IF to resolve the trends of the BSR and indirectly observe attenuation effects in the seismic. The sweetness attribute is a division of the trace envelope by the square of the instantaneous frequency (Radovich & Oliveros, 1998). It is a useful attribute for delineating sand-confined channels (Hart, 2008; Li et al., 2017; Reilly et al., 2020) as well as a good indicator of hydrocarbon reservoirs correlating to bright spots (Kumar et al., 2019; Azeem et al., 2016;). Here, sweetness is also used to better resolve the BSR.

Spectral Decomposition Application: Continuous Wavelet Transform

For this study, we ignore comparing the variations in the suite of parameters that may influence the computed results and focus on only one important parameter. Hence, for this workflow, we pay attention to how variations to the bandwidth of a window function defined by a mother ('Morlet') wavelet which convolves with the time series signal (seismic trace), may or may not improve the detection of the bottom-simulating reflectors. The convolution solution that defines the continuous wavelet transform comprises of this window function among other parameters that scale and translate the mother wavelet (Chakraborty & Okaya, 1995).

Defining this "type" of wavelet acts as a quality control method, which allows us to examine a time-frequency spectrum of the outputs to the CWT. Furthermore, we compute the spectral magnitudes of time-frequencies along a seismic trace within Region C, for half-bandwidths, fb = 0.26, 0.52 and 0.78. By examining the temporal and frequency resolutions that the different half-bandwidths provide, we select the best value to compute the spectral components from the 10 -120Hz range using a 5Hz step. In order to determine what frequencies do well in resolving the geological properties associated with BSRs, we examine several spectral components of low-frequencies (20Hz & 40Hz components) and higher frequencies (60 & 80Hz components). It is imperative that the once the BSRs can be better delineated, the results of the attenuation may provide further insight into gas hydrate and/or free gas accumulation.

Attenuation Application: Sparse-Spike decomposition

In order to accurately interpret the attenuation response within the seismic data, we simply apply a wavelet–estimation procedure developed by Wang & Morozov (2020a), and then use a spectral ratio method to determine the frequency-dependent quality factor, *Q*. The benefit of using this method especially in our case, is that it is a non-stationary statistical method that does not require well log information. An important assumption put forth for this method is that the largest amplitude peaks within a seismic trace are sparse enough that when estimating the wavelet, the neighboring reflections are small enough such that unnecessary noise is removed. The following steps describe the iterative process to achieve the estimated wavelet (Wang & Morozov, 2020a; Wang et al., 2020b);

1. Extract tapered sections along the seismic trace by overlapping windows of a specified length. The size of this window length should be larger than the source waveform length.
2. Within each windowed section, a number of the largest amplitude peaks are identified at time t_n and amplitude value A_n.
3. The windowed section of a specific length centered on each picked peak is extracted from the seismic trace.
4. Following the extraction of the windowed section, they are then aligned and stacked together to achieve the estimated wavelet, with the right-hand-side of variables including; the normalization of the peak amplitude via an rms (root-mean-square) amplitude (A_{rms}), an amplitude scaling factor for the wavelet and a Hamming taper that has the same length of the seismic trace and a sign function.
5. To determine the quality factor using the spectral ratio method, using pairs of the current and succeeding windowed sections, the quality factor is estimated between each pair such that;

$$Q^{-1} = -\left(\frac{1}{\pi(t_{i+1}-t_i)}\right)\ln\left(\frac{A_{i+1}(f_j)}{A_i(f_j)}\right) \quad \text{(1)}$$

where i represents the current windowed section, t_i is the time at that moment and the function $A_i(f)$ represents the amplitude spectra of the estimated wavelet.

RESULTS

The following results provide a holistic approach of the variety of methods applied to inferring the presence of gas hydrates within the subsurface. We explore the anomalies associated

with the different types of BSRs that we've defined, in their respective locations along the cross-section profiles, that can be interpreted from regular seismic amplitude data. Frequency-dependent seismic attributes of instantaneous frequency and sweetness were then applied to briefly examine where they fall short of being conclusive, and hence spectral decomposition provides a more in-depth computational analyses. The sparse-spike spectral decomposition results give both a quantitative and qualitative understanding about the direct relationship between BSRs and attenuation within gas hydrate bearing sediment and free gas bearing sediment.

Gas Hydrates and seismic amplitude

We observe the negative amplitude response of the BSR along Traces 1150, 2900 and 4400 (Figure 2-3). Along Trace 1150 (Region A), where the BSR is at ~3500 ms, after less than 500 ms the amplitude begins to decrease within the free gas zone and therefore the signal attenuates. This is also observed along Trace 4400, consisting of the very strong continuous BSR at ~4000 ms, in which the signal attenuates at ~4500ms as it propagates through the free gas zone. On the contrary, along Trace 2900 there is no observable attenuation of the signal, but amplitude responses that are not easily discernable from those within the gas hydrate stability zone. Interestingly, the signal increases in magnitude before decreasing at around 5500 ms. In all three cases (Traces 1150, 2900, 4400), the response within the interval of the GHSZ are similar and provides no real indication of gas hydrate accumulation.

Gas Hydrates and frequency attributes

The distinct, "local" SC and VSC BSRs are separated by a region of a WD BSR (Figure 2-4a). This WD BSR has a low IF response and hence blends with the lateral conformable geology. Towards the northwest (NW) in the region of the SC-BSR, IF does slightly well in imaging the trend of the BSR (observed in seismic as well). Beneath the anticline folded layer which coincides with the trend of the BSR there is a concentrated distribution larger IF responses in addition to the region beneath the VSC-BSR which can also be described has having a larger discernable IF response (Figure 2-4b). The large distribution of the high IF values can be attributed to the accumulation of free gas beneath the anticline folded layer and the VSC-BSR. A region of very low frequencies, potentially LFSZz are observed beneath each of these features indicating the potential accumulation of free gas. There is no noticeable difference in the IF response from that of the seismic-amplitude beneath the region of the WD-BSR, such that the seismic amplitude responses coincide with that of the IF attribute. The sweetness attribute, which again is the envelope (Figure 2-5a) of the signal divided by the square of instantaneous frequency, improves imaging of the BSR. Although fairly weak, the sweetness attribute reveals the trend of the WC-BSR distinct from the reflections of the background geology (i.e. low sweetness values). Larger sweetness values sweetness coincides with the SC-BSR in the northwest and the VSC-BSR in the southeast, in addition to the large concentration of sweetness beneath the folded layer of the anticline and the VSC-BSR. Again, this suggests the potential accumulation of free gas within these regions. Low-frequency shadow zones cannot be interpreted with this attribute.

Gas Hydrates and spectral decomposition

As aforementioned, the results of the time-frequency plots are examined to determine which bandwidth size of the mother wavelet would be most suitable in improving the resolution of the bottom-simulating reflectors (Figure 2-6). The narrower band wavelets (f_b = 0.26) shows greater variation along the frequency component values (See Figure 2-6a) and therefore better frequency resolution compared to the broader band wavelet (f_b = 0.78) (See Figure 2-6c), however lacks variation in the temporal domain. Although we observe better resolution temporally, the broader band wavelet results in more smoothened magnitudes for the frequency domain (Figure 2-6c). These smoothen magnitudes provide poor frequency variation, making this bandwidth less ideal for interpretation in frequency domain. The results for the half-bandwidth f_b = 0.52 have less smoothen magnitudes, while also highlighting the variations in the temporal domain (Figure 2-6b). Since we are taking into consideration the frequency responses in addition to above and below the interpreted BSRs, this bandwidth seems to be a suitable candidate for generating the frequency components.

Along each frequency component profile, it is clear that high magnitudes of the frequencies coincide with trend of the SC-BSR and the region beneath the anticline folded layer, as well as with the trend of the VSC-BSR and the regions below it (Figure 2-7). However, each component does not improve the detection of the WD-BSR. The larger frequency components (60 & 80Hz) does a better job than the lower frequency components (20 & 40Hz) in delineating the BSR and reducing image smoothness (Figures 2-7a & 2-7b). Additionally, using the larger frequency components (especially the 80Hz component) we can better interpret the presence of LFSZs beneath the VSC-BSR and the subsurface folded layer of the Frontal Anticline. The spectrally decomposed larger frequency components therefore improves both the detection of BSR presence

and the LFSZs compared to the frequency attributes that only improved one of these seismic responses.

Gas Hydrates and attenuation

For the attenuation application using the sparse-spike decomposition method, we focus on comparing the results of the PEG09 Line 19 survey and the adjacent APB13 Line 40 survey (Figure 2-8). The three zones of interest are defined as Region A (Figures 2-8d & 2-8g) consisting of the SC-BSR as well as the Frontal Anticline, Region B (Figures 2-8e & 2-8h) consisting of the WD-BSR and Region C which comprises the VSC-BSR and a portion of the Hikurangi Channel (Figures 2-8f & 2-8i). The zoom in on Region A of the APB13 Line 40 survey shows a fault beneath the anticline fold, which is better interpreted to signify the higher resolution data of this seismic survey compared to the PEG09 data.

The inverse Q (Q^{-1}) results highlight the distribution of attenuation within the regions of interest for both the PEG09-19 and APB13-40 surveys (Figure 2-9). Within the region of the SC-BSR (light seismic amplitude reflector) we observe high attenuation values that surround and coincide with the BSR for both surveys, but zero to low attenuation in the region where the BSR cannot be well delineated between the SC-BSR and the anticline folded layer (Figures 2-9a & 2-9b). Notice between Traces 1800-2100 along the PEG19-19 survey, that there is a concentration of high attenuation of Q^{-1} = ~0.03 within the syncline folded layers, adjacent to the anticline folds (Figure 2-9a). Although this attenuation is not observed in APB13-40 survey (Figure 2-9b), it may suggest free gas presence migrating up-dip along the folded layer. Both surveys consist of a significant concentrated distribution of attenuation beneath and coinciding with the anticline

folded layer, with APB13-40 showing more distribution of the attenuation. Additionally, a high attenuation response situated at ~4750ms beneath the region of the Frontal Anticline, along the interpreted fault, can further support the presence of free gas migration in this area (See Figure 2-9b). With careful observation, we recognize that some potential multiples in the left uppermost areas of both surveys and beneath the SC-BSR in APB13-40 are congruent with significant attenuation. It is likely that the high amplitude artifacts contribute to the attenuation and is therefore not attribute to geology. The WD-BSR region shows zero attenuation along the BSR trend (~4250ms), but does have a region of high attenuation values Q^{-1} = ~0.03 & ~0.04 at depth between 4500-5000ms along PEG09-19 (Figure 2-9c). There is no significant attenuation associated with the WD-BSR along APB13-40 (Figure 2-9d). In both surveys the region of the VSC-BSR has the highest distribution of large attenuation values of Q^{-1} = ~ 0.04-0.05, predominantly below the BSR (Figures 2-9e & 2-f). Furthermore, there is a zone of high attenuation directly beneath the sea floor along PEG09-19 cross section but not along the APB13-40 cross section, near the bathymetric feature of the Hikurangi Channel.

Overall, the results of each method has advantages and disadvantages in the response to BSRs and gas hydrate systems. The IF attribute may not clearly image the trend of the BSR but can infer free gas accumulation as a result of LFSZs. Sweetness cannot detect LFSZs and can therefore be misleading to interpreters, however it can better discern BSRs especially WD-BSRs. The high frequency components of the spectral decomposition method have the benefit of better imaging the strong BSRs and separating it from the background geological response, whilst also identifying the LFSZs in the seismic. The attenuation method provides the quantitative measurement and response of attenuation in zones where we do expect free gas accumulation and

migration which can be used to indirectly infer the presence of gas hydrates in the overlying sediment strata.

DISCUSSION

Gas hydrate attenuation in the Pegasus Basin

Interpretation of seismic amplitudes data, remind us interpreters that it is often not a reliable attribute to make sound conclusions but more of a guidance to improve our analyses. Although Traces 1150 and 4400 (See Figure 2-3) show patterns of signal attenuation, especially where strong BSRs are present, there are many factors, irrespective of gas hydrate accumulation and free gas presence, that can contribute this attenuation response. These factors include, but are not limited to, poor lithological compaction, hydrocarbon reservoirs, fluid (eg. brine) presence, and other physical rock properties (Best et al., 2013; Dvorkin et al., 2014).

Comprehensively, the results point to a pattern of seismic attenuation that predominantly occur within the well-known regions of accumulated free gas and not within the gas hydrate stability zone. With a more solid understanding of attenuation using the sparse-spike decomposition, the combination of the methods provides four main intuitive observations. These observations include; (1) low frequency shadow zones seem to correlate with large values of attenuation; (2) a strong relationship between the amplitude strength of the BSR and the increase of the attenuation response; (3) the interpretation of migration pathways of the free gas using the direct attenuation measurement method and (4) for the data analyzed, the gas hydrate stability zone itself does not give rise to either impedance or attenuation anomalies that differentiate it from nearby non-hydrate zones. Additionally, since the APB13 survey is of higher resolution and may

be a better candidate for accurate results, we compute and interpret the APB13-42 2D line adjacent to the PEG09-19 and APB13-40.

Observation 1: LFSZ and attenuation

The LFSZs observed in seismic attribute analyses have very much indicated the potential presence of gas hydrates within the subsurface due to changes difference in medium properties. As aforementioned Taylor et al. (2000) show that these low-frequency signatures can be attributed to the free gas regions below BSRs that exhibit very strong seismic reflection, capped by the hydrate layer with larger frequency responses (refer to Figure 2-4b). This is a result of the presence of gas bearing sediments (mostly gas sands) that filter signal frequencies via absorption creating the LFSZs below the zone of hydrocarbon accumulation (Taner et al., 1979). The low-frequency shadow (LFS) is described as a feature in seismic that occurs as the high-frequency components of a signal become attenuated at a shorter distance than the low-frequency components, therefore resulting in low-frequencies below the highly attenuated interval (Castagna et al., 2003; Dvorkin et al., 2014). Hence the LFSZs occur a few 100ms at depth below the VSC-BSR (NW of the Hikurangi Channel) and the anticline folded layer where we infer free gas accumulation supported by several studies (Plaza-Faverola et al., 2012; Kroeger et al., 2015). However, this is not always the case since large instantaneous frequencies can occur below the BSR (Kim et al., 2015). Nevertheless, similar analyses can be inferred for the spectral decomposition such that the the larger individually computed frequencies can better infer the LFSZ due to loss of energy of the higher frequencies, when compared to the lower frequency components. The large values of the direct attenuation measurement of the sparse-spike decomposition supports the inference that there is a free gas system with significant attenuation within the interpreted LFSZ between 4500-5000

ms, beneath anticline folded layer of the APB13-40 2D line (See Figure 2-9) and APB13-40 2D line (See Figure 2-10a) and between 4000-5000 ms beneath the VSC-BSR regions for the PEG09-19 (Figures 2-9e), APB12-40 (Figures 2-9f) and APB13-42 (Figure 2-10d) 2D lines.

Observation 2: BSR strength and attenuation

We have identified that the type and strength of the BSR has a direct relationship to the response of attenuation. The contrast in seismic velocity such as the P-wave velocity, is affected by the concentration of gas that can therefore determine the strength of the reflection in the seismic data (Holbrook et al., 1996; Taylor et al., 2000). This can explain the difference in attenuation response for the SC-BSR and the VSC-BSR zones and the occurrence of the WD-BSR. The WD-BSR has a low attenuation response for several 100 ms beneath, suggesting there is no free-gas accumulation directly below, but likely within the deeper highly attenuated section between 4500-5000ms (See Figure 2-9c). The lack of the accumulation of free gas can result in the apparent weak/low BSR amplitudes (Wu et al., 2007). Although the IF and sweetness attributes, and the spectral decomposition provide no indication for free gas accumulation the inverse Q (Q^{-1}) clearly demonstrates this. The vertical separation of the high attenuation zone from the interpreted BSR trend signify the importance of the location and vertical distribution of the free gas to the type and extent of the BSR. We speculate that the zone of zero attenuation that separates the weak BSR and the high attenuation zone, can be caused by an upward transition from high laterally permeable sediments (marked by high attenuation) to low permeable fine grained sediments after findings by Bai (2016) along the Hikurangi Margin. It is likely that no conduits for vertical permeability exists. The absence of this zone of high attenuation below the WD-BSR for the APB13 survey (Figure 2-9d) can only be explained by either a lower concentration of free gas or no free gas in this particular area. On the contrary the APB13-42 line does have significant attenuation directly below the WD-

BSR opposing the aforementioned analyses. However, this strong attenuation coexists with a strong chaotic seismic response observed in the seismic amplitude and can therefore be influenced by the seismic amplitude rather than free gas presence. Furthermore, it is important to note a study conducted by Holbrook et al. (1996) identified that although the BSR was strongest at Well Site 995 for the Ocean Drilling Program (ODP) Leg 164 along Blake Ridge, VSP data showed that the concentration of free gas was larger at adjacent well Site 997 directly beneath an intersected weak, but discernable seismic BSR. Plaza-Faverola et al. (2012) identified that buried channel sands overlain by the present day Hikurangi Channel can accommodate a significant amount of methane hydrate and free gas. We can therefore infer that the VSC BSR and its high attenuation, although further west away from the Hikurangi Channel, is caused by the large concentration of free gas in that area.

Observation 3: Free gas Migration and Q^{-1}

What is promising from the results, is that we can postulate zones of migration due to the vertical pattern of the attenuation response. For a more accurate analysis, we focus on the attenuation that occur within two main locations influenced by fluid migration; (1) the frontal anticline and (2) the buried sediments west of the Hikurangi Channel. We infer that the high attenuation below the frontal anticline is associated with the migration of methane gas via faults, fractures and folding (Crutchley et al., 2019) accommodated by deformation that form the structural anticline. Dewangan (2014) made similar deductions when high attenuation, using an effective Q estimation from seismic peak frequencies, agreed with faults cross cutting hydrate layers. The distribution of the attenuation response suggest it may be sourced from the flanks and accumulating at the crest of the folded anticline layer. This may seem contradictory to

interpretations that the blanking zone (i.e. the LFSZ in the IF attribute and CWT) of the seismic amplitude may actually indicate the presence of "debatable" biogenic (Kroeger et al., 2015) sourced free gas in sediments directly beneath the center of the anticline (Plaza-Faverola et al., 2012). The free gas may be accumulating below the crest of the anticline layer, but not accumulating further below, hence the pattern of distribution of inverse Q (Q^{-1}) observed in our results. One can hypothesize that the accumulated free gas, upon absorption of the seismic energy, will result in low frequency-low amplitude signals to image the deeper sections creating the amplitude blanking zone without free gas as a contributor. Several studies have identified that the potential pathways to fluid migration in the region of the VSC-BSR, is collocated to the largest attenuation values because of high concentrations of free gas as well. The mechanism behind this can be its proximity to the subducting plate, in which thermogenic gas migrates upward along the subduction zone and into the sediments below the BSR near the Hikurangi channel (Plaza-Faverola et al., 2012; Kroeger et al., 2015).

Observation 4: No direct relationship with GHSZ

One of our main goals is to measure the nature of attenuation within the gas-hydrate stability zone to provide a method that can directly identify gas hydrate presence using seismic data. However, we have learned from the results of the inverse Q, that the method does not directly identify any significant response within the well-known hydrate-bearing sediment interval. This is not an unexpected result, but studies that have observed the influence of gas hydrate bearing sediments on increasing attenuation (Guerin et al., 1999; Guerin & Goldberg, 2002; Dvorkin & Uden, 2004) have piqued a lot of interest in the hydrate community. Several mechanisms explain the reasons for the increased attenuation; one in particular, identifies viscosity related energy loss

due to crossflow of pore-fluid between difference medium rigidities (Dvorkin & Uden, 2004). Note that several of the following studies measured the quality factor, Q, via distinct mathematical approaches, using different data such sourced from well-logs, or seismic reflection data. Upon comparing with their results, note that the order of magnitudes differs, but the general assessment of the hydrate or free gas response is objectively reasonable. Dvorkin & Uden (2004) used an attenuation model, and estimated high attenuation values along a well, with the methane hydrate interval between Q^{-1} = 0.15 and 0.20 (Q = 6.67 and 5, respectively), opposing the observed attenuation in our Q^{-1} plots. Similar to the results of our study Dewangan et al. (2014) used seismic data to reveal low attenuation associated with hydrate bearing sediments. However, their average Q values ranged > 200, making our results only qualitatively and not quantitatively comparable. Furthermore, using a logarithmic spectral ratio for prestack, a study by Sain et al. (2009) measured high values of Q (~256; i.e. low attenuation) within gas hydrate intervals above the BSR and lower values of Q (120-137; i.e. high attenuation) for brine saturated sediments below the BSR, a case for much lower attenuation if gas was present. It is difficult to provide a conclusive reason as to why we observe no high attenuation in the Q^{-1} profiles. There are many factors that may need to be considered for a comparative analysis such as the dominant frequency of the seismic, frequency of sonic logs, the geology of subsurface and petro-physical properties to name a few.

Application in the Gulf of Mexico

Keeping the results of our investigation in the Pegasus Bain in mind, we now apply this method to the Gulf of Mexico (GOM) to determine whether this attenuation based method would produce similar results in a basin with a geologic setting and history different to that of the Pegasus Basin. We seek to establish the potential for this method to be applied to a wide range of datasets,

and produce results that can help in gas hydrate exploration. Therefore, we perform the Q estimation method on the Alaminos Canyon 21 survey (AC-21) (See Figure 2-11) survey located in the Gulf of Mexico, which has a large database dedicated to the study and exploration of gas hydrates in the region. The AC-21 survey, which is located in the western region of the Gulf of Mexico, northwest of Keathley Canyon, in the Diana Basin, has also been studied for the possibilities of as hydrate exploration (Dai et al., 2004; Frye et al., 2009).

Attenuation in the AC21 survey

Here, we to took a simple approach, similar to that performed on the Pegasus Basin data, and observed a BSR that transitions from being strong and discernable in seismic to being weak and nearly impossible to recognize. Previous studies have identified this BSR and its representation as the base of the GHSZ (Dai et al., 2004; Frye et al., 2009). Sullivan et al. (2004) have recognized that in this region there exists a complex channel system and distribution of deep-water facies that are rich in sands, which have been well producing oil and gas reservoirs. However, Frye et al. (2009) expressed that the gas hydrates located in some of these reservoirs may not correlate with the observed BSR. Surprisingly, our results indicate a discontinuous response of low attenuation values along the stronger observed BSRs, but a stronger attenuation response that occupies the region of the weaker/faint BSR. There is no significant distribution of high attenuation along the BSR trend, however the results of this survey indicates that the weak/poorly visible BSR can have a high attenuation response. When compared to the weak/discontinuous BSR of the Pegasus Basin surveys, we can suggest confidently that is likely related to the free gas accumulation that attributes to the high attenuation along the weak BSR in Figure 2-12b. Therefore, although the trend of the BSR to the northwest may be strongly visible

in the seismic data, this particular area may not consist of free gas accumulation beneath and no gas hydrate above. Data limitation prevents us from conducting a more robust analysis for this area of interest and hence a better understanding of the attenuation collocated with the weak/discontinuous BSR.

Now that we have observed the results of the attenuation in three separate seismic surveys, in two different geologic settings, we include a performance summary of each of the applied method (See Table 2-1). Each of the method has been examined for the effectiveness as; (1) a direct gas hydrate indicator; (2) a free gas indicator; (3) a way of discerning strong BSRs and (4) discerning weak BSRs.

CONCLUSIONS

Using a comprehensive analysis of several methods to improve the detection of bottom-simulating reflectors, including seismic frequency-related attribute analysis and spectral decomposition (via continuous wavelet transform), we found that attenuation measurements estimated from the quality factor *Q* provide a means to map free gas. The SSD method has the ability of estimating *Q* from purely seismic data, and can therefore be performed without well-logs which are only rarely available in deep water settings. Several observations demonstrate this SSD-based workflow can be applicable to areas of interest, primarily for discerning the presence of free gas. We observe that; (1) low-frequency shadow zones defined in seismic attributes and spectral decomposition coincide with high attenuation; (2) there is a strong relationship with the amplitude strength of the BSR and the attenuation response; (3) the inverse Q (Q^{-1}) can reveal potential fluid migration pathways and (4) for the data analyzed, the gas hydrate stability zone itself does not give

rise to either impedance or attenuation anomalies that differentiate it from nearby non-hydrate zones. It is common that distinguishing the attenuation of gas hydrates with background sediments is a difficult task when using seismic data. Although several authors have identified anomalous attenuation in the gas hydrate zone itself, such is not the case for the New Zealand and Gulf of Mexico surveys presented herein. However, if the attenuation method can assist in identifying free gas distribution and accumulation, or subtler free gas that doesn't have a high seismic amplitude (i.e. a bright spot), the attenuation response can indirectly aid in identifying gas hydrates by identifying the free gas that is being trapped. While hydrates are notoriously difficult to directly detect in seismic data - similar to hydrocarbons, attenuation can be used as an indirect hydrate detection method, aiding in discerning and characterizing hydrates and/or their trapped free gas reservoirs within the subsurface.

ACKOWLEDGEMENTS

We sincerely thank New Zealand Petroleum & Minerals and Origin Energy New Zealand Pty Ltd for providing the Pegasus Basin dataset. Additionally, we express our greatest appreciation to Petrel E&P software from Schlumberger for providing the University of Oklahoma with the academic licenses for conducting this project as well as the AASPI (Attribute-Assisted Seismic Processing and Interpretation) consortium at the University of Oklahoma.

REFERENCES

Alajmi, M. S., Qadrouh, A. N., & Alotaibi, A. M. (2020). High-fold enhancement of a seismic image and detection of the low-frequency shadow below the bottom-simulating reflector. Arabian Journal of Geosciences, 13(5), 205. https://doi.org/10.1007/s12517-020-5138-x.

Archer, D., Buffett, B., & Brovkin, V. (2009). Ocean methane hydrates as a slow tipping point in the global carbon cycle. Proceedings of the National Academy of Sciences, 106(49), 20596–20601. https://doi.org/10.1073/pnas.0800885105.

Auger, F., Flandrin, P., Gonçalvès, P., & Lemoine., O. (1996). Time-Frequency Toolbox, CNRS, France; Rice University, USA.

Azeem, T., Yanchun, W., Khalid, P., Xueqing, L., Yuan, F., & Lifang, C. (2016). An application of seismic attributes analysis for mapping of gas bearing sand zones in the sawan gas field, Pakistan. Acta Geodaetica et Geophysica, 51(4), 723–744. https://doi.org/10.1007/s40328-015-0155-z.

Bai, H., Pecher, I. A., Adam, L., & Field, B. (2016). Possible link between weak bottom simulating reflections and gas hydrate systems in fractures and macropores of fine-grained sediments: Results from the Hikurangi Margin, New Zealand. Marine and Petroleum Geology, 71, 225–237. https://doi.org/10.1016/j.marpetgeo.2015.12.007.

Bedle, H. (2019). Seismic attribute enhancement of weak and discontinuous gas hydrate bottom-simulating reflectors in the Pegasus Basin, New Zealand. Interpretation, 7(3), SG11–SG22. https://doi.org/10.1190/INT-2018-0222.1

Best, A. I., Priest, J. A., Clayton, C. R. I., & Rees, E. V. L. (2013). The effect of methane hydrate morphology and water saturation on seismic wave attenuation in sand under shallow sub-seafloor conditions. Earth and Planetary Science Letters, 368, 78–87. https://doi.org/10.1016/j.epsl.2013.02.033.

Bialas, J., ed. (2011). FS SONNE Fahrtbericht / Cruise Report SO214 NEMESYS : 09.03.-05.04.2011, Wellington - Wellington, 06.-22.04.2011 Wellington - Auckland. Open

Access. IFM-GEOMAR Report, 47. IFM-GEOMAR, Kiel, 174 pp. DOI 10.3289/ifm-geomar_rep_47_2011

Bland, K. J., Uruski, C. I., & Isaac, M. J. (2015). Pegasus Basin, eastern New Zealand: A stratigraphic record of subsidence and subduction, ancient and modern. New Zealand Journal of Geology and Geophysics, 58(4), 319–343. https://doi.org/10.1080/00288306.2015.1076862.

Bryan, G. M. (1974). In situ indications of gas hydrate, in Natural gases in marine sediments: Marine Sci., v. 3, p. 299-308.

Castagna, J. P., Sun, S., & Siegfried, R. W. (2003). Instantaneous spectral analysis: Detection of low-frequency shadows associated with hydrocarbons. The Leading Edge, 22(2), 120–127. https://doi.org/10.1190/1.1559038.

Chakraborty, A., & Okaya, D. (1995). Frequency-time decomposition of seismic data using wavelet-based methods. GEOPHYSICS, 60(6), 1906–1916. https://doi.org/10.1190/1.1443922.

Chenin, J., & Bedle, H. (2020). Multi-attribute machine learning analysis for weak BSR detection in the Pegasus Basin, Offshore New Zealand. Marine Geophysical Research, 41(4), 21. https://doi.org/10.1007/s11001-020-09421-x.

Chopra, S., & Castagna, J, P. (2014). AVO, Investigations in Geophysics no. 16, Society of Exploration Geophysicists.

Clairmont, R., & Bedle, H. (2019). Seismic attribute identification through waveform analysis of gas hydrates in the Pegasus Basin, offshore New Zealand. Seg Technical Program Expanded Abstracts.

Collier, T. (2015). The geology of Pegasus Basin based on outcrop correlatives in southern Wairarapa and northeastern Marlborough, New Zealand. [Master dissertation, Victoria University of Wellington]. http://hdl.handle.net/10063/4831.

Crutchley, G. J., Kroeger, K. F., Pecher, I. A., & Gorman, A. R. (2019). How tectonic folding influences gas hydrate formation: New Zealand's Hikurangi subduction margin. Geology, 47(1), 39–42. https://doi.org/10.1130/G45151.1.

Dai, J., Xu, H., Snyder, F., & Dutta, N. (2004). Detection and estimation of gas hydrates using rock physics and seismic inversion: Examples from the northern deepwater Gulf of Mexico. The Leading Edge, 23(1), 60–66. https://doi.org/10.1190/1.1645456.

Dev, A., & McMechan, G. A. (2010). Interpreting structural controls on hydrate and free-gas accumulation using well and seismic information from the Gulf of Mexico. GEOPHYSICS, 75(1), B35–B46. https://doi.org/10.1190/1.3282680.

Dewangan, P., Mandal, R., Jaiswal, P., Ramprasad, T., & Sriram, G. (2014). Estimation of seismic attenuation of gas hydrate bearing sediments from multi-channel seismic data: A case study from Krishna–Godavari offshore basin. Marine and Petroleum Geology, 58, 356–367. https://doi.org/10.1016/j.marpetgeo.2014.05.015.

Diaconescu, C. C., & Knapp, J. H. (2002). Gas Hydrates of the South Caspian Sea, Azerbaijan: Drilling Hazards and Sea Floor Destabilizers. All Days, OTC-14036-MS. https://doi.org/10.4043/14036-MS.

Dickens, G. R., & Quinby-Hunt, M. S. (1997). Methane hydrate stability in pore water: A simple theoretical approach for geophysical applications. Journal of Geophysical Research: Solid Earth, 102(B1), 773–783. https://doi.org/10.1029/96JB02941.

Dvorkin, J., & Uden, R. (2004). Seismic wave attenuation in a methane hydrate reservoir. The Leading Edge, 23(8), 730–732. https://doi.org/10.1190/1.1786892.

Dvorkin, J., Gutierrez, M., & Grana, D. (2014). Seismic Reflections of Rock Properties. Cambridge: Cambridge University Press. https://doi:10.1017/CBO9780511843655.

Faure, K., Greinert, J., Pecher, I. A., Graham, I. J., Massoth, G. J., de Ronde, C. E. J., Wright, I. C., Baker, E. T., & Olson, E. J. (2006). Methane seepage and its relation to slumping and

gas hydrate at the Hikurangi margin, New Zealand. New Zealand Journal of Geology and Geophysics, 49(4), 503–516. https://doi.org/10.1080/00288306.2006.9515184.

Faure, K., Greinert, J., von Deimling, J. S., McGinnis, D. F., Kipfer, R., & Linke, P. (2010). Methane seepage along the Hikurangi Margin of New Zealand: Geochemical and physical data from the water column, sea surface and atmosphere. Marine Geology, 272(1–4), 170–188. https://doi.org/10.1016/j.margeo.2010.01.001.

Frye, M., Shedd, W., Godfriaux, P., Collett, T.S., Lee, M., Boswell, R., Dufrene, R. (2009). Gulf of Mexico Gas Hydrate Joint Industry Project Leg II d Alaminos Canyon 21 site summary. In: Proceedings of the Drilling and Scientific Results of the 2009 Gulf of Mexico Gas Hydrate Joint Industry Project Leg II. https://www.netl.doe.gov/technologies/oilgas/publications/Hydrates/2009Reports/AC21SiteSum.pdf.

Ghiassian, H., & Grozic, J. L. H. (2013). Strength behavior of methane hydrate bearing sand in undrained triaxial testing. Marine and Petroleum Geology, 43, 310–319. https://doi.org/10.1016/j.marpetgeo.2013.01.007.

Goupillaud, P., Grossman, A. and Morlet, J. (1984) Cycle-Octave and Related Transforms in Seismic Signal Analysis. Geoexploration, 23, 85-102. http://dx.doi.org/10.1016/0016-7142(84)90025-5.

Guerin, G., Goldberg, D., & Meltser, A. (1999). Characterization of in situ elastic properties of gas hydrate-bearing sediments on the Blake Ridge. Journal of Geophysical Research: Solid Earth, 104(B8), 17781–17795. https://doi.org/10.1029/1999JB900127.

Guerin, G., & Goldberg, D. (2002). Sonic waveform attenuation in gas hydrate-bearing sediments from the Mallik 2L-38 research well, Mackenzie Delta, Canada. Journal of Geophysical Research, 107(B5), 2088. https://doi.org/10.1029/2001JB000556.

Hart, B. (2008). Stratigraphically significant attributes. The Leading Edge, 27(3), 320–324. https://doi.org/10.1190/1.2896621.

Hillman, J. I. T., Cook, A. E., Sawyer, D. E., Küçük, H. M., & Goldberg, D. S. (2017). The character and amplitude of 'discontinuous' bottom-simulating reflections in marine seismic data. Earth and Planetary Science Letters, 459, 157–169. https://doi.org/10.1016/j.epsl.2016.10.058.

Holbrook, W. S., Hoskins, H., Wood, W. T., Stephen, R. A., Lizarralde, D., & Leg 164 Science Party. (1996). Methane Hydrate and Free Gas on the Blake Ridge from Vertical Seismic Profiling. Science, 273(5283), 1840–1843. https://doi.org/10.1126/science.273.5283.1840.

Hyodo, M., Yoneda, J., Yoshimoto, N., & Nakata, Y. (2013). Mechanical and dissociation properties of methane hydrate-bearing sand in deep seabed. Soils and Foundations, 53(2), 299–314. https://doi.org/10.1016/j.sandf.2013.02.010.

Katz, H.-R. (1981). PROBABLE GAS HYDRATE IN CONTINENTAL SLOPE EAST OF THE NORTH ISLAND, NEW ZEALAND. Journal of Petroleum Geology, 3(3), 315–324. https://doi.org/10.1111/j.1747-5457.1981.tb00933.x.

Kim, K. J., Yi, B. Y., Kang, N. K., & Yoo, D. G. (2015). Seismic Attribute Analysis of the Indicator for Gas Hydrate Occurrence in the Northwest Ulleung Basin, East Sea. Energy Procedia, 76, 463–469. https://doi.org/10.1016/j.egypro.2015.07.882.

King, S.E. (2017). The Tectonic Evolution of Pegasus Basin and the Hikurangi Trench, offshore New Zealand: Master's Thesis, Colorado School of Mines

Klimentos, T. (1995). Attenuation of P - and S -waves as a method of distinguishing gas and condensate from oil and water. GEOPHYSICS, 60(2), 447–458. https://doi.org/10.1190/1.1443782.

Koch, S., Schroeder, H., Haeckel, M., Berndt, C., Bialas, J., Papenberg, C., Klaeschen, D., & Plaza-Faverola, A. (2016). Gas migration through Opouawe Bank at the Hikurangi margin offshore New Zealand. Geo-Marine Letters, 36(3), 187–196. https://doi.org/10.1007/s00367-016-0441-y.

Kroeger, K. F., Plaza-Faverola, A., Barnes, P. M., & Pecher, I. A. (2015). Thermal evolution of the New Zealand Hikurangi subduction margin: Impact on natural gas generation and methane hydrate formation – A model study. Marine and Petroleum Geology, 63, 97–114. https://doi.org/10.1016/j.marpetgeo.2015.01.020.

Kroeger, K. F., Crutchley, G. J., Hill, M. G., & Pecher, I. A. (2017). Potential for gas hydrate formation at the northwest New Zealand shelf margin—New insights from seismic reflection data and petroleum systems modelling. Marine and Petroleum Geology, 83, 215–230. https://doi.org/10.1016/j.marpetgeo.2017.02.025.

Kumar, J., Sain, K., & Arun, K. P. (2019). Seismic attributes for characterizing gas hydrates: A study from the Mahanadi offshore, India. Marine Geophysical Research, 40(1), 73–86. https://doi.org/10.1007/s11001-018-9357-4.

Kvenvolden, K. A. (2002). Methane hydrate in the global organic carbon cycle: Global methane hydrate. Terra Nova, 14(5), 302–306. https://doi.org/10.1046/j.1365-3121.2002.00414.x.

Lee, J., Byun, J., Kim, B., & Yoo, D.-G. (2017). Delineation of gas hydrate reservoirs in the Ulleung Basin using unsupervised multi-attribute clustering without well log data. Journal of Natural Gas Science and Engineering, 46, 326–337. https://doi.org/10.1016/j.jngse.2017.08.007.

Li, F., Verma, S., Zhou, H., Zhao, T., & Marfurt, K. J. (2016). Seismic attenuation attributes with applications on conventional and unconventional reservoirs. Interpretation, 4(1), SB63–SB77. https://doi.org/10.1190/INT-2015-0105.1.

Li, Q., Yu, S., Wu, W., Tong, L., & Kang, H. (2017). Detection of a deep-water channel in 3D seismic data using the sweetness attribute and seismic geomorphology: A case study from the Taranaki Basin, New Zealand. New Zealand Journal of Geology and Geophysics, 60(3), 199–208. https://doi.org/10.1080/00288306.2017.1307230.

Liu, J., & Marfurt, K. J. (2007). Instantaneous spectral attributes to detect channels. GEOPHYSICS, 72(2), P23–P31. https://doi.org/10.1190/1.2428268.

Madhusudhan, B. N., Clayton, C. R. I., & Priest, J. A. (2019). The Effects of Hydrate on the Strength and Stiffness of Some Sands. Journal of Geophysical Research: Solid Earth, 124(1), 65–75. https://doi.org/10.1029/2018JB015880

Makogon, Y. F., Holditch, S. A., & Makogon, T. Y. (2007). Natural gas-hydrates—A potential energy source for the 21st Century. Journal of Petroleum Science and Engineering, 56(1–3), 14–31. https://doi.org/10.1016/j.petrol.2005.10.009.

Markl, R. G., Bryan, G. M., & Ewing, J. I. (1970). Structure of the Blake-Bahama Outer Ridge. Journal of Geophysical Research, 75(24), 4539–4555. https://doi.org/10.1029/JC075i024p04539.

Maslin, M., Owen, M., Betts, R., Day, S., Dunkley Jones, T., & Ridgwell, A. (2010). Gas hydrates: Past and future geohazard? Philosophical Transactions of the Royal Society A: Mathematical, Physical and Engineering Sciences, 368(1919), 2369–2393. https://doi.org/10.1098/rsta.2010.0065.

Matsumoto, R., Ryu, B.-J., Lee, S.-R., Lin, S., Wu, S., Sain, K., Pecher, I., & Riedel, M. (2011). Occurrence and exploration of gas hydrate in the marginal seas and continental margin of the Asia and Oceania region. Marine and Petroleum Geology, 28(10), 1751–1767. https://doi.org/10.1016/j.marpetgeo.2011.09.009.

Morozov, I., Haiba, M., & Deng, W. (2018). Inverse attenuation filtering. GEOPHYSICS, 83(2), V135–V147. https://doi.org/10.1190/geo2016-0211.1.

Morlet, J., Arens, G., Fourgeau, E., & Glard, D. (1982). Wave propagation and sampling theory—Part I: Complex signal and scattering in multilayered media. GEOPHYSICS, 47(2), 203–221. https://doi.org/10.1190/1.1441328.

Osborn, S. G., Vengosh, A., Warner, N. R., & Jackson, R. B. (2011). Methane contamination of drinking water accompanying gas-well drilling and hydraulic fracturing. Proceedings of the National Academy of Sciences of the United States of America, 108(20), 8172–8176. https://doi.org/10.1073/pnas.1100682108.

Paganoni, M., Cartwright, J. A., Foschi, M., Shipp, R. C., & Van Rensbergen, P. (2016). Structure II gas hydrates found below the bottom-simulating reflector: Structure II Gas Hydrates Below a BSR. Geophysical Research Letters, 43(11), 5696–5706. https://doi.org/10.1002/2016GL069452.

Partyka, G., Gridley, J., & Lopez, J. (1999). Interpretational applications of spectral decomposition in reservoir characterization. The Leading Edge, 18(3), 353–360. https://doi.org/10.1190/1.1438295.

Plaza-Faverola, A., Klaeschen, D., Barnes, P., Pecher, I., Henrys, S., & Mountjoy, J. (2012). Evolution of fluid expulsion and concentrated hydrate zones across the southern Hikurangi subduction margin, New Zealand: An analysis from depth migrated seismic data: HIKURANGI HYDRATE ZONES FROM PSDM. Geochemistry, Geophysics, Geosystems, 13(8), n/a-n/a. https://doi.org/10.1029/2012GC004228.

Radovich, B. J., & Oliveros, R. B. (1998). 3-D sequence interpretation of seismic instantaneous attributes from the Gorgon Field. The Leading Edge, 17(9), 1286–1293. https://doi.org/10.1190/1.1438125.

Reilly, P., Clairmont, R., & Bedle, H. (2020). Are bright spots always hydrocarbons? A case study in the Taranaki Basin, New Zealand. Interpretation, 8(4), SR45–SR51. https://doi.org/10.1190/INT-2020-0047.1.

Sain, K., Singh, A. K., Thakur, N. K., & Khanna, R. (2009). Seismic quality factor observations for gas-hydrate-bearing sediments on the western margin of India. Marine Geophysical Researches, 30(3), 137–145. https://doi.org/10.1007/s11001-009-9073-1.

Shedd, W., Boswell, R., Frye, M., Godfriaux, P., & Kramer, K. (2012). Occurrence and nature of "bottom simulating reflectors" in the northern Gulf of Mexico. Marine and Petroleum Geology, 34(1), 31–40. https://doi.org/10.1016/j.marpetgeo.2011.08.005.

Sloan, E. D. (2003). Fundamental principles and applications of natural gas hydrates. Nature, 426(6964), 353–359. https://doi.org/10.1038/nature02135.

Singh, S. C., Minshull, T. A., & Spence, G. D. (1993). Velocity Structure of a Gas Hydrate Reflector. Science, 260(5105), 204–207. https://doi.org/10.1126/science.260.5105.204

Sullivan, M. D., J. L. Foreman, D. C. Jennette, D. Stern, G. N. Jensen, and F. J. Goulding. (2004). An integrated approach to characterization and modeling of deep-water reservoirs, Diana field, western Gulf of Mexico, in Integration of outcrop and modern analogs in reservoir modeling: AAPG Memoir 80, p. 215–234. https://doi.org/10.1306/M80924C11.

Taylor, M. H., Dillon, W. P., & Pecher, I. A. (2000). Trapping and migration of methane associated with the gas hydrate stability zone at the Blake Ridge Diapir: New insights from seismic data. Marine Geology, 164(1–2), 79–89. https://doi.org/10.1016/S0025-3227(99)00128-0.

Taner, M. T., Koehler, F., & Sheriff, R. E. (1979). Complex seismic trace analysis. GEOPHYSICS, 44(6), 1041–1063. https://doi.org/10.1190/1.1440994.

Vadakkepuliyambatta, S., Chand, S and Bünz, S. (2017). "The History and Future Trends of Ocean Warming-induced Gas Hydrate Dissociation in the SW Barents Sea." Geophysical Research Letters 44 (2): 835–44. https://doi.org/10.1002/2016GL071841.

Wang, Y., & Morozov, I. B. (2020a). A simple approach to nonstationary source waveform estimation in seismic records. GEOPHYSICS, 85(3), V257–V268. https://doi.org/10.1190/geo2019-0133.1.

Wang, Y., Morozov, I., & Marfurt, K. (2020b). Non-stationary source waveform and Q estimation by sparse-pulse decomposition of seismic images. SEG Technical Program Expanded Abstracts 2020, 2789–2793. https://doi.org/10.1190/segam2020-3428440.1.

Wigner, E. (1932). On the Quantum Correction for Thermodynamic Equilibrium. Physical Review, 40(5), 749–759. https://doi.org/10.1103/PhysRev.40.749.

Wood, W. T., Hart, P. E., Hutchinson, D. R., Dutta, N., Snyder, F., Coffin, R. B., & Gettrust, J. F. (2008). Gas and gas hydrate distribution around seafloor seeps in Mississippi Canyon, Northern Gulf of Mexico, using multi-resolution seismic imagery. Marine and Petroleum Geology, 25(9), 952–959. https://doi.org/10.1016/j.marpetgeo.2008.01.015.

Wu, S., Wang, X., Wong, H. K., & Zhang, G. (2007). Low-amplitude BSRs and gas hydrate concentration on the northern margin of the South China Sea. Marine Geophysical Researches, 28(2), 127–138. https://doi.org/10.1007/s11001-007-9020-y.

FIGURES

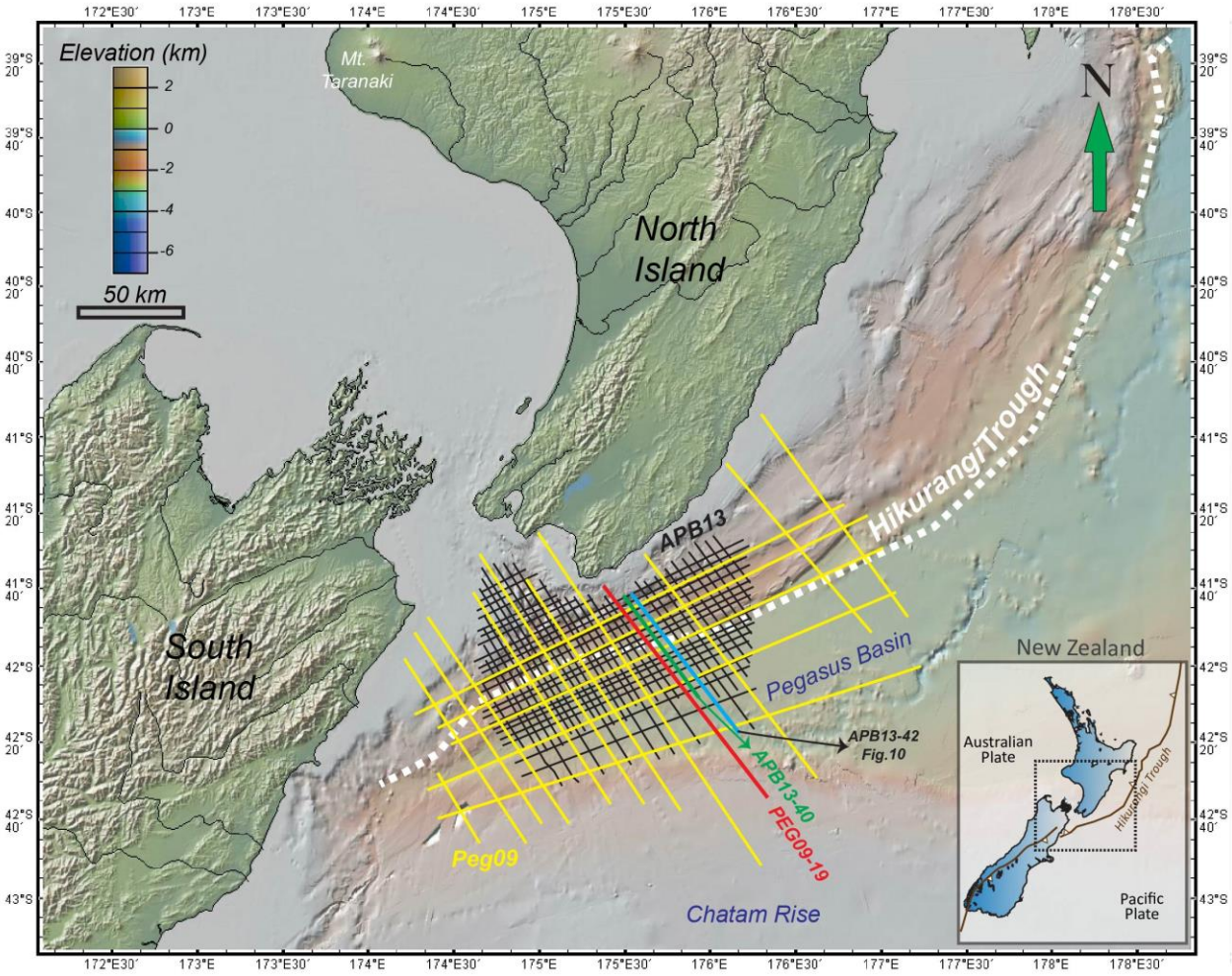

Figure 2-1. Topographic map of New Zealand the PEG09 and APB13 surveys within the Pegasus Basin and the known structural features that surround the basin, including the Chatam Rise and the Hikurangi Trough. The cross sections used in this study are highlighted in red (PEGO9-19), green (APB13-40) and cyan (APB13-42). *(Base map Courtesy GeoMapApp)*

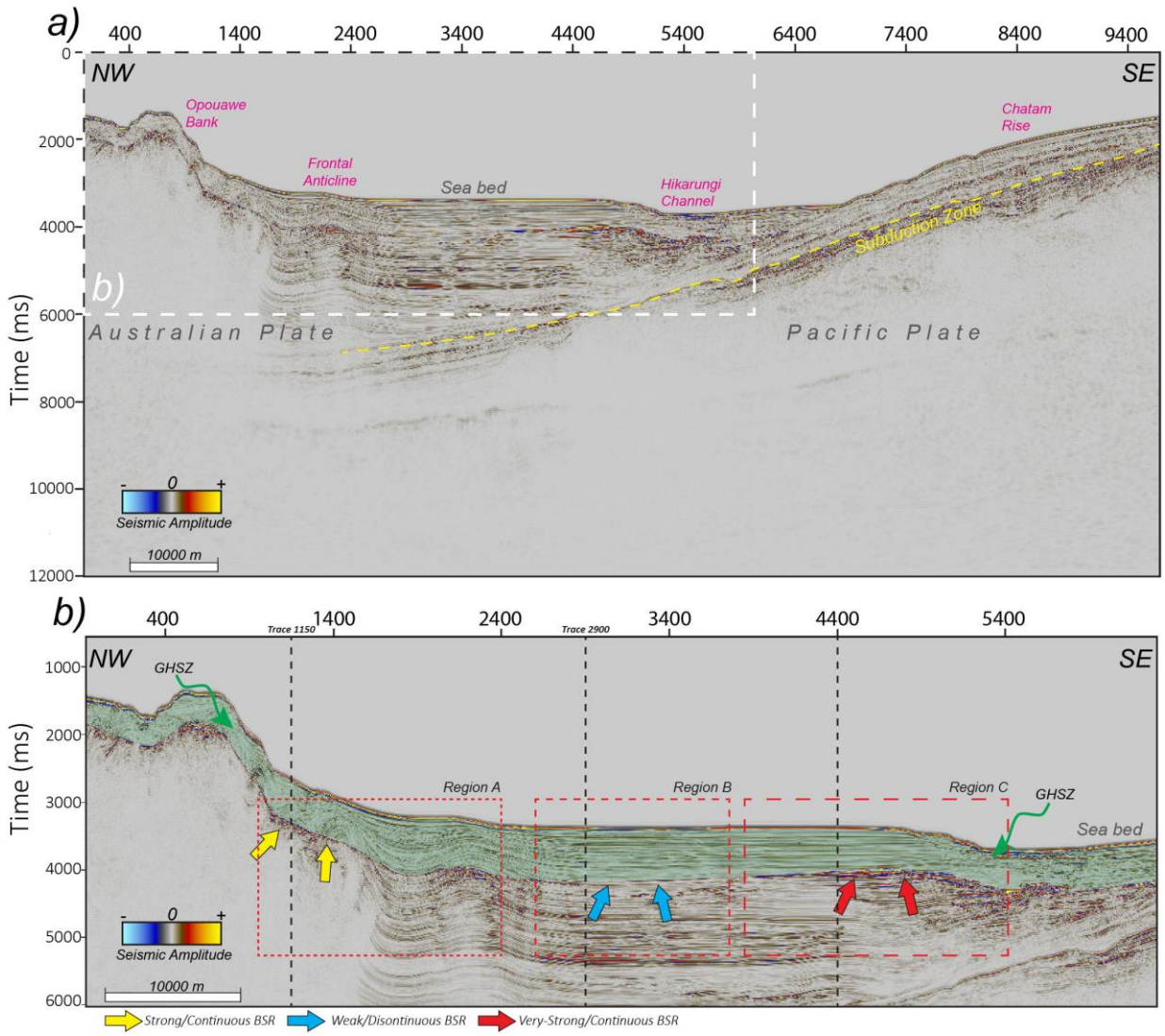

Figure 2-2. Cross sectional profile of the PEG09 Line 19 (PEG09-19) and the interpreted GHSZ. Three types of BSRs based on observable amplitude strength were described in this study and are pointed at by the box-arrows. These include a; (1) strong-continuous (SC) BSR in Region A, (2) weak/discontinuous (WD) BSR in Region B and (3) very-strong continuous BSRs in Region C. To further inspect the amplitude changes, traces 1150, 2900 and 4400 (dashed vertical lines) representing zones A, B, and C are shown in the next figure (Figure 2-3).

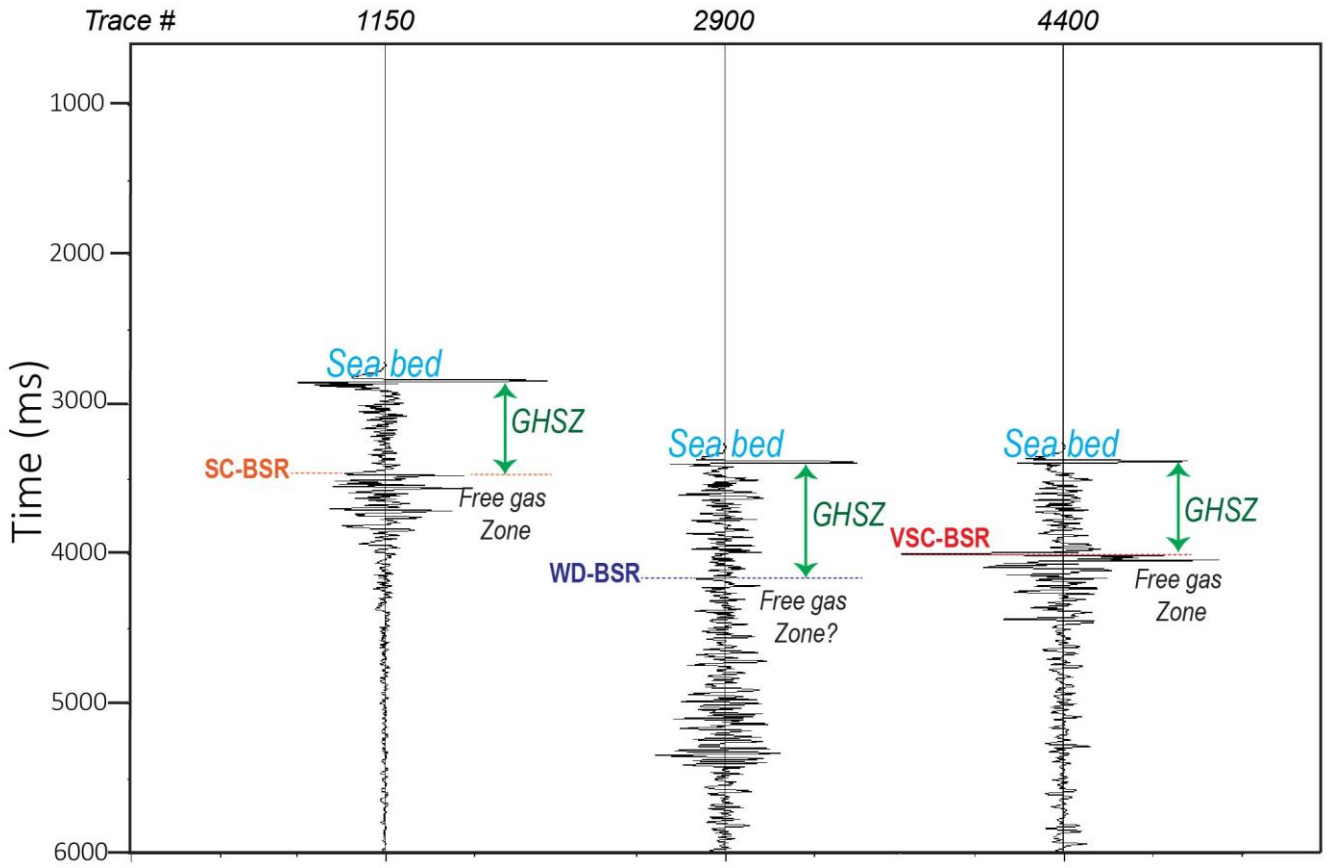

Figure 2-3. The seismic amplitude response of the GHSZ and free gas zone for representative traces extracted from the zones A, B, and C shown in the previous slide. Note that there is no anomalous response of the GHSZ. In contrast, the free gas zone gives rise to a strong amplitude response.

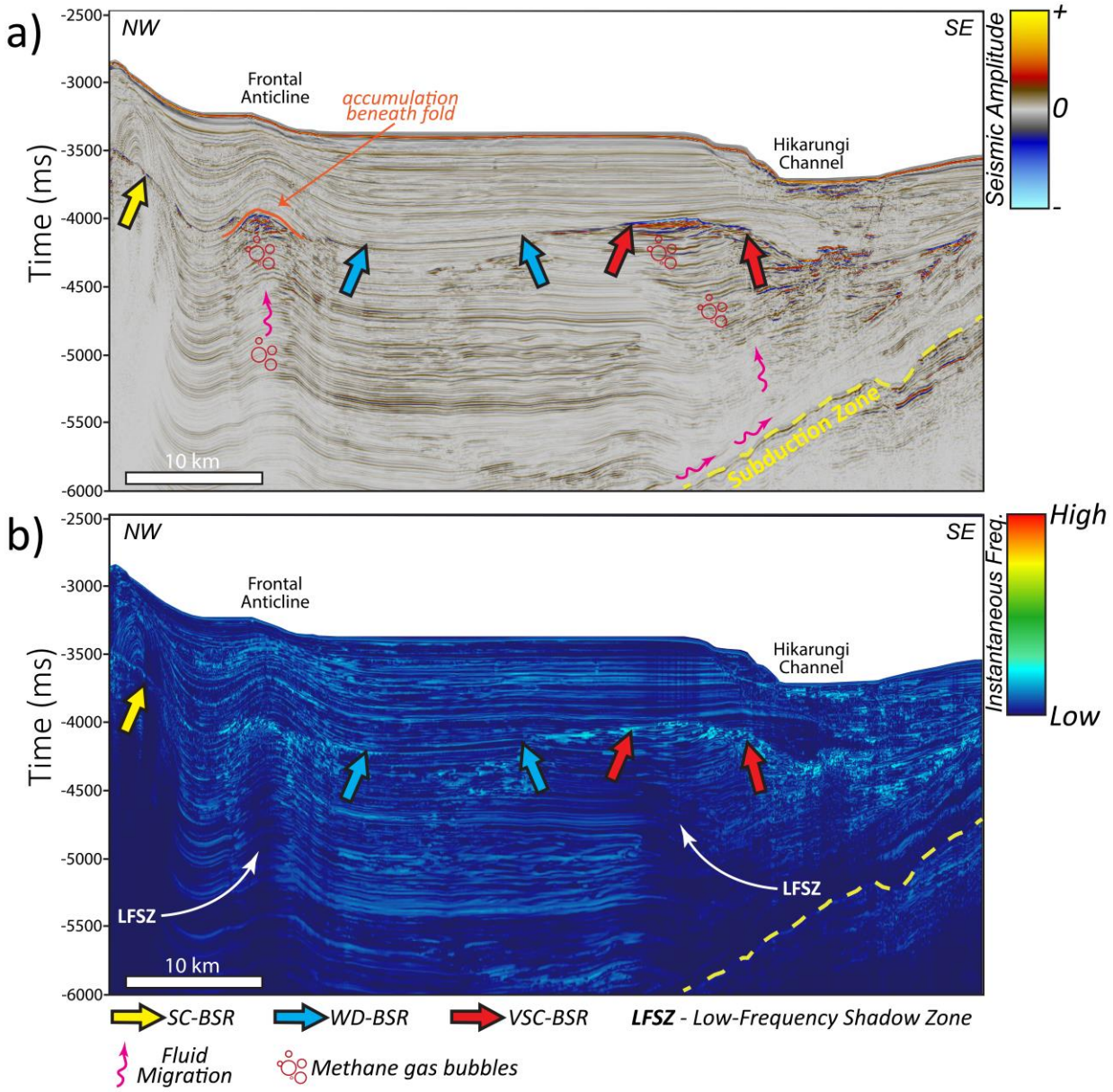

Figure 2-4. Seismic attributes used for the attribute analyses along PEG09-19 (a) amplitude, and (b) instantaneous frequency. The three types of BSRs described are indicated by the block-arrows. Note the low-frequency shadow zones (LFSZ) in (b) beneath the VSC-BSR and an anticline folded layer likely due to the potential accumulation of free gas.

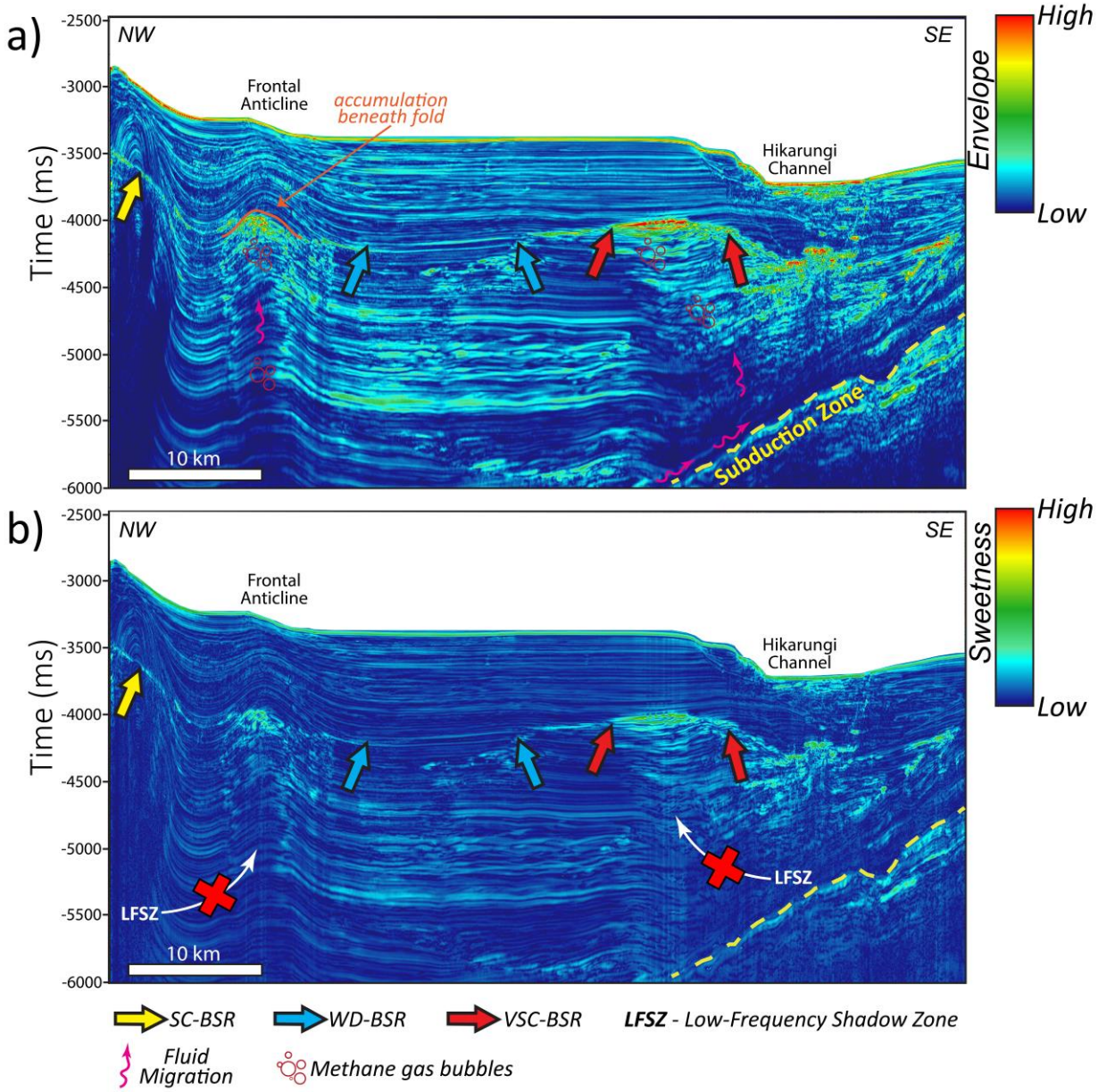

Figure 2-5. Seismic attributes used for the attribute analyses along PEG09-19: (a) envelope, and (b) sweetness. The three types of BSRs described are indicated by the block arrows. Because the instantaneous frequency is in the denominator of the sweetness attribute, the shadow zone seen in Figure 2-5b is now illuminated.

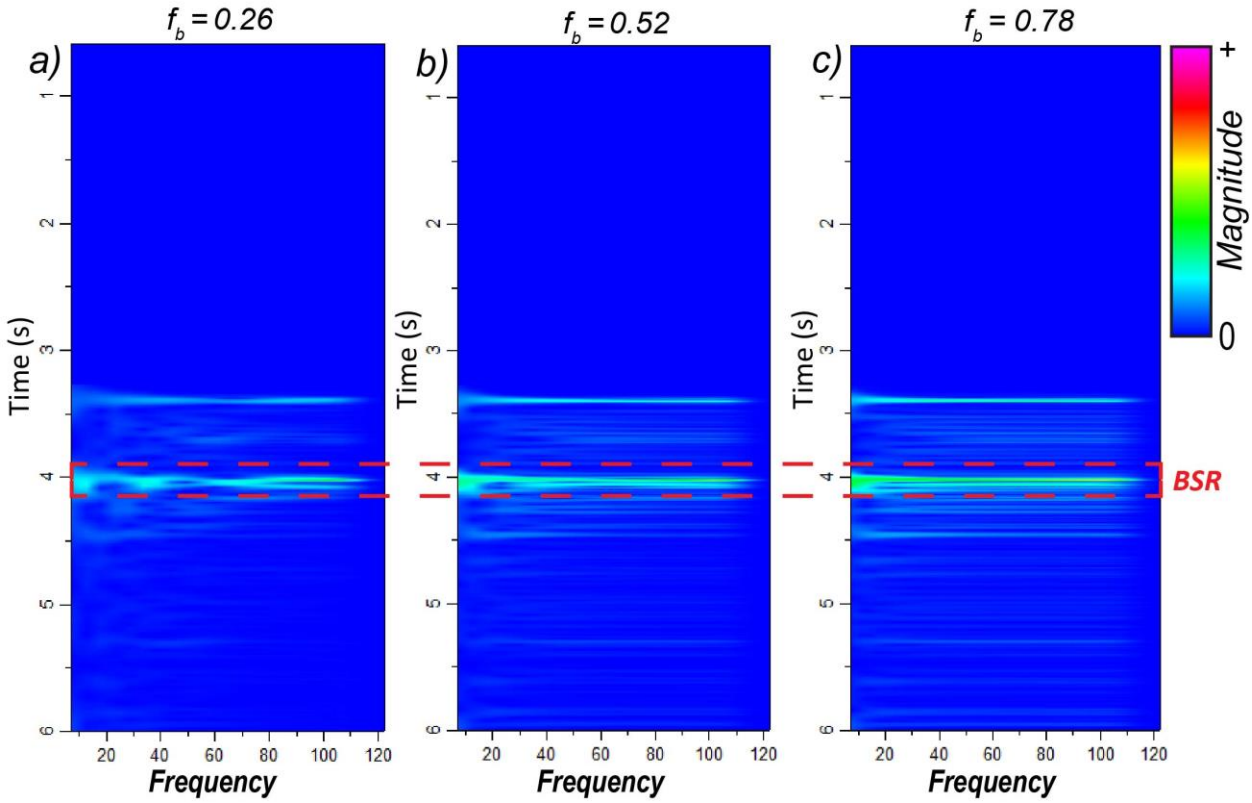

Figure 2-6. Time frequency panels for seismic Trace 4400 along PEG09-09 using different Morlet wavelet bandwidths f_b = (a) 0.26, (b) 0.52, (c) 0.78. For this trace, the BSR occurs approximately at a two-way travel time of 4 s.

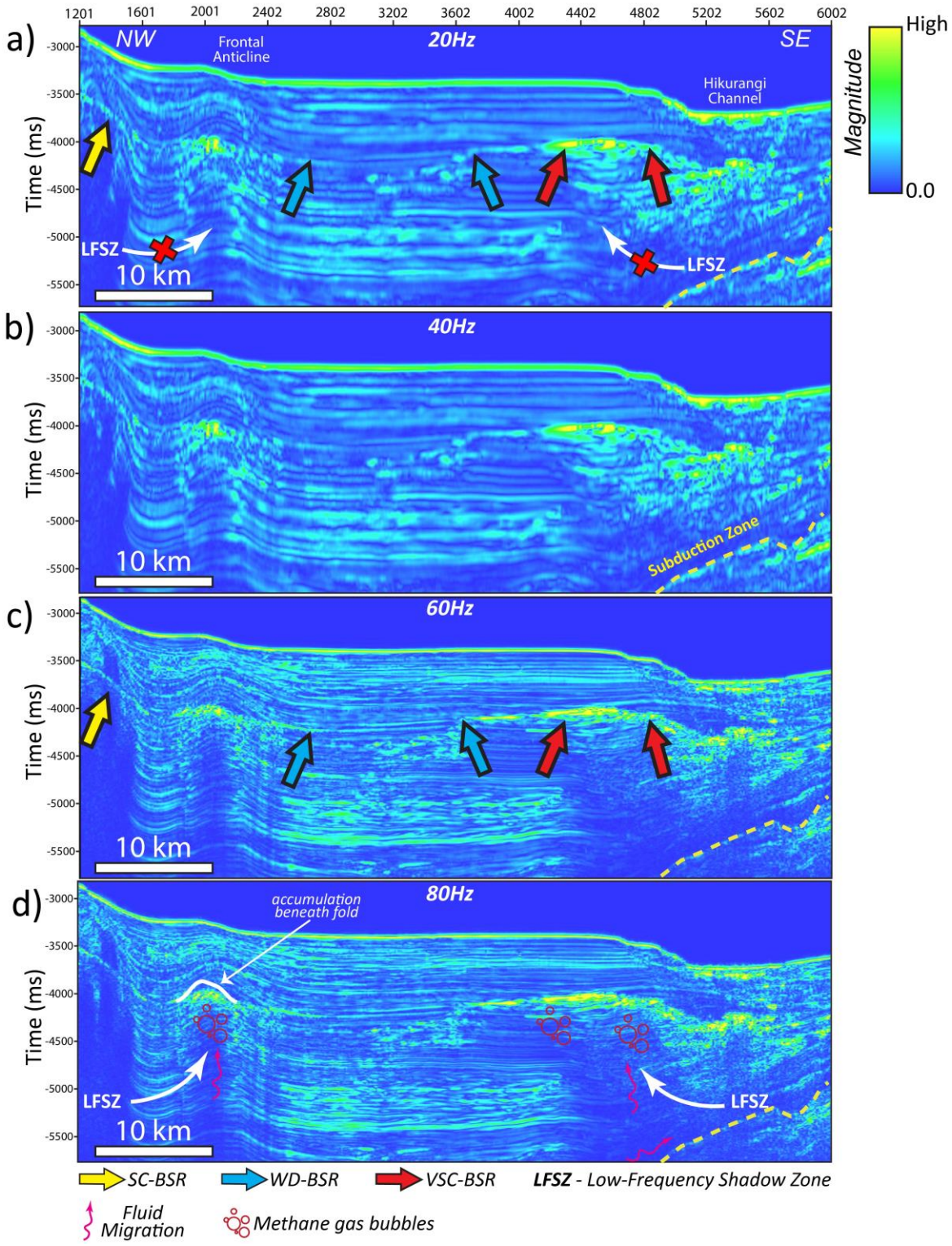

Figure 2-7. CWT spectral magnitude for the (a) 20Hz (b) 40Hz (c) 60Hz and (d) 80Hz frequency components along line PEG09-19. The three types of BSRs described are pointed by the box-arrows. Note the low-frequency shadow zones are better interpreted using higher frequency components in addition to the stronger seismic amplitude BSRs that exhibit larger magnitudes.

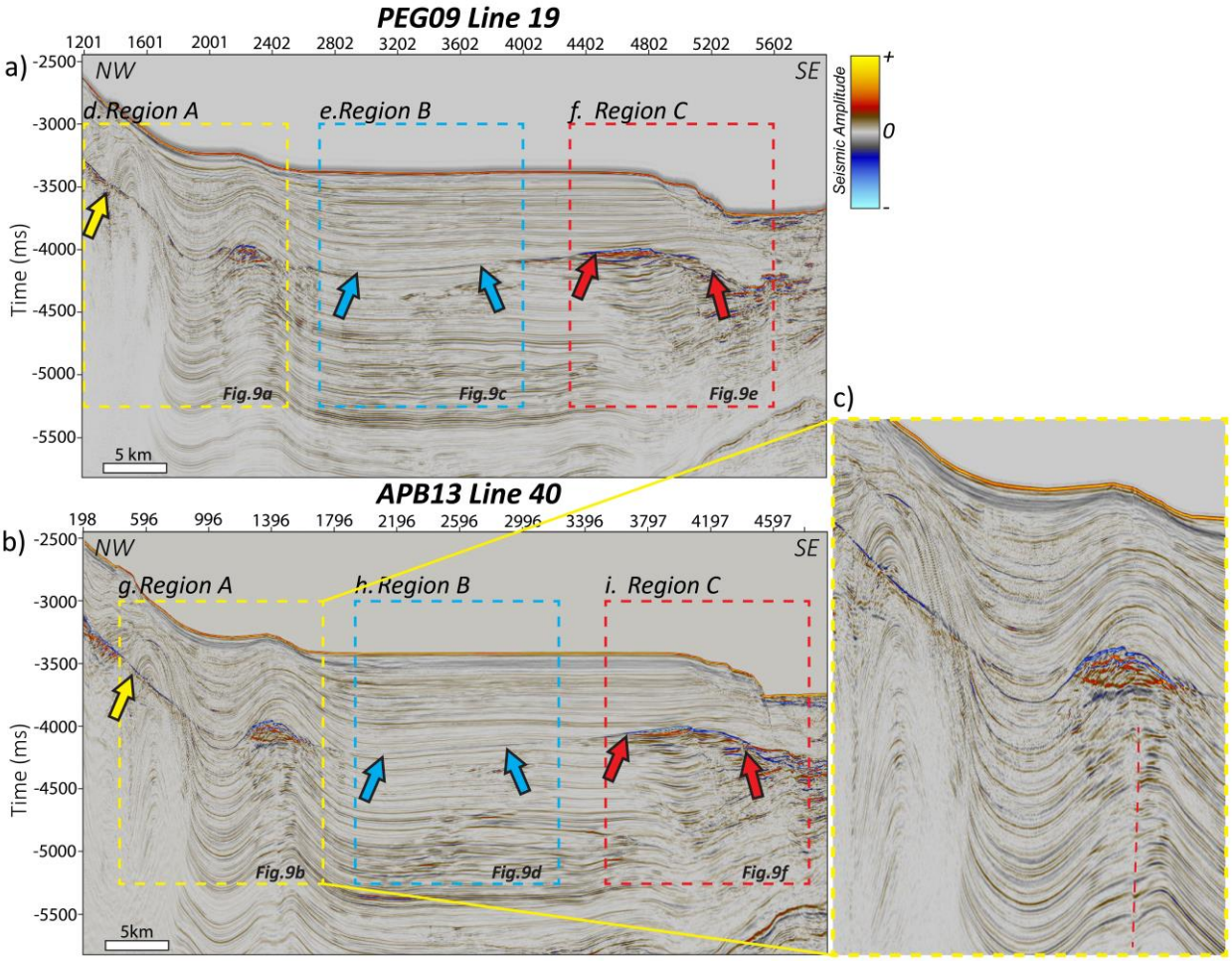

Figure 2-8. Seismic amplitude profiles of for the (a) PEG09-19 and (b) APB13-40 survey lines and the different regions consisting of the three types of BSRs described in this study. The two seismic surveys are compared for the direct attenuation measurement method to determine the transferability and performance of the method when using a higher resolution dataset (e.g. APB13 survey). Additionally, the zoom-in of (f) Region A for the APB13-40 line shows an interpreted fault beneath location of the Frontal Anticline, compared to the PEG09-19 line, where the fault is not easily discernable.

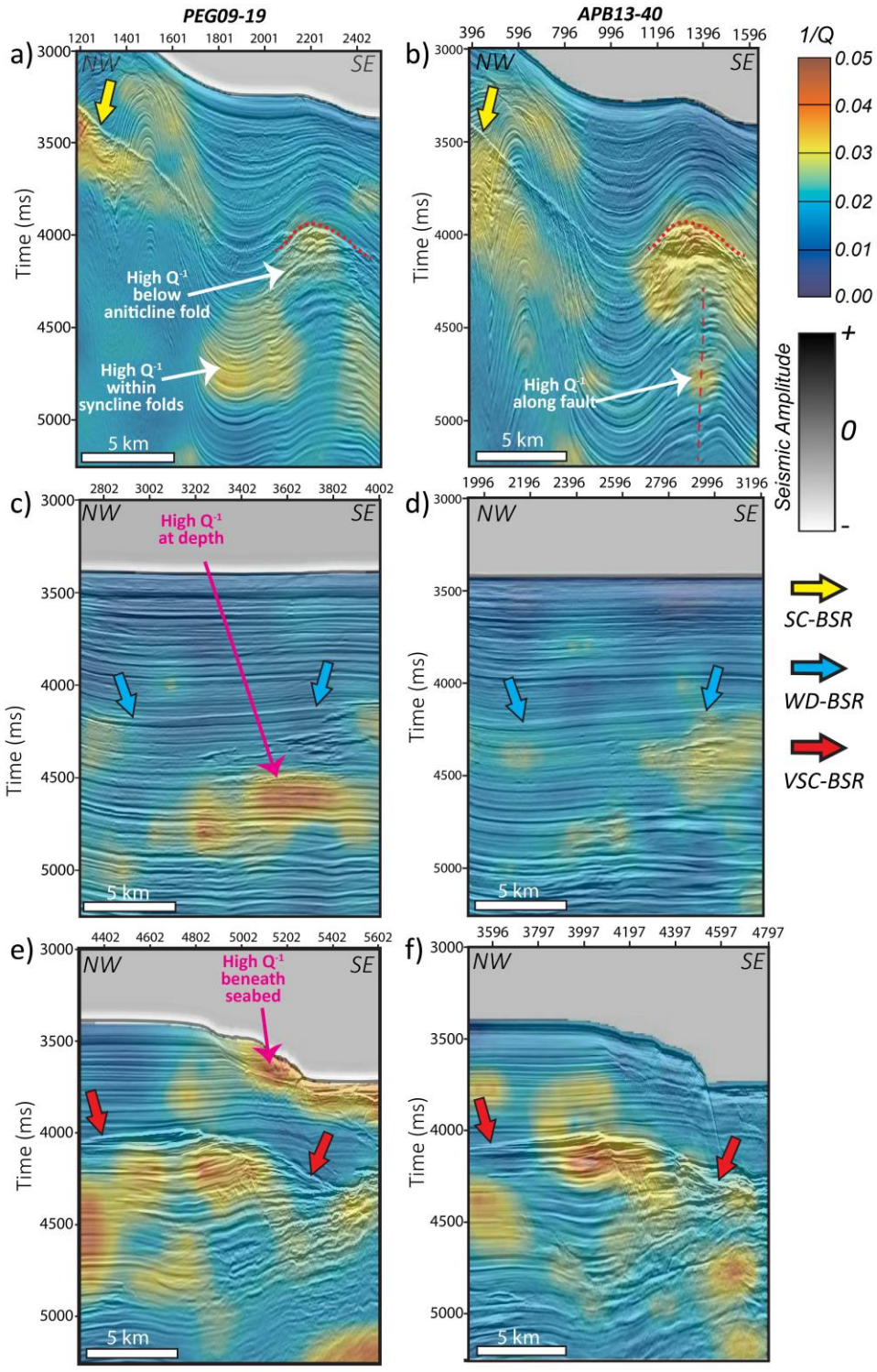

Figure 2-9. Seismic amplitude co-rendered with the seismic attenuation using the inverse quality factor Q^{-1} for the different types of BSRs describe in the study, for each of the lines along PEG09-19 and APB13-40. I interpret the regions of high attenuation to be due to the accumulation of free gas such as in the anticlinal features seen in (a) and (b) beneath the VSC-BSR near Hikurangi Channel in (e) and (f).

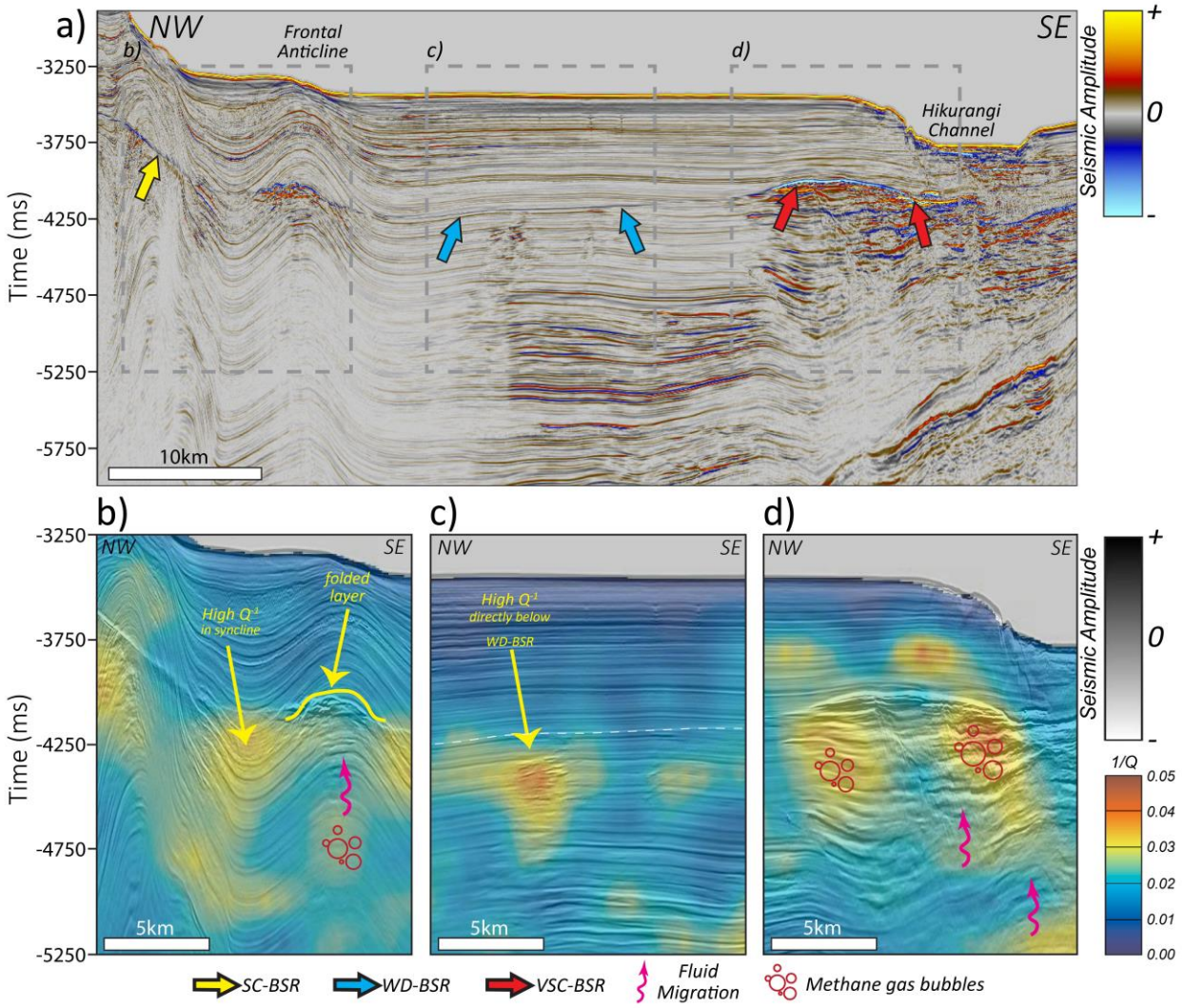

Figure 2-10. (a) Seismic amplitude and (b), (c), and (d) seismic-amplitude co-rendered with the seismic attenuation along APB13-42 using the inverse quality factor Q^{-1} for the different types of BSRs describe in the study. As in Figure 2-9, I attribute the high attenuation to free gas accumulation and distribution, especially beneath the (b) anticline folded layer and the (d) VSC-BSR near the Hikurangi Channel.

Figure 2-11. Location of the Alaminos Canyon Survey used in the Gulf of Mexico and few bathymetric features within the deep-water environment. *(Courtesy USGS)*

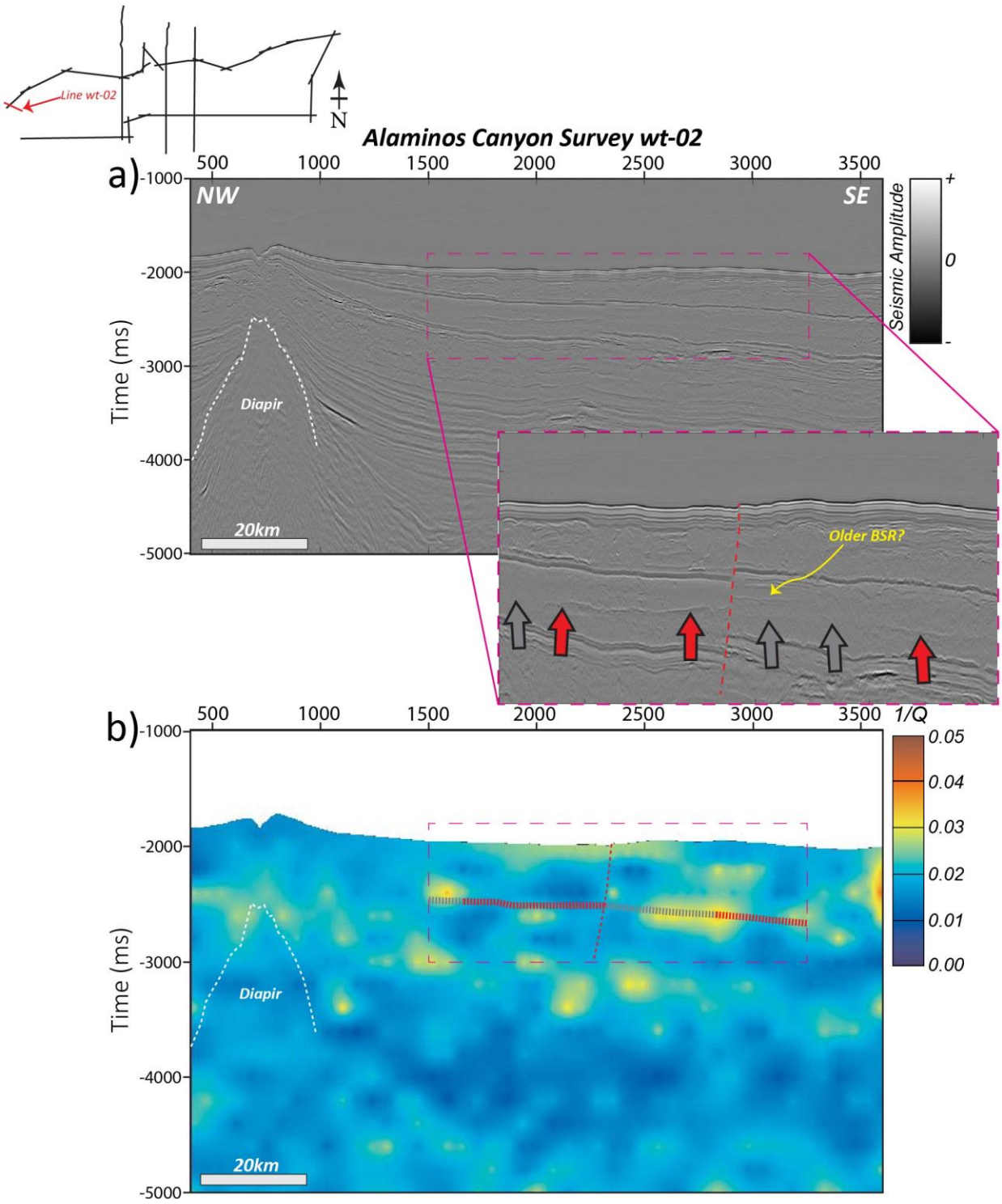

Figure 2-12. (a) Seismic amplitude compared with the (b) attenuation using the inverse quality factor Q^{-1} along line wt-02 in the Alaminos Canyon survey. Gray block arrows indicate the presence of a weak non-visible BSR and red block arrows indicate the presence of strong BSRs.

LIST OF TABLES

Table 2-1. Performance Summary of the 3 methods used. (X) indicates No, whereas (✓) indicates Yes.

Intended Application	Seismic Attribute		Continuous Wavelet Transform	Sparse Spike Decomposition
	Instantaneous Frequency	Sweetness		
As Direct GH Indicator	X	X	X	*Indirectly infers gas hydrate presence*
As a free gas Indicator	✓ *(via a LFSZ)*	X	✓ *(via a LFSZ)*	✓ *(High Attenuation)*
Discerning of strong BSRs	*Low-Medium response. Difficult to distinguish from background geology*	*High response*	*High Magnitude*	*High Attenuation*
Discerning of weak BSRs	*Weak attribute response. Difficult to distinguish from background geology.*	*Low Sweetness, but can somewhat be discerned.*	*Weak magnitudes. Difficult to distinguish from background geology.*	*Can potentially vary, (eg. The high attenuation associated with the weak/non BSR region along the Alaminos Canyon 2D Line).*

CHAPTER 3: CONCLUSIONS

In this dissertation, I examine the potential to improve the detection of gas hydrate and free gas accumulation in seismic data, utilizing a recently developed method known as Sparse-Spike Decomposition (SSD) that directly quantifies and measures the attenuation response, following the use of traditional seismic attribute application and spectral decomposition techniques.

In Chapter 2, we explore and discuss the traditional frequency attributes (i.e. instantaneous frequency and sweetness) that have been able to better image bottom-simulating reflectors (BSRs) in seismic data as well as seismic features associated with free gas accumulation known as low-frequency shadow zones (LFSZs). The next step which involved using the spectral decomposition continuous wavelet transform method is used to better improve the detection of the BSRs, which therefore proved to be a more accurate approach having more advantages to interpretation compared to the traditional frequency attributes. I showed that with the 3rd method (SSD) the results of the directly measured attenuation can help make several key observations of these hydrate systems. These observations include; (1) low-frequency shadow zones defined in seismic attributes and spectral decomposition coincide with high attenuation; (2) there is a strong relationship with the amplitude strength of the BSR and the attenuation response; (3) the inverse Q (Q^{-1}) can reveal potential fluid migration pathways and (4) there is no direct relationship between the attenuation response and hydrate bearing sediment. In response to the last observation, we can however infer the potential presence gas hydrates due to the response of free gas. Not only do we identify that the SSD can indirectly infer gas hydrates especially where strong BSRs are present, but it is apparent that for weak BSRs the results are variable, which can therefore be attribute to differences in lithology. This comment follows the results observed in the Alaminos Canyon survey where the weak seismic BSR coincided with a significant attenuation response. With

respect to the objectives of this study we can conclude that; (1) sweetness attribute and spectral decomposition (cwt) improves BSR detection compared to instantaneous frequency; (2) the attenuation method does not provide a direct relationship to gas hydrate presence, however hydrates can be inferred indirectly because of the attenuation response associated with free gas, specifically in the regions surrounding the strong continuous (SC) and very strong continuous (VSC) BSRs; (3) the attributes and the cwt method correlates with the attenuation method such that there is a strong relationship between low frequency shadow zones and high attenuation, especially beneath strong reflections; (4) we can make inferences on the free gas migration and accumulation from attenuation, strongly supported by previous interpretations of the region; (5) The application to other areas of interest seem promising, however more constraints on the subsurface features and geology are necessary to implement a more robust approach.

Future work would include several key approaches to validate the efficiency of this method. These include; (i) an in-depth analysis of the lithology and how it affects the attenuation response using data from other continental margin basins or beneath permafrost, (ii) exploring how the attenuation measurements are influenced by the amplitude spectrum of the seismic data and its dominant frequency, (iii) an opportunity to compare the seismic attenuation results to other available data such as core, well logs and VSP to name a few and (iv) testing the attenuation method on time or depth migrated angle stack data.

APPENDIX A

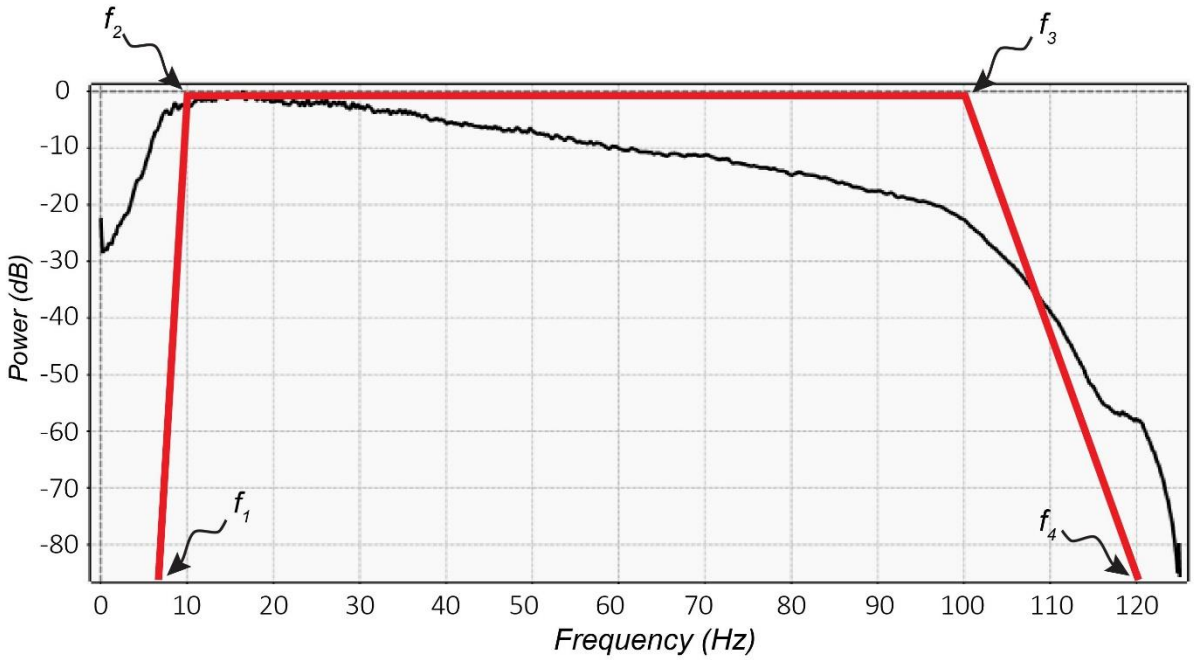

Figure A-1. Amplitude spectrum of seismic Pegasus Line 19 and a schematic of an Ormsby filter with cut off frequencies f1, f2, f3 and f4 used for the continuous wavelet transform.

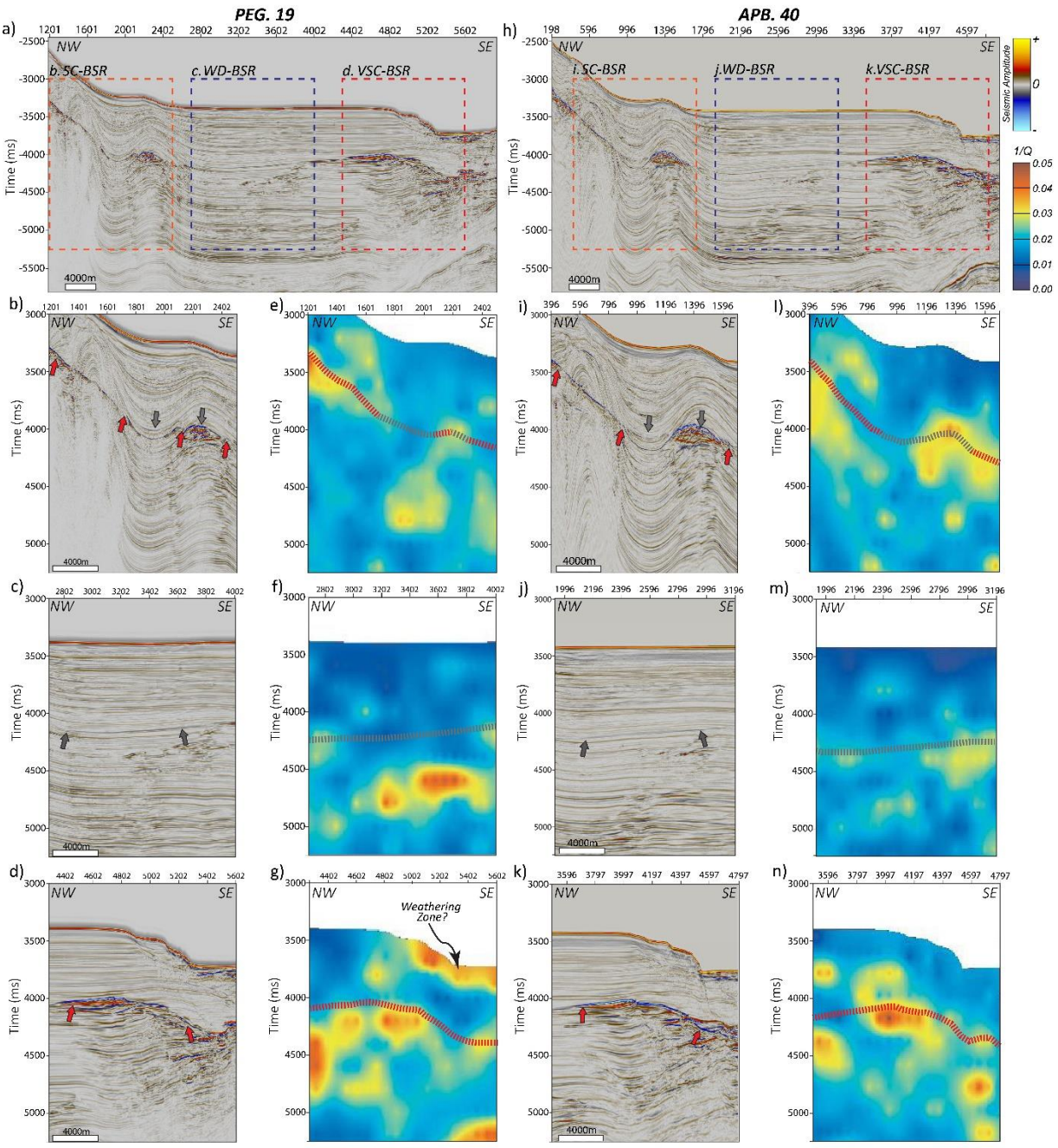

Figure A-2. Seismic amplitude compared with the seismic attenuation using the inverse quality factor Q^{-1} for the different types of BSRs describe in the study, for each of the surveys along Peg09-19 (a-g) and APB13-40 (h-n). The gray arrows and dashed lines represent the weak/non visible BSR trends whereas the red arrows and train lines represent the strong BSR trends.

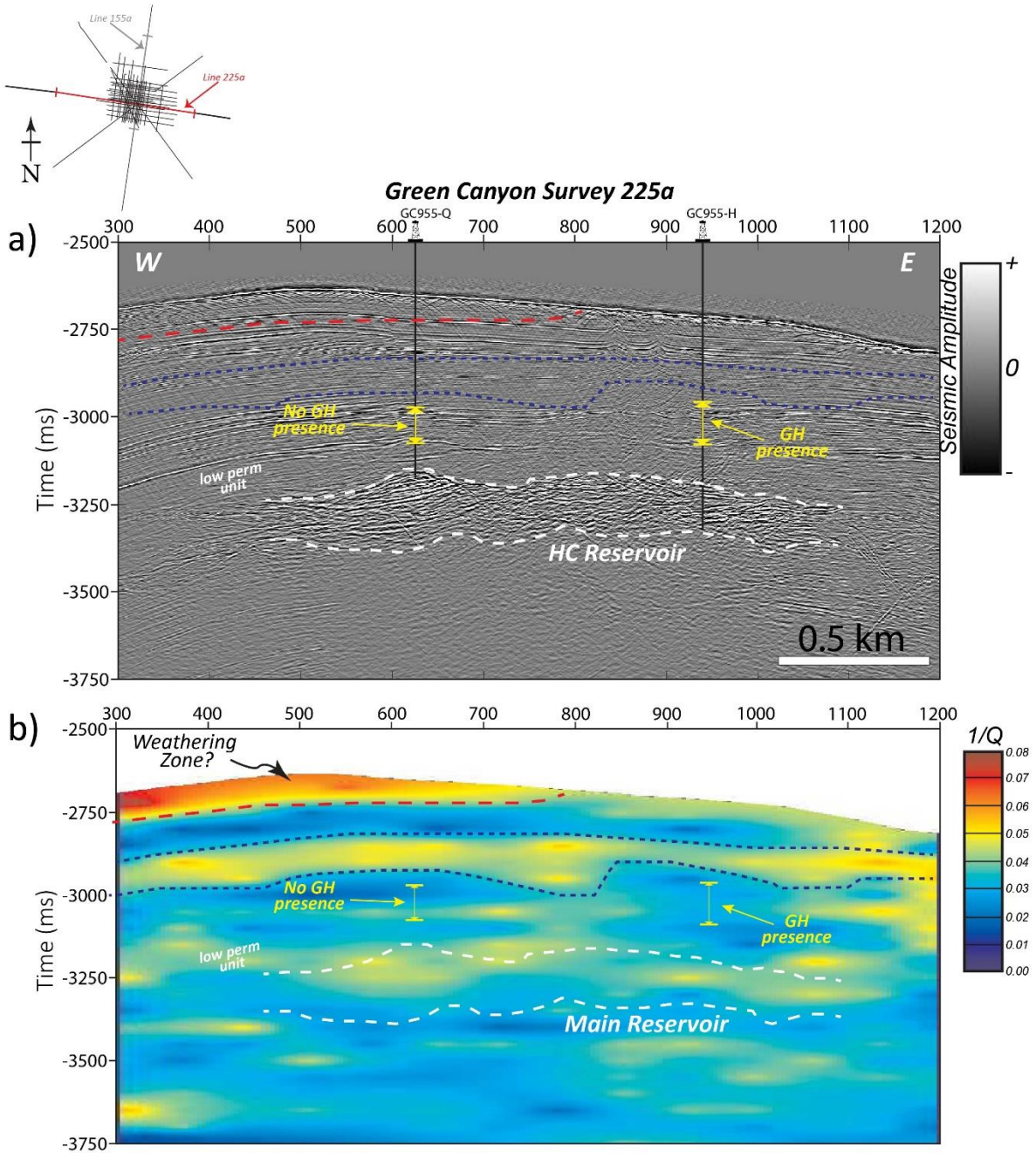

Figure A-3. (a) Seismic amplitude and (b) attenuation using the inverse quality factor Q^{-1} along Line 255a in the Green Canyon 955 survey. The interpretations of the main reservoir, low permeability unit and GH and non-GH presence along two wells in the area, are adopted from Haines et al. (2017).

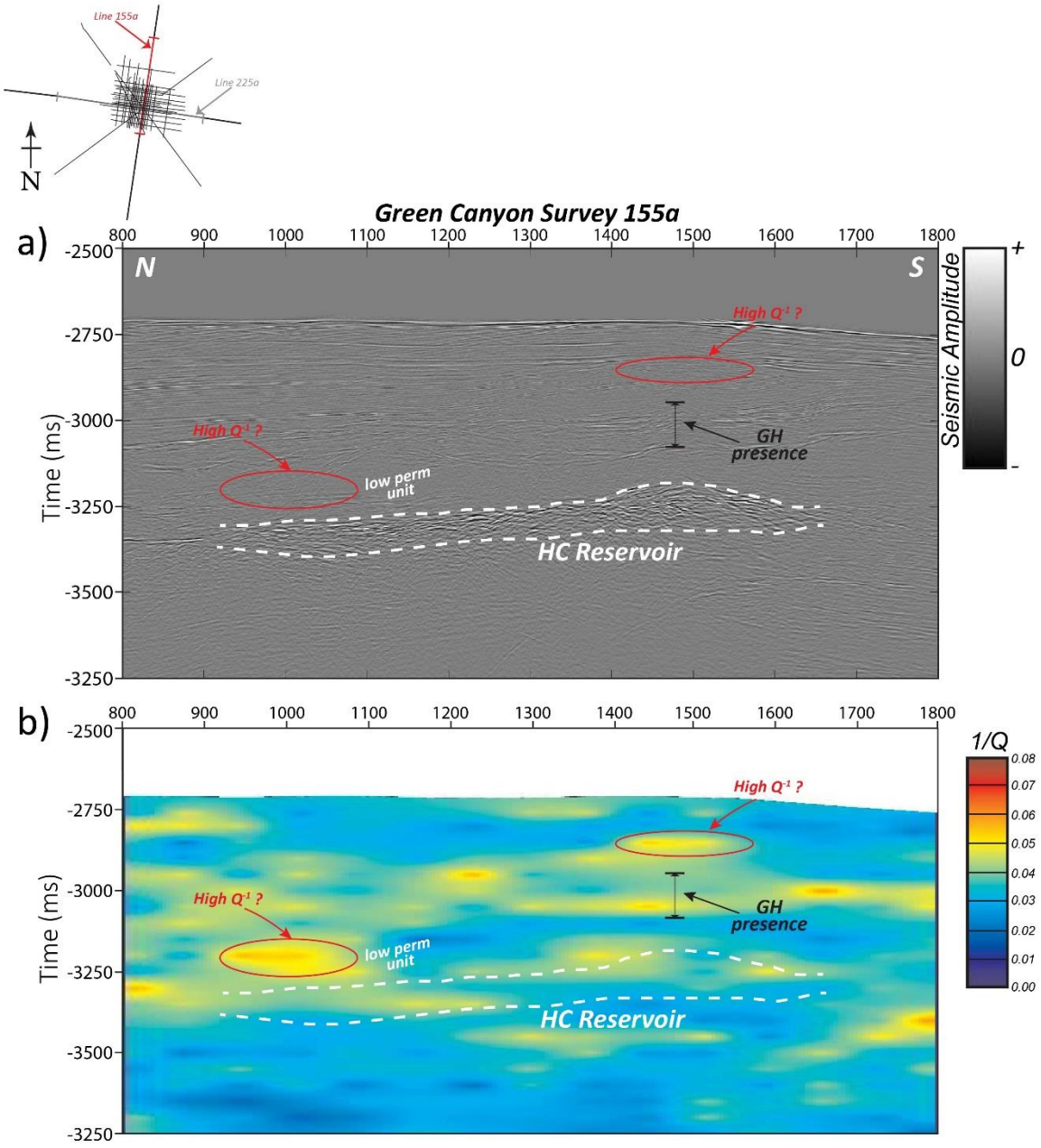

Figure A-4. (a)Seismic amplitude compared with the (b) attenuation using the inverse quality factor Q^{-1} along Line 155a in the Green Canyon 955, GOM survey. The interpretations of the main reservoir, low permeability unit and GH and non-GH presence along two wells in the area, are adopted from those of Haines et al. (2017).

APPENDIX B

Controls of Pre-existing Structures on Clinoform Architecture and the Associated Progradational System Elements

Roberto Clairmont[1]*, Folarin Kolawole[1], Abah P. Omale[2], Heather Bedle[1]

[1]*School of Geology and Geophysics, University of Oklahoma, 100 East Boyd Street, RM 710, Norman, OK 73019, U.S.A.*

[2]*Department of Geology & Geophysics, Louisiana State University, E235 Howe Russell Kniffen, Baton Rouge, LA 70803, U.S.A.*

This section was published online on 12 July 2020 in the Basin Research.

DOI: 10.1111/bre.12487.

ABSTRACT

There remains a limited understanding of the controls of preexisting structures on the architecture of deep-water progradational sequences. In the Northern Taranaki Basin (NTB), New Zealand, Pliocene post-extensional sedimentary sequences overlie Miocene back-arc volcaniclastic units. We utilize seismic reflection datasets to investigate the relationships between the buried back-arc mound-shaped structures, and the spatio-temporal changes in clinoform architecture and the associated progradational system elements within the overlying continental slope margin sequences. Our results reveal: (1.) buried mound shape structures in the northern domain of the study area, overlain by younging progression of shelf-to-basin prograding clinoforms; (2.) folding of the deeper clinoforms that systematically decrease in magnitude with shallowing depth from the top of the seamounts; (3.) overall, the N-S-trending continental slope margin evolves from a highly curvilinear/angular trend in the deeper clinoforms (Units 1-2) into a rectilinear geometry within the shallower post-extensional intervals (Unit-3 and shallower); (4.) Units 1-2 characterized by

dominance of stacked offlap breaks and over-steepened (7-10°) clinoform foreset slopes in the northern domain, and dominance of gently dipping foreset slopes (<6°) in the south; (5.) Unit-3 show very low (<5°) and intermediate (5-7°) foreset slopes across the entire survey; (6.) in the northern domain, differential loading by prograding sequences about the buried seamounts and horst-graben structures induced a differential compaction of the deeper units, which influenced a temporal pinning of the prograding slope margin in pre- Unit-2 times; and (7.) wide, closely-spaced channel incision into over-steepened slopes dominate the deeper prograding sequence in the northern domain, whereas, narrower, straighter channels dominate the south. We show that the buried preexisting structures constitute rigid buttresses that modulated the syn-depositional topography and post-depositional architecture of the prograding sequences in the NTB. Our findings present a distinction in the controls on progradational sedimentation patterns between magmatic and non-magmatic continental margins.

Keywords: Clinoforms, Sedimentation patterns, Paleovolcanoes, Deepwater, Extensional margins, Shelf-margin, Igneous-structures

INTRODUCTION

Few studies have intensively explored the potential link between buried structural features and their influence on subsequent sedimentary sequences (Hardage et al., 1996; Tsikalas, et al., 1998; Anka et al., 2009; Alves, 2010; Johnston et al., 2010). This leaves much in question as to the influence of pre-existing structures on the basinal sedimentation patterns associated with eustatic sea level changes, climate, and tectonic-related events. The purpose of this study is to examine how inherited paleovolcanic edifices alter the architectural elements, geometry and other large-scale features of the overlying, prograding strata (clinoform packages). Several studies have

analyzed the intricate internal architecture, depositional sequences, and potential economic significance of clinoforms (e.g., Hansen and Kamp, 2006; Berton et al., 2016; Salazar et al., 2016). However, the controls of inherited tectonic structures on clinoform architecture remain a longstanding problem.

Clinoforms encompass multi-scale (tens of meters to kilometers) sloping depositional surfaces that are associated with the progradation of sediments in deltaic environments and continental shelf settings (Mitchum, 1977; Patruno and Helland-Hansen, 2018). Due to the regionally extensive nature of continental-shelf margins, clinoforms provide a great opportunity to pin-point the salient features that potentially indicate the influences of buried structural features. Three distinct geometrical sections that characterize a clinoform package include topsets, foresets and bottomsets, describing their erosional and depositional basin-ward structure. Progradational system elements are largely controlled by sediment supply, however, eustatic sea level changes and tectonism may influence the associated sedimentation patterns and therefore the shape of clinoform profiles (e.g., Emery and Myers, 1996).

Buried structural features may influence the morphology of the earth's surface and the associated sedimentation processes (e.g., Gomes et al., 2014; Mortimer et al., 2016). Many studies implicate that igneous activities may deform the shallow crust and modify the surface morphology at the time of emplacement (e.g., Bridgwater et al., 1974; Feuillet et al., 2002; Hansen and Cartwright, 2006; Muirhead et al., 2012; Holford et al., 2012; Jackson et al., 2013; Magee et al., 2016, 2018; Reynolds et al., 2018; Kolawole et al., 2020). Post-emplacement, igneous edifices may influence seabed sedimentation, and local distribution of crustal load and geometry of the subsequent sedimentary successions (e.g., Infante-Paez and Marfurt, 2017; Infante-Paez, 2018; Jackson et al., 2019).

In the northernmost Taranaki Basin, New Zealand (Figures B-1a-c), shallower Early Pliocene sedimentary sequences are characterized by an excellent stacked succession of laterally outbuilding sequences that overlie Middle to Late Miocene back-arc extension volcaniclastic sequences, Mohakatino Volcanic Complex (Stagpoole and Nicol, 2008; Giba et al., 2010, 2013). The region of the volcanic edifices, observed in seismic reflection data along the western continental shelf of the North Island (Giba et al., 2013), provide an excellent location to explore the influence of the igneous structures on the geometry of the migrating shelf margin and therefore clinoform sequence stratigraphy and the associated progradational system elements.

In this study, we utilize seismic reflection datasets to analyze the spatio-temporal variations in the architecture of the post-extension progradational sequences that overlie inherited syn-back-arc extension seamounts. We show that in this region of the Taranaki Basin, differential loading by the overriding clinoform sequences about buried seamounts and horst-graben structures induced a differential compaction of the deeper units which modulated the syn-depositional location and geometry of the deeper clinoform sequence boundaries, and post-depositional geometries of the clinoform packages. Further, our findings present a distinction in the controls on progradational sedimentation patterns between magmatic and non-magmatic continental margins (both convergent and divergent).

GEOLOGICAL SETTING

Pre- Middle Miocene

The Taranaki Basin evolved as a rift basin during the Late Cretaceous as the New Zealand continent separated from Gondwanaland (Stagpoole et al., 2001), and continued to experience extension up till the Late Paleocene (Palmer, 1985). It formed as a result of the subduction of the

Pacific Plate beneath the Australian Plate about ~40 myr ago (Giba et al., 2013; Stagpoole and Nicol, 2008; Seebeck et al., 2014), where both plates converge at the Hikurangi Trough (See Figure B-1a inset), which runs south to north, toward the eastern end of the island (Giba et al., 2010). The Hikurangi subduction margin initially had a NW-SE trend (Giba et al 2013; King, 2000) eventually orienting to a NE-SW trend. The basin is situated on the overriding Australian Plate and is located on the western coast of the North Island (Figure B-1a), is approximately 60km wide and extends for about 350 km in a NNE direction from the south Taranaki Peninsula to the offshore coast, west of Auckland (Giba et al., 2010). The structure of the basin is separated into two main components, the Western Stable Platform and the Eastern Mobile Belt (King and Thrasher, 1996) and is non-distinctly bounded by the Northland Basin to the north and the Deepwater Taranaki Basin to the west.

In the Oligocene to Early Miocene period, the Hikurangi subduction margin, which began to develop between the convergent event of the Pacific and Australian plates (Uruski and Baillie, 2004), caused the Taranaki Basin to transition from an extensional tectonic setting into a contractional tectonic domain (King, 2000). Primarily, a 50-degree rotation, about a vertical axis, of the Australian Plate (~24 myr) was accompanied by steepening of the westerly subducting Pacific Plate (Giba et al., 2010, 2013; Kamp, 1984). This clockwise vertical rotation of the North Island, of New Zealand, was then followed by north and west extension and south and east shortening of the Australian plate (Giba et al., 2013; Nicol et al. 2007). The northern region of the basin then witnessed the development of andesitic volcanism and intra-arc/back-arc extension in Early Miocene, corresponding to the subduction (Stagpoole et al., 2001, Herzer 1995). This is a result of dehydration of the westward subduction Pacific Plate (Seebeck, 2012; Bischoff et al., 2017) and/or partial melting of the plate (King, 2000). This magmatic event led to the emplacement

of the NNE-SSW-trending Mohakatino Volcanic Belt (MVB) in the northern Taranaki Basin (Figures B-1a and B-1c), consisting of mainly submarine volcanic centers (Giba et al., 2010 and 2013; Seebeck, 2012). Additionally, the MVB has over 20 volcanic centers, covering an area of ca. 3200km^2 (Lodwick et al., 2019), stretching a distance of about 200km, from the northern coastal area of the Taranaki Peninsula (See Figure B-1a).

Late Miocene - Early Pliocene

Late Miocene to Pliocene activity in much of the Northern Taranaki Basin involved back-arc extension tectonics associated with the Hikurangi subduction zone of the Australian-Pacific plate margins. Extensional faulting within the basin formed a c. 40km wide depocenter, known as the Northern Taranaki Graben (Hansen and Kamp, 2004a, 2004b), bordered between the Turi Fault Zone and Cape Egmont Fault Zone (Stagpoole et al., 2001). The graben occupies an area of 10,000 km^2. Hansen and Kamp (2004a) observed Late Miocene to early Pliocene stratigraphic units formed deep within the structural formation of a Northern Graben and below the onset of the Giant Foresets Formation (GFF). These stratigraphic units have been characterized as the Ariki Formation and the Early Pliocene basin floor fan of the Mangaa Formation, respectively (Hansen and Kamp, 2004a). The Ariki Formation is a marly condensed interval related to the starvation of terrigenous sediment to the northern parts of the basin and the Mangaa Formation is a thick sandstone-dominated unit (Hansen and Kamp, 2002, 2004a). The structural limits of the Northern Graben and its continuing extension affected the depositional environment during local chronostratigraphic stages of the Waipipian (3.5 – 2.79 Ma) to Mangapanian (2.79-2.28 Ma), in early Pliocene; together with the existence of volcanic massifs of the Mohakatino Formation that

influenced the way the paleogeography would affect siliciclastic sediment accumulation (Hansen and Kamp, 2002, 2004b).

Middle Pliocene to Recent

In the late local chronostratigraphic stage of the Nukumaruan (1.8 – 0.33 Ma), structural influence of the graben maintained and aligned the deposition of material in a sloping SE to NW direction, with little impact of subsidence on sedimentation (Hansen and Kamp, 2004a). Substantial voluminous sediment was then supplied to the adjacent sedimentary basins, as the southwest-dipping subduction zone of the northern region of New Zealand uplifted and exposed parts of Zealandia in the Neogene (Nicol et al., 2007; Bischoff et al., 2017). The source of the deposited sediment supply would be derived from the uplifted Southern Alps created <8 Myr ago (Tippet and Kamp, 1995). In the Pliocene and Pleistocene, the Taranaki basin would then be filled with sediment associated with the Giant Foresets Formation, which prograded at rapid rates in a north and predominantly westward direction, building onto the undisturbed Western Stable Platform (Giba et al., 2010, 2013; Stagpoole et al., 2001) as the rate of uplift increased. This sequence of sedimentation filled the Northern Taranaki Graben with a thick succession of deep-water sediments (Bischoff et al., 2017) and continued to bury the Miocene aged MVB volcanic seamounts (Stagpoole et al., 2001) within the last ~20 myr. Thicker units of the GFF would be expected within the graben, due to subsidence and syn-sedimentary tectonics (Hansen and Kamp, 2004a). Additionally, the GFF is predominantly characterized by low-angle shelf-edge trajectories (Anell and Midtkandal, 2017). This regional formation is the result of rapid progradation and aggradation of late-early Pliocene to relatively recent succession of the continental margin that underlies the modern shelf-to-basin ward structure (Hansen and Kamp, 2002).

Seismic interpretation studies reveal the varying litho-facies and geometrical elements of the GFF. Its top-sets are indicative of coarser grained sandstone and muddy siltstone; the foresets include an accumulation of fine-grained mudstone and muddy siltstone, with variability in its lithology along the degradational surface and the bottom-sets are described as being composed of either sandstone or mudstone (Hansen and Kamp, 2002). The observation of the GFF in seismic data reveal no distinct geological boundary northward, into the southern part of the Northland Basin. Johnston (2010) have provided potential evidence of progradational successions in the southern region of the Northlands basin due to growth of the shelf margin in the Pliocene that overlay the buried volcanic massifs.

DATA AND METHODS

Seismic survey and well data

To address the onset and evolution of the progradational events including the GFF, the 3-D Nimitz survey was selected for analysis. The survey which was acquired by the Swire Pacific Offshore owned vessel, Pacific Titan, was operated by Compagnie Générale de Géophysique (CGG) from January through April 2007. It is located along the western coast of the North Island New Zealand (Figure 1a) covers approximately 432 km^2 and provides a recording length of 6500 ms (O'Leary et al., 2010). Inline and crossline interval dimensions are measured at 25 meters and 12.5 meters, respectively. The data has SEG positive display polarity, correlating impedance increases with positive amplitude reflection and the recorded sampling rate is 2 ms. Quality Control (QC) processing was conducted to determine issues associated with acquisition and recording for every line and to determine the impact of noise on the data. For example, a bulk shift static correction was applied to the seismic data to correct for a 50 ms delay in instrument recording, true amplitude

recovery was applied using a spherical divergence correction, band pass filtering was also performed, followed by NMO (Normal-Moveout) and stacking (O'Leary et al., 2010).

Prior to seismic interpretation, we utilized the Korimako-1 well (Figure B-1b) to perform the seismic-to-well tie and complete a time to depth conversion of the seismic dataset. We tie the well to the seismic to get the interval velocities, and using the interpreted horizons and well-log velocity information, created a P-wave model. The P-wave interval velocity model was then used to convert the seismic to depth. Time-depth curves from sonic data used to create the synthetic seismograms (O'Leary et al., 2010) indicate an average velocity of 1710m/s from the top of the log at 454.6 m and a Mean Sea Level (MSL) datum. Given that we observe a dominant seismic frequency of approximately 20 Hz, this provides vertical (1/4 wavelength) resolution of ~21m.

As a wildcat exploration well, its intended goal was to target sands similar to the Miocene Mangaa Formation. Drilling of the Korimako-1 well dated between October-November 2010, and reached a maximum penetration depth of 1946 m. Unfortunately, the well turned out to show no significant economic impact, and was therefore abandoned. The results revealed high risk AVO (Amplitude versus offset) and amplitude anomalous targets within the Pliocene-Miocene strata linked to differences in the properties of shale, mistaken for potential reservoirs. We utilize stratigraphic markers and the associated ages from the Korimako-1 well-completion reports (O'Leary et al., 2010) to aid in constraining the ages of major stratigraphic surfaces in the survey.

Seismic interpretation methods

We use conventional seismic data interpretation techniques and 3-D seismic attributes to investigate the geological features in the 3-D Nimitz survey. Although seismic resolution of the seismic acquisition provides ~5 TWTs of seismic imaging, seismic interpretation was limited to

the seismic reflection data above 1.6 TWTs in addition to the underlying dome-shaped structures just below 1.6 TWTs. Herein, we use the terms “clinoforms” and “clinothems” respectively as chronostratigraphic horizons (surfaces traced by single amplitude reflectors) and the deposited features contained by these surfaces (Slingerland et al., 2008). We delineate the clinothems (clinoform packages) using continuous high-impedance reflectors in a shelf-to-basinward direction similar to published approaches (Anell and Midtkandal, 2017; Gomis-Cartesio et al., 2018). We utilize standard seismic facies analyses techniques (Berton and Vesely, 2016) and simple seismic stratigraphic terminology (Vail, 1987; Steel and Olsen, 2002) to interpret the clinothems, their architectural elements, and the associated progradational system elements. A two-dimensional (2-D) seismic transect (CNL95B-38) line is also included to indicate the regional extent of the studied GFF (See Figures B-1a and B-2a).

We use a bottom-up approach in our structural and stratigraphic mapping. First, we map the reflector bounding a deep-seated buried mound-shaped feature in the survey. Afterward, we map four strongly basin-ward-dipping, high impedance reflectors (R1 to R4). These reflectors bound packages of the same geometries (U1 to U3), (Figures B-2b and B-2c). Moreover, the reflectors, observed as the clinoform surfaces were mapped throughout the 3-D volume. We use these surfaces as key horizons delineating the regional changes in pale-topography and clinoform architecture from north to south across the survey. To better understand temporal evolution of the geometry and location of these key surfaces, as the extents of coverage of our dataset allow, we quantify the maximum foreset dip angle or “maximum foreset angle” (Figure B-3a), and the location of the toe of the continental slope/top of the continental rise (Figure B-3b), herein used as the “toe-of-slope inflection point”. The former indicates the maximum angle measured along the clinoform surface in the foreset region, while the latter indicates the first noticeable change in

angle upslope (i.e. base of the slope). O'Grady and Syvitski (2002) define the base of the slope as a point in which there is a significant decrease in the dip of the slope, which can be generally difficult to define due to less dramatic changes and inconsistency along the lower margins. Additionally, the continental rise has been defined as a uniform gentle sloping surface that lies at the base of the continental slope, in the absence of trenches (Heezen et al., 1996), on which mainly terrigenous sediment is deposited at high rates (Heezen et al., 1996; Murdmaa et al., 2012). We take these two measurements along five profile transects spaced 6 km apart (L1-L5).

We compute standard 3-D seismic attributes and surface-extracted displays to map the sedimentary dispersal features (e.g., channels, mass transport deposits etc.) along the mapped dipping reflectors. More specifically, we use the structural curvature, variance (coherence), and root-mean-square (rms) amplitude seismic attributes. Curvature is the 2D second-order derivative of both the inline and crossline components of the calculated dip; hence structural curvature is the 2D second-order derivation of the structural component of the reflections along vertical seismic (Chopra and Marfurt, 2013). It is particularly useful in identifying and constraining channel geometries, faults and fracture intensities. Variance is an edge detection method that uses local variance as a measure of unconformity in signal traces (Randen et al., 2001). The Variance attribute is used to identify fault trends and discontinuities in the seismic character derived from potential erosional features. Root-mean-square (RMS) amplitude is the square root of the sum of the square of amplitude values within a window length (Chen and Sidney, 1997; Chopra and Marfurt 2008). RMS amplitude aids in interpretation since it can differentiate areas with changes in acoustic impedance associated with lithological variations such as fluid content, and sand and shale contrasts in siliciclastic regions (Amonpantang et al., 2019). It is therefore useful in revealing channel morphologies (Amonpantang et al., 2019), basin floor fans, and depositional features such as mass transport

deposits, slump deposits and shale drapes/debris flow (Gong et al., 2011). Lastly, due to the dipping foreset successions and lack of clear reflections within the clinothems in the Nimitz 3D dataset, we apply the stratal slicing method to explore the spatio-temporal evolution of the analyzed stratigraphic units (Figure B-2c). Using two non-parallel dipping clinoform surfaces, a total of nine (9) stratal slices within each unit were generated and investigated (Figure B-2c).

Modelling of stratigraphic decompaction

Further, to better understand the influences of deeper rigid blocks (e.g., buried volcanic edifices) on the overlying clinoform geometries and architecture, we investigate the role of differential compaction on the 2-D spatio-temporal distribution of lithologic unit thicknesses. To evaluate the timing and magnitude of differential compaction about the buried volcanoes, we carry out 2-D decompaction on six layers identified within a representative seismic cross-section in the northern part of the survey. Decompaction reverses the porosity loss and reduced thickness caused by the weight of overlying sediments on a buried layer. Standard decompaction steps involve the removal of the topmost layer and allowing all the layers below to expand back to their thickness prior to the deposition of the removed layer. Porosity loss during burial depends on lithology and is assumed to follow the exponential relationship shown in Table 1 (Allen and Allen, 2006; Sclater and Christie, 1980). We use compaction parameters calculated for the Taranaki Basin from best-fit porosity-depth curves of compensated formation density-determined porosity (Table 1) (Armstrong et al., 1998). We use the flexural decompaction software 'FlexDecomp' (Badley's Geoscience Ltd) for the decompaction exercise.

$\Phi=\Phi_0 e^{-cz}$

Φ= Porosity at depth (%)

$\Phi 0$ = Porosity at the surface (%)

c= porosity-depth coefficient (km^{-1})

z= depth

The removal of sedimentary layers may result in an isostatic uplift of the basement because of mechanical unloading. However, we assume that this effect is insignificant in our study depth intervals. Therefore, we focus solely on the decompaction of the layers by keeping the basement at a fixed depth throughout the decompaction iterations.

Table 1. Parameters used for decompaction

Layer	Surface porosity Φ_0 (%)*	Porosity-depth coefficient (km^{-1})*
1	50	0.44
2	50	0.44
3	50	0.44
4	50	0.44
5	50	0.44
6	50	0.44
*Armstrong et al. (1998)		

RESULTS

The subsurface structure of the study area (Figures B-4a-c) consists of a deep (850 – 2500 TWTms) syn- back-arc extension interval where pervasive normal faulting dominates, overlain by a transition phase (500 – 850 TWT ms) and a post-extension section (<500 TWTms) that largely consists of prograding clinoform packages. We group the clinoform packages into three units, Unit-1 to -2 (transition phase) and Unit-3 (post-extension phase) and are bounded by surfaces R1 to R4 (Figures B-2b and B-4a-4c). Below, we describe the relevant features of each of these intervals.

Deep-seated dome-shaped mega-structures

Within the syn- back-arc extension section, we identify dome-shaped features in the seismic dataset (Figures B-4a and B-5a-b). The dome-shaped structures are all located in the northern domain of the seismic volume, within which one dome sits at the northernmost edge of the survey, and another to its southeast (V1 and V2 in Figure B-1b). A strong, bright, positive reflector defines the upper boundary of the dome features (R_0 reflector in Figure B-5b) which peaks at 1000 - 1250 TWTms. The largest of the two domes (V1) has a diameter of ~6.2 km, measured at the largest inflection point toward its base. Its internal character is mostly chaotic, mid-low amplitude responses that lack strong continuous reflectors, sustaining at deeper depths below the dome structure (Figure B-5b). Within the chaotic zone, we observe the presence of short high amplitude 'saucer-shaped' features and several low-amplitude reflectors that extend steeply upward into the central axis of the mound (Figure B-5b). We identify multiple cone-shaped features along the lower slopes of the mound (Figure B-5b). On the flanks of the dome structures, gently- to steeply-dipping reflectors onlap onto the strong, bright positive reflector, as well as steep normal fault segments that cut downwards into the dome structures. Above the dome-shaped features, the succeeding stratigraphic units show folding that systematically decrease (log-linear trend) in magnitude with shallowing depth from the top of the dome features (Figures B-5b and inset).

Clinoform sequence boundaries

The Korimako-1 well markers constrain surface R1 to be of Mid Pliocene age, surface R2 to be a unit at ~20 ms above the Top Pliocene, likely the base of the GFF, surface R3 to be somewhat Early-Mid Pleistocene, and surface R4 defining the top of the GFF (O'Leary et al., 2010). For

simplicity we use these four horizons (clinoform surfaces) to divide the clinothems into units U1, U2, and U3 (Figures B-2b and B-2c). Figure B-2a reveals the full extent of the GFF, initiating at the oldest shelf-edge location and a generally continuous trend in outbuilding geometry, although some interpreted faulting occurred thereafter. The vertical seismic sections, relatively closer to the modern-day continental shelf (Figures B-4b-c, see inset on 4a for location) show the variations in the thicknesses of the three depositional units bounded by the reflectors. Surfaces R1 and R2 bound the first succession, Unit 1 (U1), whilst Unit 2 (U2) is bounded by R2 and R3. As observed in the seismic section (Figure B-4c), here, surfaces R3 and R4 bound the facies along the continental shelf or topset region of the clinoform package labeled as Unit 3 (U3). The Mangaa Formation represents the bottomsets of the GFF, and as such are observed in the southern domain of the seismic section, as compared to the northern domain, where we see the upslope, foreset seismic facies. As a result, Figure B-4c shows the foresets of U1 in the northern domain, and these basinward 'bottomsets' toward the southern domain, and U2 highlights most of the foreset seismic facies of the prograding clinothems from the central to southern domain of the seismic survey. Overall, as we navigate northwest across the seismic survey, toward the basin, we will observe at best, topset, foreset and bottomset (e.g., southern domain of U1, Figure B-4a) seismic facies for each defined unit, along northern, central and southern domains of the survey.

The mapped surfaces (Figure B-4c) reveal a northward thinning of Unit 2 with an abrupt lateral increase in the angle of the R2 surface at the middle of the transect. Consequently, the thickness of Unit 1 decreases from approximately 460 TWTms in the northern domain to 174 TWTms in the central region of the study area and increases again to about 274 ms TWT in the south. There is apparently no seismic facies consistent with foreset geometries within Unit 1 toward the south. Additionally, in the north, Unit 1 consists predominantly of V and U-shaped, continuous high

amplitude reflectors that incise vertically into the underlying strata. These reflectors are "truncated" toward the south, by the surface R2. The thinner central domain of Unit 1 consists of mostly continuous subparallel, high amplitude reflectors deformed by the underlying syn-depositional sequence and faults that terminate at the surface R2. Cross-sections reveal that the increase of the angle of the lateral trend of surface R2, together with the non-uniform thickness of Unit 1, can be due to the position of the seismic inlines slicing through a zone of the continental shelf in the north and more basinal settings toward the south. However, keep in mind that the non-uniform thickness is also influenced by the aforementioned, underlying syn-depositional sequence. This is a result of the layout and alignment of the acquired seismic volume along the New Zealand coast. We therefore see more available space of the northern graben depocenter in the southern domain, which is mainly influenced by this back-arc syn-rift sequence. This sets up the observed thickness of the next prograding clinothem, Unit 2 (U2).

The northernmost section of Unit 2 is approximately 74 ms TWT and thickens to about 488 ms TWT consistently throughout the southern sections of the inline cross section (Inline 1440, Figures B-4b and B-4c). It is composed predominantly of similar V and U-shaped wavy-subparallel, mid-high amplitude reflectors, less distinct as those observed within the thicker Unit 1 facies. They are also channel type features, potentially submarine gullies or smaller submarine canyons. Toward the basin, along inline 1225 (See Figure B-4a, inset) located in the mid-sections of the 3D volume, we observe the more distal facies (lower slopes and bottomsets) of Units 1 and 2, and the foreset facies of Unit 3, dominated by mid-high amplitude, continuous wavy reflectors throughout most of the package (Figure B-4a). The high frequency and timing of these features correlate to submarine gullies studied in the region of the Taranaki Basin (Shumaker et al., 2017).

Additionally, we observe a north-dipping fault that extends from the deeper syn-rift sequences up into the shallower units (Fault D; Figure B-4a).

The geometries of the clinoform sequences

Normalization of the surfaces allowed us to observe the migration of the system by identifying the point at which there is an abrupt change in slope from the proximal basin floor to the distal foreset slope, or the toe-of-slope inflection point (See Figure B-3). We use a formula, S_c+d_{Rx} (Figures B-3b) to observe the lateral location of this inflection point. This formula represents the summation of the average distance of the eastern edge of the survey away from the western New Zealand coastline (S_c = ~38,800 meters) and the distance of the observed inflection point (i.e d_{Rx}) from the right edge of the seismic (See Figure B-3b). The angle of the maximum foreset dips (Refer to Figure B-3a) are taken along cross sections L1-L5 on the depth converted seismic volume to observe the variations in trends of dip along each clinoform surface. The spatial extent of the seismic from east to west does not allow us to measure the dip of the foreset along each surface on the seismic cross sections (eg. L1, across surface R1 – Figure B-6a). Figures B-2b and B-2c shows the limited spatial extent along surface R1 for measuring the maximum foreset dip. In addition to the inflection points measured along the surfaces, we identify from the normalized surfaces, a unique trend used to qualitatively identify the shape of the continental slope margin. This was defined by an 80% max. depth contour line. This trending line, shows the older surfaces (R1 and R2) consisting of a predominantly curvilinear geometry, exaggerated in the south, to a more rectilinear geometry in the succeeding surfaces (Figure B-7).

The graph plots for cross sections L1, L2 and L4 (Figure B-6a, B-6b and B-6d), reveal similar trends in the distance of the inflection point from the continental slope ($S_{xc}+d_R$) versus depth in

two-way-travel time. Additionally, both plots of the L3 and L5 cross sections show another distinct trending style, compared to L1, L2 and L4. We describe each of these styles as Progradation Style A and Progradation Style B, respectively. Progradation style A indicates an initial steep upward trend of the observed inflection points, before an abrupt change to a downtrend. Progradation style B also shows an initial, steep upward trend, but experiences a less abrupt, gradually increasing trend. The tightly clustered points (Figure B-6f) highlights the geometrical uniformity across the survey, following the trend of the toe-of-slope inflection point of the prograding system, on the more recent R4 surface whilst the most separated points describe the greatest geometrical non-uniformity along the older R2 surface (dashed line connecting points at R2 surface). The largest dip values are recorded in the north with maximum foreset dip angles at approximately 10° across section L1 on surface R2 (Figure B-6a) and 8° across section L2 on surface R2 as well (Figure B-6b). Along surface R3 the dip of the maximum foreset angles in the north decreases from ~7.5° (Figure B-6a) to ~6.6° (Figure B-6b), and as low as ~4.8 in the south (Figure B-6e). Along surface R4 the maximum foreset dips decreased from ~7.9 in the north (Figure B-6a) to ~6.8 (Figure B-6b), to as low as ~4.° in the south. Generally, the mid-lower slope and basinward units of the system is observed along surface R1, whilst we are able to identify more low-to-upslope environments and eventually the upslope-to-shelf edge region of the clinoforms along surface R4. This however, varies along the regionally defined domains of the survey. With the deposition of each unit, the shelf-to-basin system generally migrates to the northwest without the buried mound features influencing the input of sediment, and progradation of the clinoforms in the younger units.

Internal architecture of clinoform packages

Unit 1 (U1) drainage network patterns

Proportional slicing produces a better interpretational approach of the internal architectural elements of each chronostratigraphic clinothem, compared to time-slice intersections. The nature of the clinoforms makes it difficult to accurately identify features along the dipping surfaces on the time-slice intersections. In addition to the steepness of the shelf-edge, deep-seated mound shape features in the north have influenced the progradational evolution of this earliest succession, such that structural highs of the region have resulted in large channels that migrate toward the basin, deeply incising into the shelf-edge and along the upper slopes (Figure B-8). The northernmost dome-shaped feature has also directed sediment flow toward the southwest along the slopes of the deposited strata, indicated by the dashed arrow (See Figure B-8b). Younger stratal slices (S8) within Unit 1 (Refer to Figure B-2) potential canyon sized channels that have incised deeply (i.e. valley incisions ranging from 80-120 meters deep) into the underlying strata due to the steepening of the slopes likely influenced by differential compaction at lower sections of the U1 layer (Figure B-9a). The widths of these deeply incising channels vary between 700-1100 meters. Though we identify channel or valley-like features along the proximal shelf-to-basin region, south of the curvature attribute surface (green arrows, Figure B-9a), it does not reveal much distinct channel geometry toward the basin. This is likely due to complexity of horizon mapping or termination of the growth of channels in the zone indicated by the red arrows. Recall that due to the layout and areal limit of the seismic, specifically to the east, it is likely that these are identical to the "canyon sized" valleys we identify in the north (green arrows, Figure B-9a) that flow basinward in the central and southern regions.

Unit 1 (U1) erosional and depositional features

Unique to this older clinoform package, is the nature of the attribute response (bounded by the polygon) with lateral margins trending primarily east-west, distinctly revealed along the generated variance surface (Figure B-8c). This enclosed body consists of a mostly chaotic seismic character of high discontinuous variance zones, with globular low variance values. This mass of chaotic stratigraphic facies is also observed on the cross-section view as an interval of highly disrupted seismic facies of low-mid to mid-high acoustic impedance values (Figure B-8a) that is enclosed by a basal shear surface and topped by parallel continuous, high amplitude reflectors. The thicker and thinner portions are potentially influenced by underlying half–graben and horst-block structures. Additionally, we observe that a ENE-trending fault extends up shallow and cuts the surface (Figures B-4a and B-9a-b).

Unit 2 (U2) drainage network patterns

Channel features continue to dominate the northern most region of this unit, as the mapped stratal slices sustains a topographic high primarily in the northern domain (Figures B-10a-d). Channel width is smaller compared to the incising canyon-like valleys in the same area of the previous succession, however the central region of the attribute interpolated surfaces consists of more channels migrating as the clinoforms out-build and prograde basinward in a northwest/west direction (Figure B-10a).

Unit 2 (U2) erosional and depositional features

Keeping within the confines of the central area of the stratal slice (S5), we observe a zone of wavy-like chaotic responses in negative structural curvature, likely to be either a detached slope fan unit

or slump (Figure B-10a). This erosional feature is better revealed along the variance attribute surface (Figure B-10b). This is chronostratigraphically followed by low sinuous channels that gently meander toward the basin floor flowing through the eroded slope fan unit/slump feature along stratal slice S8 (Figure B-10c). Additionally, in the younger sequences of this unit, along stratal slice S8, RMS amplitudes reveal a high positive response within the channel geometries (Figure B-10d) and support the potential for the channels to consist of coarser grained sediment infill. Further analysis of the RMS amplitude stratal slice shows a high RMS oval-shaped feature toward the south enclosed by the black dotted line, similar to the geometry of a fan lobe deposit (See also Figure B-10d). A linear channel-like feature with mid to high-mid RMS values joins the fan lobe from along the proximal slope but is not easily distinguished within the high RMS region.

Unit 3 (U3) drainage network patterns

The lateral extent of the seismic volume has constrained the interpretations of this unit along the continental shelf-edge to the upper sections of its lower slope. Since this unit consists of distinct seismic interpreted features consistent with studies (Hansen and Kamp, 2006; Salazar et al., 2016; Shumaker et al., 2017) in the central and southern explored Taranaki Basin's Giant Foresets Formation, we are able to compare our internal architectural findings with some of the previous work done on the GFF. The early onset of this succession is characterized by a dense network of linear channels that feed into the basin (Figure B-11). Compared to the previous successions, the slopes of this unit are less steep, and there are no paleo-topographic or structural highs that allow for channels to incise deeply into underlying strata. There are also no erosional or depositional features observed along the generated stratal slice surfaces.

Stratigraphic decompaction models of the prograding units

We present the results of the sequential decompaction of the post-R4 units and Units U3 to U1 in Figures B-12a-e. In iterations #1 (removal of Post-R4 units) and #2 (removal of Post-R3 units), the syn-depositional locations of the continental slope margin are to the west of the volcano, and there are no significant changes in the unit thicknesses and maximum foreset dip angles (Figures B-12b-c). However, in iteration #3 (removal of Post-R2 units; Figure B-12d), we observe that the continental slope margin is significantly narrower, and the associated maximum foreset angle is steeper than those of Time R3 (in iteration #2) and Time R4 (in iteration #1). Further, the removal of all Post-R1 units (iteration #4; Figure B-12e) show additional change in the thicknesses of the units between the volcano and R1.

DISCUSSION

Volcanic edifices of the Miocene Mohakitino Volcanic Belt (MVB)

The tectonic setting of the study area (Figures B-1a and B-1c) and the characteristic features of the two dome-shaped structures within the syn- back-arc extension interval (Figures B-4a, B-5a-b, and B-13a-b) suggest a volcanic origin. The onlapping of the younger stratigraphic sequences, suggesting its formation at the surface and its sub-flank-parallel reflections that downlap to a basal surface are similar to some interpretations of buried volcanoes in seismic data (eg. Infante-Paez and Marfurt, 2017; Infante-Paez, 2018; Jackson et al., 2019; Magee et al., 2013; Zhao et al., 2014). The size of the dome structures (~6.2 km diameter, measured from the abrupt increase of its slope; Figure B-5a) is consistent with that of a modern volcano within the region (Mount Taranaki, ~6.5 km diameter; Figure B-4a inset). Thus, we interpret that the dome-shaped features are volcanic

seamounts, associated with the Middle to Late Miocene Mohakatino Volcanic Belt (MVB) of the Northern Taranaki Basin. The bright continuous reflector that defines the top of the volcanic edifice (R_0 reflector in Figure B-5b) is associated with the large contrast in impedance response that characterize the interface between volcanic rocks and siliciclastic sediments (e.g., Infante-Paez and Marfurt, 2017).

We interpret the low-amplitude chaotic facies bounded by the domal reflector as the magmatic conduit of the edifice (Figure B-5b). The aforementioned sub-vertical, steep reflectors that extend up through the central axis of the magma conduit are consistent with the velocity 'pull-up' (vpu) features observed in previous studies of volcanic bodies (e.g., Magee, 2013). These reflectors are useful for the estimation of seismic wave velocities through the volcanic bodies (Magee et al., 2013). It is also important to note that these features are not geologically related and can represent untrue structures in the time-migrated seismic data (Marfurt and Alves, 2015). Additionally, we deduce that the high-amplitude "saucer-shaped" reflectors beneath the R_0 reflector represents igneous sills, also consistent with the observations in previous studies (e.g., Infante-Paez and Marfurt, 2017; Magee, 2013). In our study area, the onlapping of stratigraphic reflectors on the R_0 surface (Figure B-5b) suggests that the burial of the volcanic edifice is as a result of delivery of sediments from the New Zealand hinterland, onlapping onto the volcanic seamount.

Mechanisms of deformation of the post-MVB sedimentary sequences

Although we observe that in a few places, deep-seated faults propagate up into the clinoform packages (U1; Figures B-2a, B-9a, B-9b), we primarily focus on the larger-scale influence of the buried MVB seamounts on the deformation of the clinoform packages. The deeper clinoforms and

strata that overlie the buried seamounts show doming/folding patterns that systematically decrease in magnitude with shallowing depth from the top of the seamounts (Figure B-5b and inset). This suggests that the vent of the magmatic conduit consists of a relatively more competent and denser rock, resulting in differential compaction of the overlying sediments (e.g., Reynolds et al., 2018).

Based on the observed systematic relationship between the buried seamounts and the associated overlying stratal doming, we interpret a differential compaction origin. At the time of deposition of the deeper clinoform packages, the weight of the overriding prograding sequences above the area of buried volcanoes would progressively load the underlying units, inducing a differential loading about the underlying rigid seamount. In response to the differential loading, the contrast in stiffness between the seamounts and the surrounding more-compressible sedimentary sequences would result in the differential compaction of the of the deeper units (e.g., Hansen and Cartwright, 2006), thus leading to the folding of the units. If the amplitudes of the folds are high enough (i.e. shallow burial of the mound peaks), the effect could propagate upwards and lead to the differential settling of the shallower unconsolidated sediments, thus influencing the local topography of the contemporary syn-depositional surface (Athy, 1930). In the following sections of our discussion below, we will demonstrate how the preexisting buried structures influenced the architecture of the overlying clinoform sequences by means of the mechanisms described above.

Regional evaluation of the younger clinoform sequences

Regional examination of the seismic profile provides the potential to understand how each unit varies structurally and internally with respect to the interpreted seismic facies, geometry and internal architectural elements. We have inferred that the high amplitude reflector (R2) that marks

the boundary between Unit 1 and the onset of the next clinothem succession (Unit 2) abruptly truncates the interpreted canyon sized valleys defined by the V- and U-shaped continuous reflectors (Figures B-4b-c). It is likely that this high amplitude response correlates to one of several observed condensed seismic intervals prominent within the GFF (Hansen and Kamp, 2002). Hansen and Kamp (2002, 2006) recognize these occurrences as a result of partial lithification of the horizons during relative sea level rise. There remains the potential to explore whether this is the cause for the distinct high amplitude response of surface R2 (Figure B-4c). Although the prograding units U1 and U2 develop within the transition phase, we observe the collocation of a broad 'sag' geometry along both units in the southern domain of the study area, directly above a buried half-graben (Figures B-4b-c). Additionally, we observe that thickest sections of an enclosed stratigraphic unit "MTD" within Unit U1 is collocated with underlying syn-extensional half grabens, separated by a thinner section that is collocated with an underlying syn-extensional horst block (Figure B-8a). These observations suggest the influence of differential compaction of the syn- back-arc extension sequences caused by an imposed post-extension sediment loading along the axis of the buried horst-half graben structures. Thus, we interpret that buried syn-extension horst and graben structures may control the surface topography of evolving transition phase and post-extension depositional environments. This is consistent with observations in the Northern Graben, where the spatial distribution of clinoform height within the Pliocene-Recent strata show evidence of the control of the underlying normal fault structures (Salazar, 2015).

Controls of the Mohakitino Volcanic Complex on younger clinoform sequence boundaries

The known first-order controls on clinoform architecture and progradation are accommodation space and sediment supply (e.g., Emery and Myers, 1996). In our study area, we observe

systematic relationships between the architecture of the clinoform packages and the underlying Mohakatino volcanic seamounts. First, we observe that overall, the N-S temporal variations (static) in the location of the 80% max. depth contour line along the two-way-travel time surfaces shows an initial landward migration (R1 to R2), followed by a consistently basinward migration (R2 to R4; Figures B-7a-b). However, this initial landward migration is most evident in the central and southern domains of the study area. In the northern domain, two zones of inflection are present in the deeper units (U1 and U2), one proximal and the other distal of the volcanoes (Figures B-6a and B-7a), in which the largest maximum foreset angle is collocated with the proximal inflection point (Figure B-8a). Also, the syn-depositional surface R2 in Figure B-12d shows that the narrowest continental slope margin and steepened maximum foreset angle is collocated with the zone of significant flexural decompaction response to the east of the buried volcano. These observations suggest that the differential loading of the syn-extensional sequences about the buried volcano may have induced a temporal 'pinning' of the location (slowed basinward migration), width and steep geometry of the continental slope margin at the Time R2. The collocation of the slower migrating shelf in the northern domain with the compacted eastern flank of the buried Mohakatino volcanic seamounts (Figure B-12d) suggests that the volcanic edifices may have temporally restricted the supply of sediment from the hinterlands into the basin of the northern domain. The absence of buried volcanoes in the central and southern domains may have allowed for the availability of more accommodation space further basinward, and no barrier to sediment supply. Furthermore, Progradational Style A (See Figure B-7g) correlates with the highest recorded maximum foreset dips in the northern domain, where the buried seamounts are emplaced. This tells us that the volcanic seamounts influence the apparent progradational styles observed, such that the toe of the continental slope is not laterally consistent. Progradational Style B

potentially correlates with the lower foreset dips in the central and southern domains, where the volcanic seamounts do not influence the lateral location of the toe-of-slope inflection point.

In addition, the along-trend geometry of the toe-of-slope inflection changes from a highly curvilinear/angular trend in the transition phase (R1 and R2), to a more rectilinear geometry within the post-extension interval (Unit-3 and shallower) (Figure B-7a). This is also represented by the 80%max. depth contour line. We interpret that as sediment supply into the basin progressed, the geometry of the continental slope margin eventually becomes rectilinear as the central and southern domain shelf edge catches up with the slower migrating margin in the northern domain.

The break in slope of the depositional profile occurring between the topset and the clinoform (foreset) is the offlap break (Vail et al., 1991; Emery and Myers, 1996), and is previously defined as the shelf-edge in literature (See Figure B-3). Overall, we find a prominence of stacked offlap breaks and over-steepened (7-10°) clinoform foreset slopes within the northern domain (Refer to Figure B-13a) transition phase clinoforms, and occurrence of gently dipping foreset slopes (<6°) in the southern domain (Refer to Figure B-13c). Whereas, the post-extension clinoforms exhibit very low (<5°) and intermediate (5-7°) foreset slopes across the entire survey. Also, we observe that post-R2 loading of the area by the prograding sequences also induced more, although minor differential compaction of the deeper units (Figures B-12b-c). This led to an additional flexure of the compacted units created the highly flexed geometry of the deeper units (units between the volcano and R1) seen in present-day (Figure B-12a). Therefore, we further infer that the influence of the buried volcanoes on the post-extension sequences are not only syn-depositional, but also post-deposition of the clinoform packages. The observed temporal variations of the geometry of the post-extension sequences (units above the volcano) between the northern and southern domains

of the study area suggest a systematic control of the buried volcanic structures in the northern domain.

We infer that the delivery of sediment along the oversteepened slopes within the deeper units (U1 up to Time R2) incised into the underlying stratigraphy forming canyon sized valleys (Figures B-9a-b), that can be characterized as potential submarine canyons based on interpretations by Talling (1998). Their analyses characterize submarine canyon incisions to have depths greater than 70 m, coinciding with erosional processes, likely via turbidity currents. Additionally, Talling (1998) mention that pre-existing submarine canyons that are sub-aerially expose during sea level fall, tend to extend across the shelf-edge toward the continental coast. The seismic attribute stratal slices do not distinctly reveal extension of the canyon incision along the shelf edge (See Figure B-9a). As the foreset angle becomes too steep, rapid deposition at the sudden decrease in slope occurs as turbidity currents will bypass the foreset - and with each succeeding flow of sediment packages and deposition on top of previously deposited material downslope, result in the backstepping of sediment (Refer to Figures B-13d-h) onto the foreset, similar to observations defined by Gerber (2008). Such processes also indicate a period of high sediment supply. This may seem contradicting, since short-lived ovsersteeping of clinoform foresets have been linked to low rates of sediment supply into the basin (O'Grady et al., 2000; Shumaker et al., 2017) and/or the delivery of coarser grained sediment (Orton and Reading, 1993). O'Grady (2000) defines similar regional continental slope-geometries as "deep and steep" margins with dips ranging between 5-9.5°, consistent with high rates of canyon incision and mass wasting processes. The decrease in our measured foreset slope angles toward the southern domain, and following the position of the volcanic edifice, ranging between 4.3 - 6.5°, coincides with O'Grady's (2000) interpretation of relatively low sediment input of "steep and rough" margins (4.4 – 6.5° slope angles) and higher

sediment supply of "sigmoid" margins (2.2 – 4.5). This further stipulates the contribution of the placement of the volcanic seamount as a potential area of lateral confinement, influencing the geometry of the foreset slope and/or the migration of the progradational system.

Hansen and Kamp (2006) recognize that the northern "graben-bounding" faults have undergone displacement from the Pliocene into Pleistocene, controlling the patterns of deposition, regarding size and distribution in regional strata of the Giant Forests Formation. We suggest that the GFF, inferred from well summary reports, thickens toward the south where larger accommodation space is provided by southern extension of the graben, and its syn-depositional normal faults acting as the main depocentre for sediment deposition (Bierbrauer et al., 2008; Kamp and Furlong, 2006). The successions are structurally influenced by the paleo-topographic highs of the volcanic massifs closer to the continental shelf and deposition into the northern graben, while building and prograding northwestward/westward onto the Western Stable Platform. It is assumed that in the southernmost domain of the 3-D seismic, the perceived northwestern migration of the slope margin is consistent with the overall NW migration of the studied Giant Foresets formation, observed in previous studies (Salazar et al., 2016; Shumaker et al., 2017). On the contrary, the shelf-edge maintains a general westerly migration pattern as the Northern Graben depocentre opens up in the same direction but with axial movement likely limited by the basement high of the Western Stable Platform.

Associated architectural elements of the younger clinoforms

The stratigraphically-enclosed body ("MTD" in Figure B-8c) consisting of a mostly chaotic seismic character of high discontinuous variance zones, with globular low variance values is

identified as coherent displaced rock consistent with mass transport deposits (MTDs), a common component of deep-water settings. The occurrence of the MTD (Figures B-8a-c) above reflector R1 (within Unit 1) during Mid Pliocene is imaged clearly by the variance attribute as a result of the significant variations and structural discontinuity in its seismic trace patterns. They are consistent with great degrees of slope failure triggered by regression during rapid sea level fall, high sedimentation rates, seismicity and gas hydrate destabilization (Moscardelli and Wood, 2008; Rusconi, 2017). Rusconi (2017) studied MTD's in the Taranaki Basin within the Pliocene to Pleistocene interval, linking their occurrence to oversteepening of the slopes due to high sediment influx to the shelf edge and seismicity related to back arc extension. It is therefore possible that this erosional feature located below surface R2, and which truncates parallel amplitude reflectors (See Figure B-8a) on both sides in the central region of the volume, likely occurred during the basinward outbuilding of Unit 1, since it coincides with the back arc extension tectonics. Internal clinoform architectural elements are more prominent within Unit 2 as more channelized geometries are also highlighted along the curvature attribute surfaces (Figures B-10a and B-10c). Here, we interpret a slump feature, which (Refer to Figure B-10a and B-10b) associated with periods of falling sea level, in which unstable slope conditions persist due to over-pressuring (Postma, 1984) during sediment accumulation, and a depositional fan lobe toward the south, coherent with mud/sand rich systems distinctly encapsulated by the high positive RMS amplitude response. We've linked, via interpretations by Bierbrauer (2008), the top of Unit 2 to the end of a falling stage systems tract, before the initiation of a high-stand systems tract. The basin was perhaps experiencing increasing sediment bypass forming the aforementioned principal elements of deep-marine clastic systems. The system then experienced an increase in sediment supply with steady rise in sea level, as the sequence boundary at the base of our interpreted Unit 3 (top Unit 2),

coincides with the high-stand systems tract interpreted by Bierbrauer (2008). The timing of this increasing sediment supply, and overall decreasing maximum foreset angles, can be further be supported by the increase in uplift of the Southern Alps ~3 Myr ago in Late Pliocene, supplying sediment across the Taranaki Basin (Tippet and Kamp, 1995; Salazar et al., 2015)

Unit 3 consists of shallower foreset and topset gradients as further supported by the mapped negative curvature stratal slices (Figure B-11), indicating the overall transition to a sediment driven arrangement as the progradation system migrated toward and onto the Western Stable Platform (Shumaker et al., 2017). The more recent sequence of this unit is characterized by a dense network of linear channels that feed into the basin (Figure B-11). These regularly spaced channels have been defined as submarine gullies, originating at the shelf-edge (Shumaker et al., 2016). The shelf edge has migrated significantly basinward (S2 and S8), and the network of the gullies are predominant throughout the northern to southernmost domains of the horizon surface. The RMS amplitude also reveal high positive responses within the confines of the northern and southern highlighted gullies (Figure B-11b), again discriminating the lithological variations across the surface. The Giant Foresets Formation is a claystone to siltstone dominated succession comprising of intervals of argillaceous sandstone (O'Leary et al., 2010) and is generally a thick coarsening upward sequence commencing in late Miocene further south near the Awatea-1 well (Hansen and Kamp, 2006; O'Leary et al., 2010) and commencing in early Pliocene in our area of study. With the interpretations of Bierbrauer (2008), and our observations, we assume that this coarsening upward sequence explains the increase in channelization or gully formation coinciding with a high energy transport environment and increased erosion and deposition as the gullies partially incise into the paleo-seafloor.

Implications for the influence of preexisting structures on the architecture of deep-water progradational sequences

Few studies have highlighted the potential influence of buried structural features on subsequent sedimentary sequences (Hardage et al., 1996; Tsikalas, et al., 1998; Anka et al., 2009; Alves, 2010; Johnston et al., 2010). Our observations in the Northern Taranaki Basin expand on these previous works by demonstrating that buried, discrete, massive, relatively more- or less-stiff structures may significantly modulate the geometry of syn-depositional surfaces and the post-depositional architecture of deep-water progradational sequences. These features may include, but are not limited to paleovolcanoes, mass transport deposits, impact craters, carbonate mounds & karst features, horst-graben structures etc.

Furthermore, our findings highlight important controls on post-extensional sedimentation patterns in magmatic continental margins that contrast those of non-magmatic margins. For example, in the case of rifted margins, the global distribution of magmatic and non-magmatic rifted margins (e.g., Geoffroy, 2005; Leroy at al., 2008) suggests that there is a significant percentage of magmatic rifted margins. Magmatic rifted margins account for approximately 80% of the total distribution, with 20% being the known non-magmatic or magma-poor regions. The Northern Taranaki Basin is located within a back-arc setting of a previously rifted margin, and therefore is not a true passive margin in its present form. However, the structures potentially present features that may be observable in rifted margins that have accommodated magmatic deformation. In the central domain of our study area where buried volcanoes are absent, we observe the differential compaction of the syn- and post-extension sedimentary packages influenced by buried horst-graben structures. This indicates that the buried syn-extensional horst-graben structures may partially control the topography of the succeeding depositional environment (e.g., Figures B-8a,

B-4c, and B-14). The modulation of the topography would have a spatial wavelength that is consistent with the extents and geometry of the buried structure (e.g., Figure B-8a). We envision that such controls on post-extension sedimentary architecture may be observable in both magmatic and non-magmatic rifted regions. However, the presence of paleovolcanoes in the deeper strata of rifted margins having magmatic deformation constitute relatively 'smaller' (shorter-wavelength) structures that are super-imposed on the longer-wavelength syn-extension horst-graben structures (Figure B-14). We infer that the superposition of buried syn-extension volcanoes on their contemporary longer-wavelength horst-graben structures in magmatic rifted margins represents an important distinction on the controls of post-extension progradational sedimentation patterns that contrasts those of rifted margins that have not accommodated magmatic deformation (Figure B-14). Overall, in relation to both divergent and convergent continental margins, we have shown that the architecture and sedimentation patterns reveal a relationship between buried volcanic structures and succeeding post-magmatism progradational stratigraphic successions, such that we observe high maximum foreset angles; relative temporal pinning of the continental slope; and a transition from accommodated erosional features such as submarine canyon incision, mass transport deposits, and slumps to less erosional and more depositional channelized features (submarine gullies) as the system progrades.

CONCLUSIONS

We investigated the controls of buried syn-back-arc extension seamounts on the post-extension sedimentation patterns within the Northern Taranaki Basin. Our results reveal that overall, the N-S trend of continental slope margin changes from a highly curvilinear geometry in the deeper post-extension sequences (transition phase), into a rectilinear trend within the shallower post-extension

sequences. In the northern domain of the study area where the buried seamounts dominate, the overlying clinoform packages and sequence boundaries show folding that systematically decrease in magnitude with shallowing depth from the top of the underlying seamounts. In this same part of the area, we observe aggradational type seismic facies, clinoform oversteepening and backstepping, high foreset slope angles, and relatively slower continental slope margin basinward migration (temporally 'pinned') in the post- extension sequences above the buried volcanoes.

Whereas, in the southern domain, where buried volcanoes are absent, we observe more progradational type seismic facies, very low foreset slope angles, and landward-to-basinward ('unpinned') migration of the continental slope margin. Additionally, in the northern domain, we observe wide, closely spaced channel incision into over-steepened slope dominate the post-extension sequence in the northern domain. Whereas, narrower, straighter channels dominate the southern domain. These findings suggest that buried syn-extension volcanic massifs can significantly influence the architecture of the succeeding progradational sedimentary successions. Our study provides insight into the controls of preexisting buried discrete, massive, relatively more- or less-stiff structures on the development of the onset of deep-water progradational sequences, such that we observe high maximum foreset angles; relative temporal pinning of the continental slope; and a transition from accommodated erosional features such as submarine canyon incision, mass transport deposits, and slumps to less erosional and more depositional channelized features (submarine gullies) as the system progrades. Furthermore, we suggest that our findings in this work present a distinction in the controls on sedimentation patterns between magmatic and non-magmatic continental margins.

ACKOWLEDGEMENTS

We would sincerely like to thank New Zealand Petroleum & Minerals and Origin Energy New Zealand Pty Ltd for providing the Nimitz 3D data set. Additionally, we express our greatest appreciation to Petrel E&P software from Schlumberger for providing the University of Oklahoma with the academic licenses for conducting this project as well as the AASPI (Attribute-Assisted Seismic Processing and Interpretation) consortium here at the University of Oklahoma. We thank CGG for providing the Hampson Russell academic license used for this study and Badley's Geoscience Ltd for providing the FlexDecomp software. We thank Abidin Caf for assisting within the seismic-to-well tie. We also thank the Editor Craig Magee, reviewer Mac Beggs and the second, anonymous, reviewer.

Data Availability Statement: The data that support the findings of this study are publicly available on the New Zealand Petroleum and Minerals website www.nzpam.govt.nz, and can be acquired without any privacy or ethical restrictions.

REFERENCES

Allen, P., and Allen, J. R. (2006). Basin analysis. Principles and applications 2nd edn, Blackwell Scientific Publications. Oxford, p. 549p.

Alves, T. M. (2010). 3D Seismic examples of differential compaction in mass-transport deposits and their effect on post-failure strata. Marine Geology, 271(3–4), 212–224. https://doi.org/10.1016/j.margeo.2010.02.014

Amonpantang, P., Bedle, H., & Wu, J. (2019). Multiattribute analysis for channel element discrimination in the Taranaki Basin, offshore New Zealand. Interpretation, 7(2), SC45–SC61. https://doi.org/10.1190/INT-2018-0174.1

Anell, I., & Midtkandal, I. (2017). The quantifiable clinothem—Types, shapes and geometric relationships in the Plio-Pleistocene Giant Foresets Formation, Taranaki Basin, New Zealand. Basin Research, 29, 277–297. https://doi.org/10.1111/bre.12149

Anka, Z., Séranne, M., Lopez, M., Scheck-Wenderoth, M., & Savoye, B. (2009). The long-term evolution of the Congo deep-sea fan: A basin-wide view of the interaction between a giant submarine fan and a mature passive margin (ZaiAngo project). Tectonophysics, 470(1–2), 42–56. https://doi.org/10.1016/j.tecto.2008.04.009.

Armstrong, P. A., Allis, R. G., Funnell, R. H., and Chapman, D. S. (1998). Late Neogene exhumation patterns in Taranaki Basin (New Zealand): Evidence from offset porosity-depth trends: Journal of Geophysical Research: Solid Earth, v. 103, no. B12, p. 30269-30282.

Athy, L.F. (1930). Density, porosity, and compaction of sedimentary rocks. Aapg Bulletin, 14(1), pp.1-24.

Berton, F., Vesely, F. F., & Universidade Federal do Paraná, Brazil. (2016). Seismic expression of depositional elements associated with a strongly progradational shelf margin: Northern Santos Basin, southeastern Brazil. Brazilian Journal of Geology, 46(4), 585–603. https://doi.org/10.1590/2317-4889201620160031

Bierbrauer, K., Herdy, T.J., Rek, A. & Mills K.L. (2008). Offshore Northland Basin - Frontier exploration north of the established Taranaki Hydrocarbon Province. Origin Energy Limited, 18.

Bischoff, A. P., Nicol, A., & Beggs, M. (2017). Stratigraphy of architectural elements in a buried volcanic system and implications for hydrocarbon exploration. Interpretation, 5(3), SK141–SK159. https://doi.org/10.1190/INT-2016-0201.1

Bridgwater, D., Sutton, J. and Watterson, J. (1974). Crustal downfolding associated with igneous activity. Tectonophysics, 21(1-2), pp.57-77.

Chen, Q., & Sidney, S. (1997). Seismic attribute technology for reservoir forecasting and monitoring. The Leading Edge, 16(5), 445–448. https://doi.org/10.1190/1.1437657

Chopra, S., & Marfurt, K. J. (2008). Emerging and future trends in seismic attributes. The Leading Edge, 27(3), 298–318. https://doi.org/10.1190/1.2896620.

Chopra, S., Marfurt, K. (2013). Structural curvature versus amplitude curvature. The Leading Edge. Pgs 178-184.

Emery, D. and Myers, K.J. (1996). Sequence Stratigraphy. Blackwell Science, Oxford, 297. http://dx.doi.org/10.1002/9781444313710

Feuillet, N., Manighetti, I., Tapponnier, P. and Jacques, E. (2002). Arc parallel extension and localization of volcanic complexes in Guadeloupe, Lesser Antilles. Journal of Geophysical Research: Solid Earth, 107(B12), pp.ETG-3.

Gerber, T. P., Pratson, L. F., Wolinsky, M. A., Steel, R., Mohr, J., Swenson, J. B., Paola, C. (2008). Clinoform Progradation by Turbisity Currents: Modeling and Experiments. Journal of Sedimentary Research; 78 (3), 220-238. https://doi.org/10.2110/jsr.2008.023

Geoffroy, L. (2005). Volcanic passive margins. Comptes Rendus Geoscience, 337(16), 1395–1408. https://doi.org/10.1016/j.crte.2005.10.006

Giba, M., Nicol, A., & Walsh, J. J. (2010). Evolution of faulting and volcanism in a back-arc basin and its implications for subduction processes: Taranaki Basin Evolution. Tectonics, 29(4), n/a-n/a. https://doi.org/10.1029/2009TC002634

Giba, M., Walsh, J. J., Nicol, A., Mouslopoulou, V., & Seebeck, H. (2013). Investigation of the spatio-temporal relationship between normal faulting and arc volcanism on million-year time scales. Journal of the Geological Society, 170(6), 951–962. https://doi.org/10.1144/jgs2012-121

Gomes, M. P., Vital, H., Bezerra, F. H. R., de Castro, D. L., & Macedo, J. W. de P. (2014). The interplay between structural inheritance and morphology in the Equatorial Continental Shelf of Brazil. Marine Geology, 355, 150–161. https://doi.org/10.1016/j.margeo.2014.06.002

Gomis-Cartesio, L. E., Poyatos-Moré, M., Hodgson, D. M., & Flint, S. S. (2018). Shelf-margin clinothem progradation, degradation and readjustment: Tanqua depocentre, Karoo Basin (South Africa). Sedimentology, 65(3), 809–841. https://doi.org/10.1111/sed.12406

Gong, C., Wang, Y., Zhu, W., Li, W., Xu, Q., & Zhang, J. (2011). The Central Submarine Canyon in the Qiongdongnan Basin, northwestern South China Sea: Architecture, sequence stratigraphy, and depositional processes. Marine and Petroleum Geology, 28(9), 1690–1702. https://doi.org/10.1016/j.marpetgeo.2011.06.005

Hansen, R. J., & Kamp, P. J. (2002). Evolution of the Giant Foresets Formation, northern Taranaki Basin, New Zealand. 18.

Hansen, R. J., & Kamp, P. J. J. (2004a). Late Miocene to early Pliocene stratigraphic record in northern Taranaki Basin: Condensed sedimentation ahead of Northern Graben extension and progradation of the modern continental margin. New Zealand Journal of Geology and Geophysics, 47(4), 645–662. https://doi.org/10.1080/00288306.2004.9515081

Hansen, R., & Kamp, P. (2004b). Rapid progradation of the Pliocene-Pleistocene continental margin, northern Taranaki Basin, New Zealand, and implications. 10.

Hansen, D.M. and Cartwright, J.A. (2006). The three-dimensional geometry and growth of forced folds above saucer-shaped igneous sills. Journal of Structural Geology, 28(8), pp.1520-1535.

Hansen, R. J., & Kamp, P. J. J. (2006). Sequence stratigraphy and architectural elements of the Giant Foresets Formation, northern Taranaki Basin, New Zealand. 13.

Hardage, B. A., Carr, D. L., Lancaster, D. E., Simmons, J. L., Elphick, R. Y., Pendleton, V. M., & Johns, R. A. (1996). 3-D seismic evidence of the effects of carbonate karst collapse on overlying clastic stratigraphy and reservoir compartmentalization. GEOPHYSICS, 61(5), 1336–1350. https://doi.org/10.1190/1.1444057

Heezen, B. C., Hollister, C. D., & Ruddiman, W. F. (1966). Shaping of the Continental Rise by Deep Geostrophic Contour Currents. Science, 152(3721), 502–508. https://doi.org/10.1126/science.152.3721.502

Herzer, R. H. (1995). Seismic stratigraphy of a buried volcanic arc, Northland, New Zealand and implications for Neogene subduction. Marine and Petroleum Geology, 12, 511–531.

Holford, S., Schofield, N., MacDonald, J., Duddy, I. and Green, P. (2012). Seismic analysis of igneous systems in sedimentary basins and their impacts on hydrocarbon prospectivity: Examples from the southern Australian margin. The APPEA Journal, 52(1), pp.229-252.

Hood, S. D., Nelson, C. S., & Kamp, P. J. J. (2003). Lithostratigraphy and depositional episodes of the Oligocene carbonate-rich Tikorangi Formation, Taranaki Basin, New Zealand. New Zealand Journal of Geology and Geophysics, 46(3), 363–386. https://doi.org/10.1080/00288306.2003.9515015

Infante-Paez, L., & Marfurt, K. J. (2017). Seismic expression and geomorphology of igneous bodies: A Taranaki Basin, New Zealand, case study. Interpretation, 5, SK121-SK140.

Infante-Paez, L. (2018). Seismic expression of igneous bodies in sedimentary basins and their impact on hydrocarbon exploration: Examples from a compressive tectonic setting, Taranaki Basin, New Zealand. PhD. Dissertation, University of Oklahoma.

Jackson, C.A., Schofield, N. and Golenkov, B. (2013). Geometry and controls on the development of igneous sill–related forced folds: A 2-D seismic reflection case study from offshore southern Australia. Bulletin, 125(11-12), pp.1874-1890.

Jackson, C.A., Magee, C. and Hunt-Stewart, E.R. (2019). Cenozoic contourites in the eastern Great Australian Bight, offshore southern Australia: implications for the onset of the Leeuwin Current. Journal of Sedimentary Research, 89(3), pp.199-206.

Johnston, S., Strachan, L., Cassidy, J. (n.d.). Late Pliocene to Recent Seismic Stratigraphy of the Northland Basin, New Zealand, #50327 (2010). 33.

Kamp, P.J.J. (1984). Neogene and Quaternary extent and geometry of the subducted Pacific Plate beneath North Island, New Zealand: Implications for Kaikoura tectonics. Tectonophysics, 108, 241–266.

Kamp, P. J. J., & Furlong, K. P. (2006). Neogene Plate Tectonic Reconstructions and Geodynamics of North Island Sedimentary Basins: Implications for the Petroleum Systems. 14.

King, P.R. and Thrasher, G.P. (1996) Cretaceous-Cenozoic geology and petroleum systems of the Taranaki Basin, New Zealand. Institute of Geological and Nuclear Sciences monograph 13. 243 p. 6 enclosures. Institute of Geological and Nuclear Scienses Ltd., Lower Hutt.

King, P. R., 2000, Tectonic reconstructions of New Zealand: 40 Ma to the present: New

Zealand Journal of Geology and Geophysics, 43, 611–638.

Kolawole, F., Simpson-Turko M., & Carpenter, B. M. (2020). Basement-Controlled Deformation of Sedimentary Sequences, Anadarko Shelf, Oklahoma. Basin Research.

Leroy, M., Gueydan, F., & Dauteuil, O. (2008). Uplift and strength evolution of passive margins inferred from 2-D conductive modelling. Geophysical Journal International, 172(1), 464–476. https://doi.org/10.1111/j.1365-246X.2007.03566.x

Lodwick, George, Rupert, Maguire (2019). What controls the reservoir quality of andesitic arc derived volcano clastic sandstone reservoirs: An example from the Mohakatino Formation, Taranaki Basin, New Zealand, Durham theses, Durham University. Available at Durham E-Theses Online:http://etheses.dur.ac.uk/13239/

Magee, C., Hunt-Stewart, E., & Jackson, C. A.-L. (2013). Volcano growth mechanisms and the role of sub-volcanic intrusions: Insights from 2D seismic reflection data. Earth and Planetary Science Letters, 373, 41–53. https://doi.org/10.1016/j.epsl.2013.04.041

Magee, C., Muirhead, J.D., Karvelas, A., Holford, S.P., Jackson, C.A., Bastow, I.D., Schofield, N., Stevenson, C.T., McLean, C., McCarthy, W. and Shtukert, O. (2016). Lateral magma flow in mafic sill complexes. Geosphere, 12(3), pp.809-841.

Magee, C., Stevenson, C. T. E., Ebmeier, S. K., Keir, D., Hammond, J. O. S., Gottsmann, J. H., Whaler, K. A., Schofield, N., Jackson, C. A.-L., Petronis, M. S., O'Driscoll, B., Morgan, J., Cruden, A., Vollgger, S. A., Dering, G., Micklethwaite, S., & Jackson, M. D. (2018). Magma Plumbing Systems: A Geophysical Perspective. Journal of Petrology, 59(6), 1217–1251. https://doi.org/10.1093/petrology/egy064

Marfurt, K. J., & Alves, T. M. (2015). Pitfalls and limitations in seismic attribute interpretation of tectonic features. Interpretation, 3(1), SB5–SB15. https://doi.org/10.1190/INT-2014-0122.1

Mitchum, R. M. (1977). Seismic Stratigraphy and Global Changes of Sea Level, Part 11: Glossary of Terms used in Seismic Stratigraphy. 8.

Mortimer, E.J., Paton, D.A., Scholz, C.A. and Strecker, M.R. (2016). Implications of structural inheritance in oblique rift zones for basin compartmentalization: Nkhata Basin, Malawi Rift (EARS). Marine and Petroleum Geology, 72, pp.110-121.

Moscardelli, L., & Wood, L. (2008). New classification system for mass transport complexes in offshore Trinidad. Basin Research, 20(1), 73–98. https://doi.org/10.1111/j.1365-2117.2007.00340.x

Muirhead, J.D., Airoldi, G., Rowland, J.V. and White, J.D. (2012). Interconnected sills and inclined sheet intrusions control shallow magma transport in the Ferrar large igneous province, Antarctica. Bulletin, 124(1-2), pp.162-180.

Murdmaa, I. O., Levchenko, O. V., & Marinova, J. G. (2012). Quaternary seismic facies of the atlantic continental rise. Lithology and Mineral Resources, 47(5), 379–400. https://doi.org/10.1134/S0024490212050069

Nicol, A., Mazengarb, C., Chanier, F., Rait, G., Uruski, C., & Wallace, L. (2007). Tectonic evolution of the active Hikurangi subduction margin, New Zealand, since the Oligocene:

Hikurangi Subduction Margin Tectonics. Tectonics, 26(4), n/a-n/a. https://doi.org/10.1029/2006TC002090

O'Grady, D. B., Syvitski, J. P. M., Pratson, L. F., & Sarg, J. F. (2000). Categorizing the morphologic variability of siliciclastic passive continental margins. 4.

O'Grady, D. B., & Syvitski, J. P. M. (2002). Large-scale morphology of Arctic continental slopes: The influence of sediment delivery on slope form. Geological Society, London, Special Publications, 203(1), 11–31. https://doi.org/10.1144/GSL.SP.2002.203.01.02

O'Leary, R. Luft, F. and Mogg, W. Origin Energy New Zealand Pty Ltd (2010). Ministry of Economic Development New Zealand Unpublished Petroleum Report 4299. 401

Orton, G. J., & Reading, H. G. (1993). Variability of deltaic processes in terms of sediment supply, with particular emphasis on grain size. Sedimentology, 40(3), 475–512. https://doi.org/10.1111/j.1365-3091.1993.tb01347.x

Palmer, J. (1985). Pre-Miocene lithostratigraphy of Taranaki Basin, New Zealand. New Zealand journal of geology and geophysics, 28, 197-216.

Patruno, S., & Helland-Hansen, W. (2018). Clinoforms and clinoform systems: Review and dynamic classification scheme for shorelines, subaqueous deltas, shelf edges and continental margins. Earth-Science Reviews, 185, 202–233. https://doi.org/10.1016/j.earscirev.2018.05.016

Postma, G. (1984). Slumps and their deposits in fan delta front and slope. 4

Puga-Bernabéu, Á., Vonk, A. J., Nelson, C. S., & Kamp, P. J. J. (2009). Mangarara Formation: Exhumed remnants of a middle Miocene, temperate carbonate, submarine channel-fan system on the eastern margin of Taranaki Basin, New Zealand. New Zealand Journal of Geology and Geophysics, 52(2), 73–93. https://doi.org/10.1080/00288300909509880

Randen, T., Pedersen, S. I., & Sønneland, L. (2001). Automatic extraction of fault surfaces from three-dimensional seismic data. SEG Technical Program Expanded Abstracts 2001, 551–554. https://doi.org/10.1190/1.1816675

Reynolds, P., Schofield, N., Brown, R. J., & Holford, S. P. (2018). The architecture of submarine monogenetic volcanoes—Insights from 3D seismic data. Basin Research, 30, 437–451. https://doi.org/10.1111/bre.12230

Rusconi, F. J. (n.d.). 3D Seismic Interpretation of a Plio-Pleistocene Mass Transport Deposit in the Deepwater Taranaki Basin of New Zealand. (2017). 62.

Salazar, M., Moscardelli, L., & Wood, L. (2016). Utilising clinoform architecture to understand the drivers of basin margin evolution: A case study in the Taranaki Basin, New Zealand. Basin Research, 28(6), 840–865. https://doi.org/10.1111/bre.12138

Sclater, J. G., and Christie, P. A. (1980). Continental stretching: An explanation of the post-mid-Cretaceous subsidence of the central North Sea basin: Journal of Geophysical Research: Solid Earth, v. 85, no. B7, p. 3711-3739.

Seebeck, H.C. (2012). Normal Faulting, Volcanic and Fluid Flow, Hikurangi Subduction Plate Boundary, New Zealand. PhD. Dissertation, University of Canterbury. 113-151

Seebeck, H., Nicol, A., Villamor, P., Ristau, J., & Pettinga, J. (2014). Structure and kinematics of the Taupo Rift, New Zealand: Taupo Rift. Tectonics, 33(6), 1178–1199. https://doi.org/10.1002/2014TC003569.

Shumaker, L. E., Jobe, Z. R., & Graham, S. A. (2017). Evolution of submarine gullies on a prograding slope: Insights from 3D seismic reflection data. Marine Geology, 393, 35–46. https://doi.org/10.1016/j.margeo.2016.06.006

Slingerland, R., Driscoll, N. W., Milliman, J. D., Miller, S. R., & Johnstone, E. A. (2008). Anatomy and growth of a Holocene clinothem in the Gulf of Papua. Journal of Geophysical Research, 113(F1), F01S13. https://doi.org/10.1029/2006JF000628

Stagpoole, V., & Funnell, R. (2001). Arc magmatism and hydrocarbon generation in the northern Taranaki Basin, New Zealand. Petroleum Geoscience, 7(3), 255–267. https://doi.org/10.1144/petgeo.7.3.255.

Stagpoole, V., & Nicol, A. (2008). Regional structure and kinematic history of a large subduction back thrust: Taranaki Fault, New Zealand. Journal of Geophysical Research, 113(B1), B01403. https://doi.org/10.1029/2007JB005170.

Steel R.J & Olsen T. (2002). Clinoforms, clinoform trajectories and deepwater sands. In: Armentrout J.M. & Rosoen N.C. (Eds.). Sequence stratigraphic models fpr exploration and production: evolving models and appkication histories, GCS-SEPM Special Publication, 22: 367-381.

Talling, P. J. (1998). How and where do incised valleys form if sea level remains above the shelf edge? 4.

Tippett, J. M., & Kamp, P. J. J. (1995). Geomorphic evolution of the Southern Alps, New Zealand. Earth Surface Processes and Landforms, 20(2), 177–192. https://doi.org/10.1002/esp.3290200207

Tsikalas, F., Gudlaugsson, S. T., & Faleide, J. I. (1998). The anatomy of a buried complex impact structure: The Mjølnir Structure, Barents Sea. Journal of Geophysical Research: Solid Earth, 103(B12), 30469–30483. https://doi.org/10.1029/97JB03389

Unkaracalar, E. E. 3D seismic imaging of submarine stratovolcanic and salt structures beneath the Taranaki Basin, New Zealand and the Gulf of Mexico (2018). Masters Theses. 7787. http://scholarsmine.mst.edu/masters_theses/7787

Uruski, C., & Baillie, P. (2004). Mesozoic evolution of the Greater Taranaki Basin and implications for petroleum prospectivity. The Appea Journal, 44(1), 385. https://doi.org/10.1071/AJ03014

Vail, PR. (1987). Seismic stratigraphy interpretation using sequence stratigraphy. Part I: Seismic stratigraphy interpretation procedure. In Atlas of Seismic Stratigraphy, ed. AW Bally, pp. 1-10. Am. Assoc. Petrol. Geol. Stud. Geol. No. 27, Vol. 1. 125 pp

Vail, P.R., Audemart, F., Bowman, S.A., Eisner, P.N, Perez-Cruz, G. (1991). The stratigraphic signatures of tectonics, eustasy and sedimentation – an overview. In: cyclic Stratigraphy (ed. By G.Einsele, W. Ricken & Seilacher). Springer-Verlag, New York, pp. 617-659.

Zhao, F., Wu, S., Sun, Q., Huuse, M., Li, W., & Wang, Z. (2014). Submarine volcanic mounds in the Pearl River Mouth Basin, northern South China Sea. Marine Geology, 355, 162–172. https://doi.org/10.1016/j.margeo.2014.05.018.

FIGURES

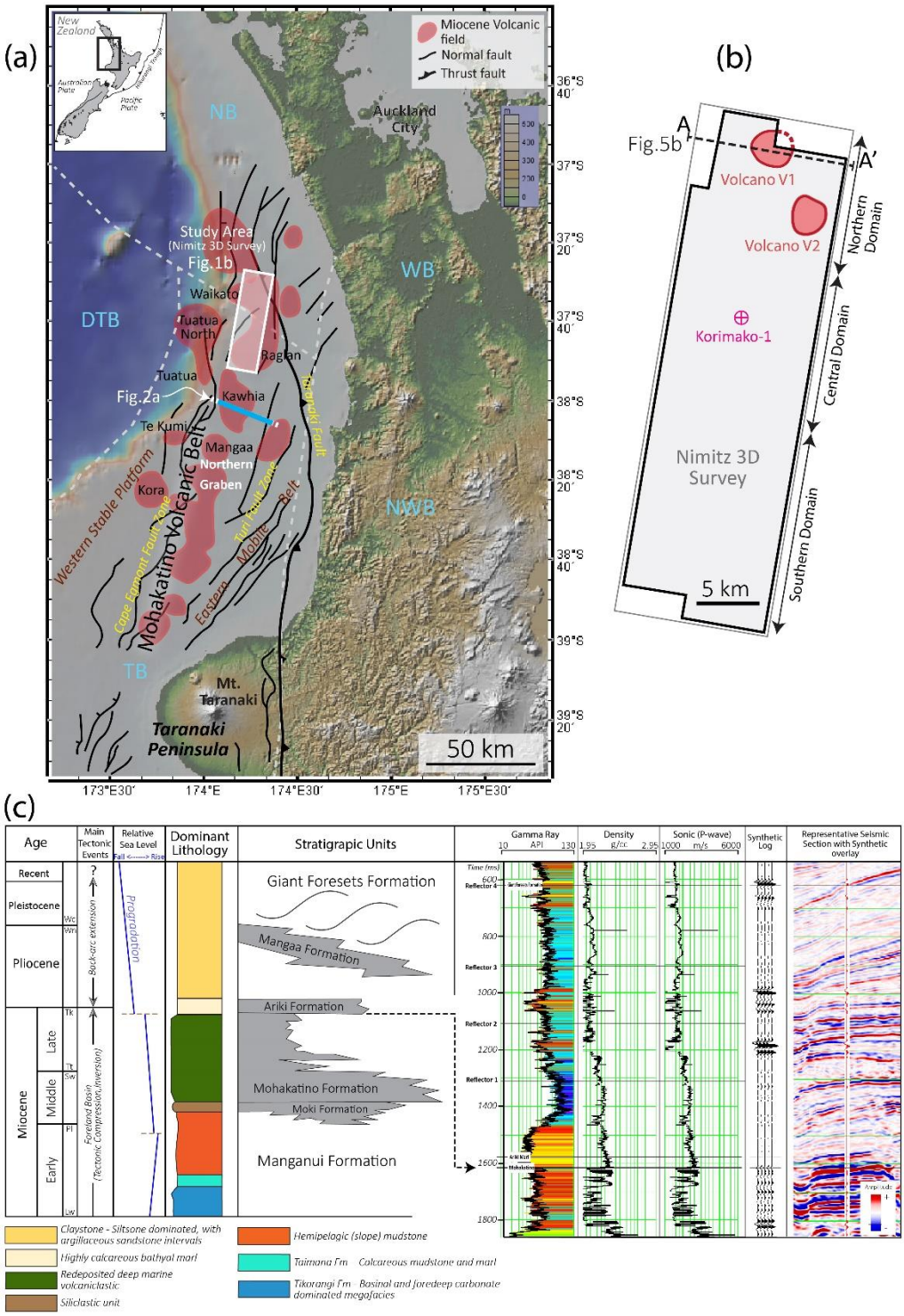

Figure B-1. Location and the geologic setting of the study area. (a) Topographic map of northern New Zealand showing the Taranaki and Northland Basins, large faults, and the Miocene volcanic fields of the Mohakatino Volcanic Belt (modified after Stagpoole & Funnell, 2001 and Johnston et al., 2010). The location of the primary study area (Nimitz 3-D Seismic Survey) is

shown in the white rectangle, together with a 2D transect line used to show the extent of interpreted geologic features, discussed throughout this expert. (b) Map of the Nimitz 3-D seismic survey and location of the Korimako-1 well. (c) Generalized stratigraphic column of the upper fill of the Taranaki Basin (after Unkaracalar, 2018 and King and Thrasher, 1996), and generated wireline logs and synthetic model of the Korimako-1 well. The following stage abbreviations reflect the local geology of the area; Wc-Castlecliffian, Wn-Nukumaruan, Wo-Opoitian, Tk-Kapitean, Tt-Tongaporutuan, Sw-Waiauan, Sc-Clifdenian, Pl-Altonian, Lw-Waitakian). Predominant Formation lithologies are classified based on observations by Hood (2003), Puga-Bernabéu (2009) and O'Leary (2010). DTB – Deepwater Taranaki Basin, NB – Northland Basin, NWB - North Wanganui Basin, WB – Waikato Basin, TB – Taranaki Basin.

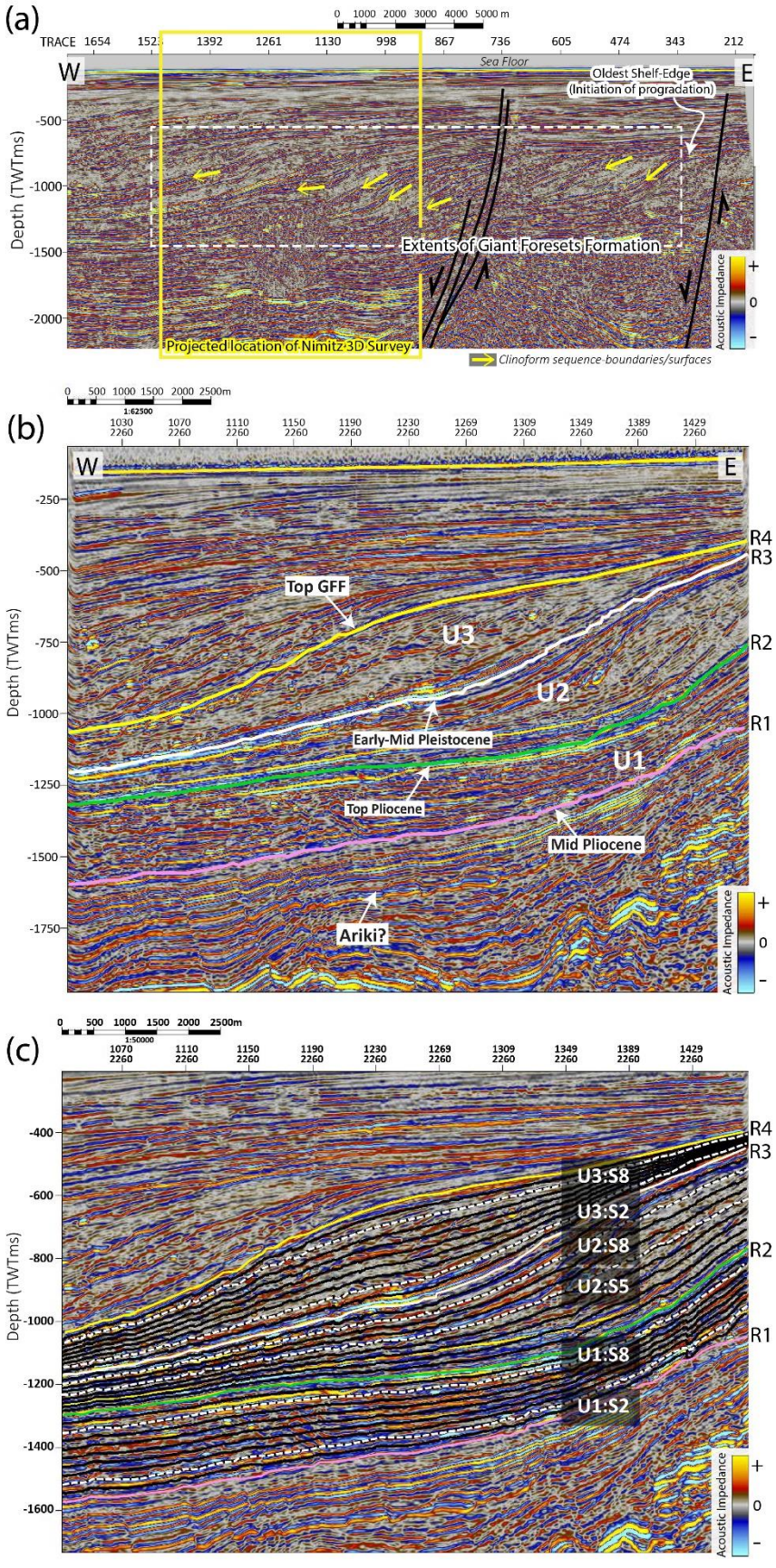
(a)
0 1000 2000 3000 4000 5000 m
TRACE 1654 1523 1392 1261 1130 998 867 736 605 474 343 212
Sea Floor
W
E
Oldest Shelf-Edge
(Initiation of progradation)
Depth (TWTms)
-500
-1000
-1500
-2000
Extents of Giant Foresets Formation
Projected location of Nimitz 3D Survey
Acoustic Impedance
+
0
-
Clinoform sequence boundaries/surfaces
(b)
0 500 1000 1500 2000 2500m
1:62500
W
E
R4
R3
R2
R1
Top GFF
U3
U2
U1
Early-Mid Pleistocene
Top Pliocene
Mid Pliocene
Ariki?
Depth (TWTms)
-250
-500
-750
-1000
-1250
-1500
-1750
Acoustic Impedance
(c)
0 500 1000 1500 2000 2500m
1:50000
R4
R3
R2
R1
U3:S8
U3:S2
U2:S8
U2:S5
U1:S8
U1:S2
Depth (TWTms)
-400
-600
-800
-1000
-1200
-1400
-1600
Acoustic Impedance

Figure B-2. Post back-arc extension progradational features. (a) Cross section (CNL95B-38) showing the 2D transect (See Figure 1a) with the oldest interpreted shelf-edge and the location of the onset of clinoform progradation. The box encloses the lateral extent of the known Giant Foresets Formation within the Taranaki Basin. (b) Cross-section showing the mapped key horizons (four reflectors - R1, R2, R3, R4) of the Nimitz Survey which bound Units 1 – 3 and potential formation tops, supported by both well-ties and literature (O'Leary et al., 2010) (b) A zoom-in of the mid-section of Figure 2b showing stratal slices generated within the units and the dashed, labeled slices used for surface horizon interpretation. See Figure S1 for the a larger uninterpreted version of the seismic line.

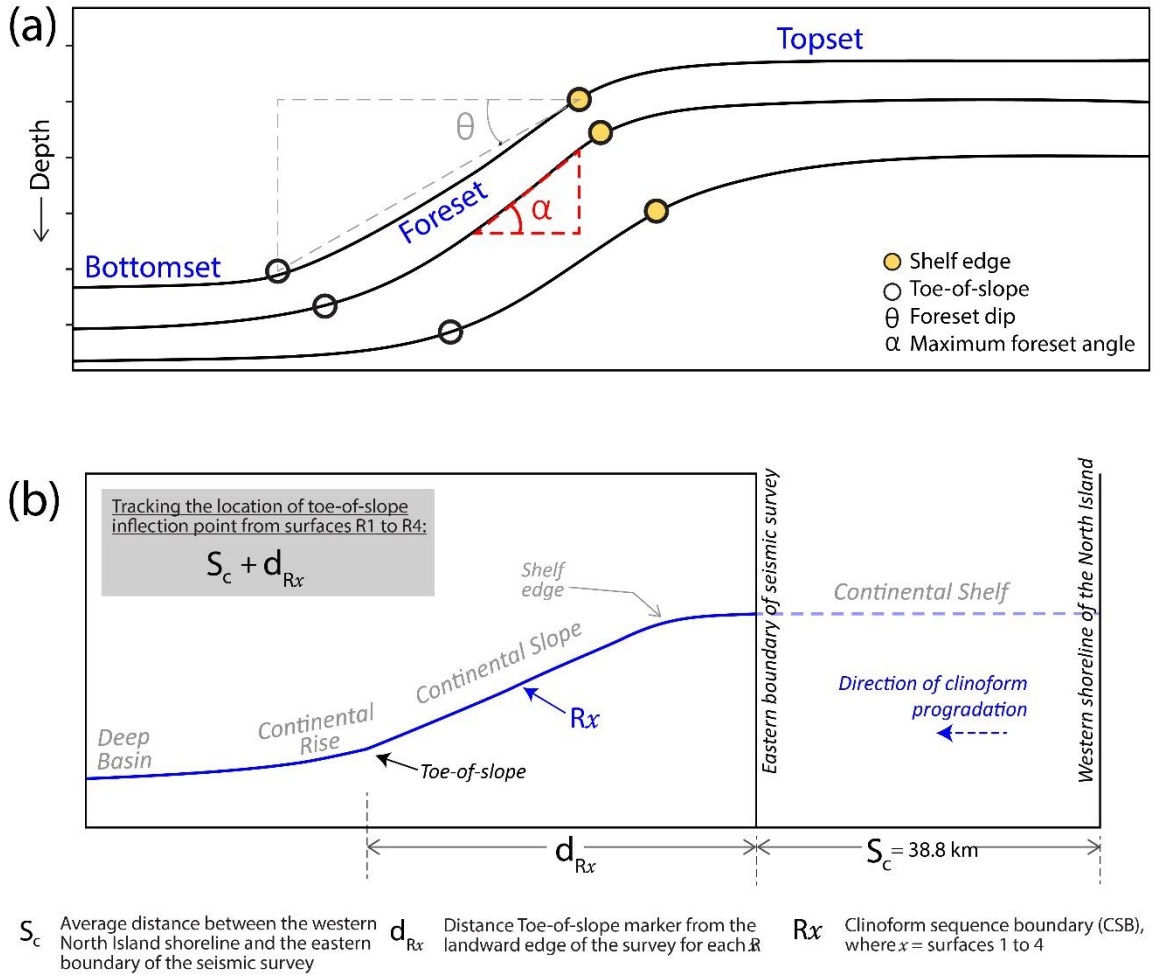

Figure B-3. Measurement of the clinoform sequence boundary structure. (a) Schematic diagram illustrating the geometrical elements associated with progradational clinoform systems. We utilized the angular parameters α (maximum foreset angle, measured along the reflector surface) and θ (foreset dip, measured from the shelf edge to the toe of the slope) to quantify the clinoform geometries across the study area. (b) Schematic diagram showing the scheme used in this study to the track the migration of the continental margin over time. The average distance of the survey from the New Zealand cost is represented by the parameter S_c, and the distance of the toe of slope markeris represented by the parameter d_{Rx}. We evaluate the changes in the location of rise-basin transition over four clinoform sequence boundary surfaces (R1 to R4).

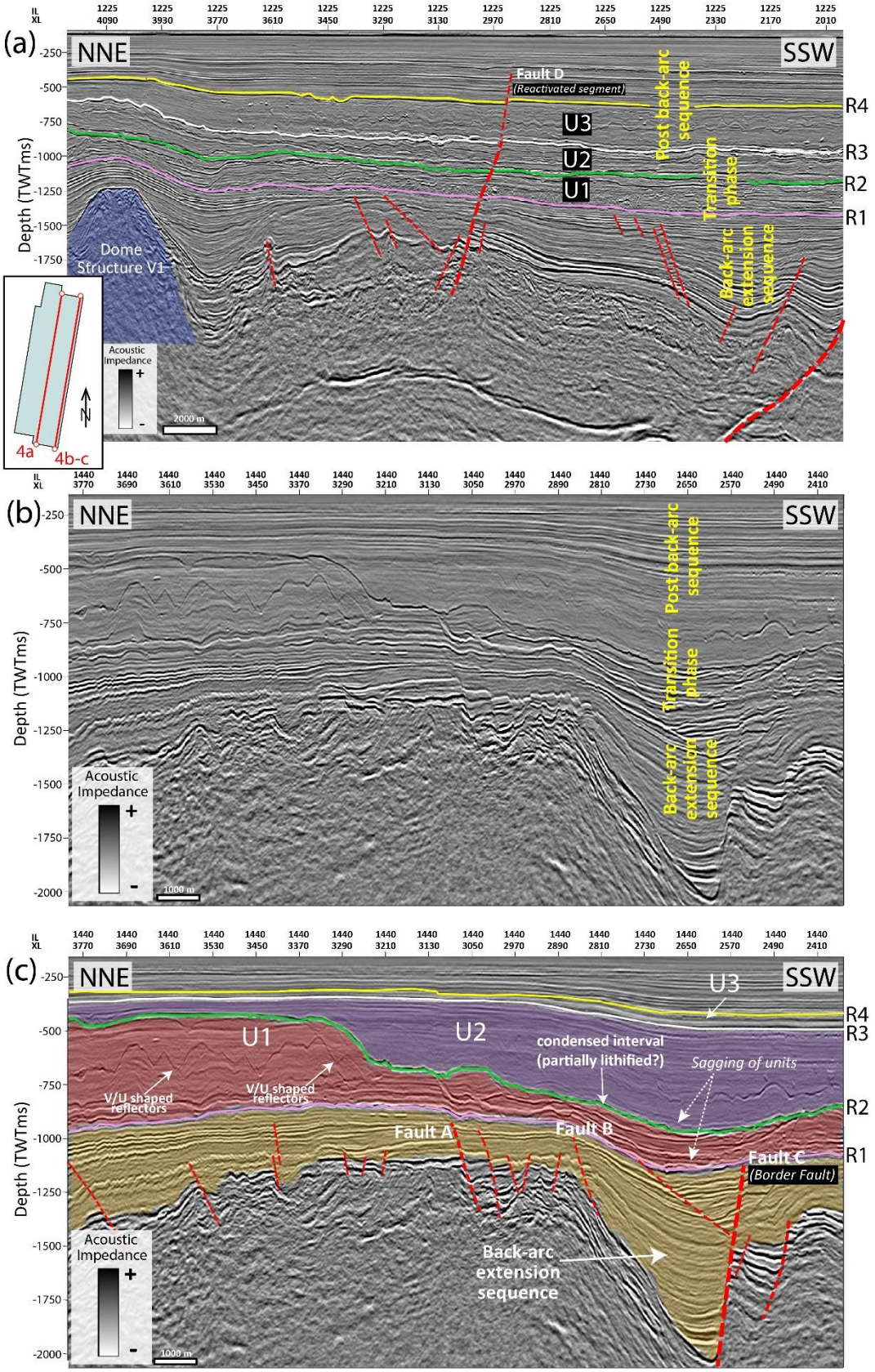
(a)
NNE
SSW
Fault D
(Reactivated segment)
U3
U2
U1
R4
R3
R2
R1
Post back-arc sequence
Transition phase
Back-arc extension sequence
Dome Structure V1
Depth (TWTms)
Acoustic Impedance
2000 m
4a
4b-c
(b)
NNE
SSW
Post back-arc sequence
Transition phase
Back-arc extension sequence
Depth (TWTms)
Acoustic Impedance
1000 m
(c)
NNE
SSW
U1
U2
U3
R4
R3
R2
R1
condensed interval (partially lithified?)
Sagging of units
V/U shaped reflectors
V/U shaped reflectors
Fault A
Fault B
Fault C
(Border Fault)
Back-arc extension sequence
Depth (TWTms)
Acoustic Impedance
1000 m

Figure B-4. Subsurface structure and sedimentary sequences. (a) Inline (IL 1225) cross-section across the survey showing a dome-shaped shaped structure within the back-arc interval (blue polygon). Units 1-3 are also interpreted, bounded by the horizons R1, R2, R3, and R4. (b) An uninterpreted inline (IL 1440) cross-section across the seismic survey. (c) Interpretation of the cross section in Fig. 5b showing the mapped horizons and the tectonic features that influence the shape of the progradaing sequences, together with V and U shaped reflectors. Colored polygons highlight the thickness of the units and the interpreted condensed section (surface R2). The sagging of the units in the central-south domain are potential results of differential compaction due to the underlain syn-rift sequence. See inset in Fig. 4a for the locations of the cross-section transects.

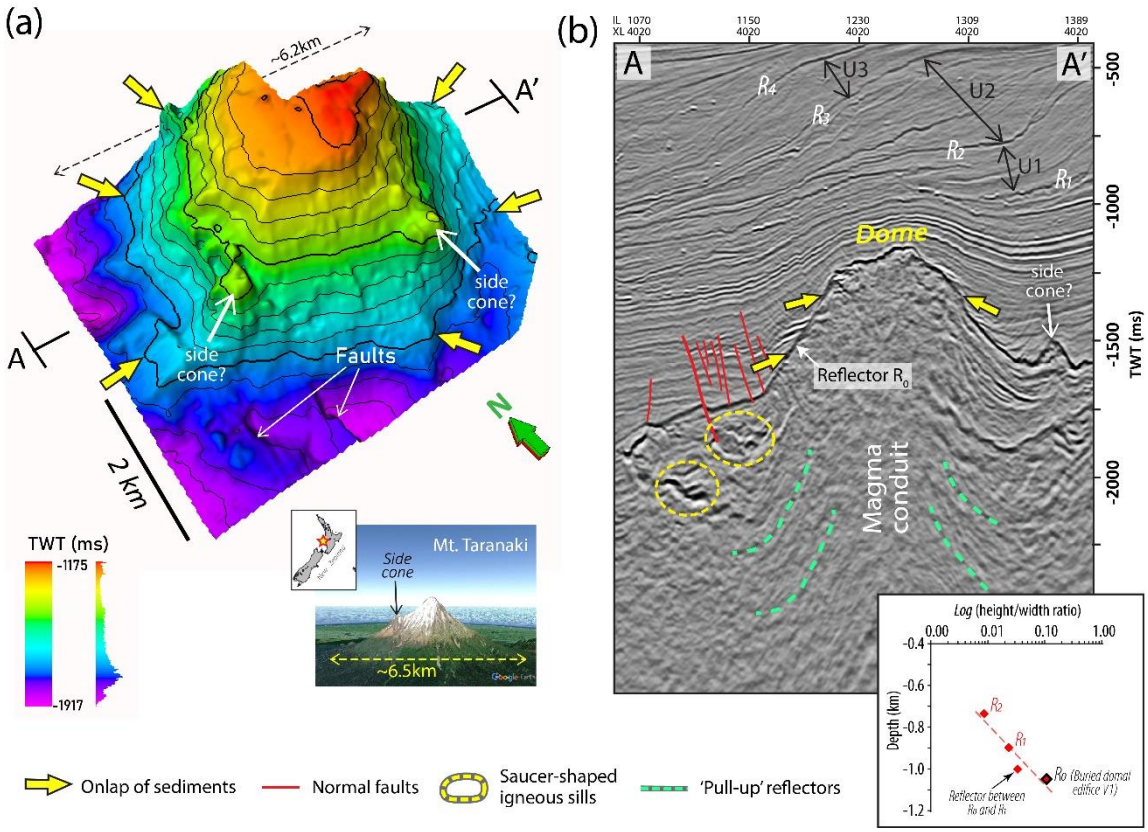

Figure B-5. Miocene back-arc dome-shaped structures in the study area. (a) 3-D perspective view of the largest dome-shaped structure (Volcano V1 in Fig. 1b) in the northern part of the Nimitz seismic survey. We interpret the structure to be a volcanic edifice of the Mohakatino Volcanic Complex (MVC), with a diameter of ~6.2km, emplaced during the Miocene back-arc extension tectonics in the region. *Inset:* A modern day analogue, Mt. Taranaki, located further southeast of the study area, which is similar in dimensions to the intepreted dome shaped structures. (b) Crossline (XL 4020) seismic section showing the strong, high amplitude reflector associated with the top of the dome-shaped structures, the associated features at depth, and the distinct packages of prograding clinoforms at shallower depths above the dome structures. *Inset:* Plot showing a systematic (log-linear) variation of height/width ratio of buried seamount and overlying folds with shallowing depth.

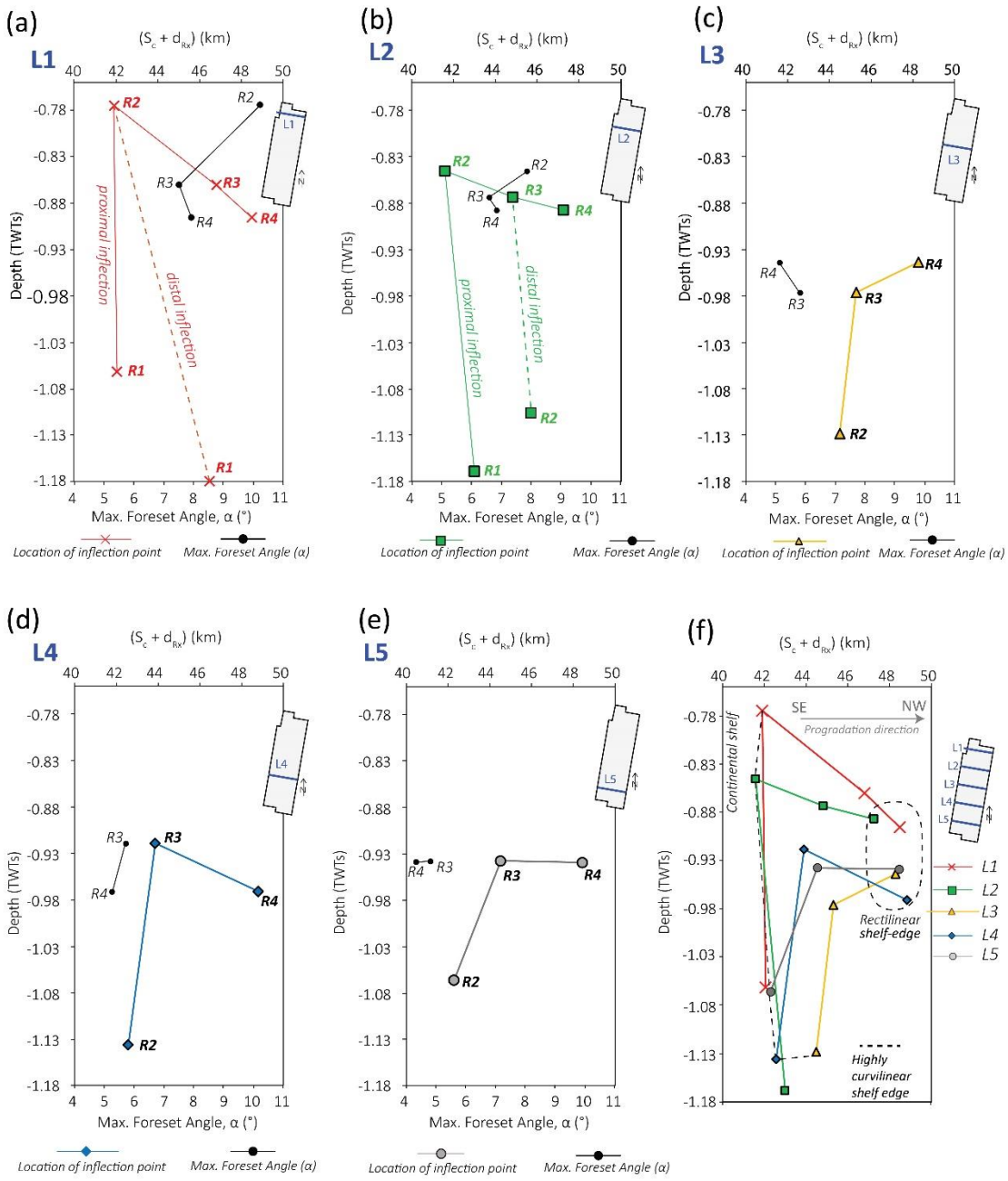
(a)
L1
(b)
L2
(c)
L3
(d)
L4
(e)
L5
(f)
(S$_c$ + d$_{Rx}$) (km)
Depth (TWTs)
Max. Foreset Angle, α (°)
proximal inflection
distal inflection
R1
R2
R3
R4
Location of inflection point
Max. Foreset Angle (α)
SE
NW
Progradation direction
Continental shelf
Rectilinear shelf-edge
Highly curvilinear shelf edge
(g)
(h)
Distance from shoreline
Depth
Progradation Style A
Progradation Style B

Figure B-6. (a-e) Plots of depth (TWTTms) vs (S_c + d_{Rx}) for surfaces R1 to R4, measured in 6 km-spaced cross-sections L1-L5 along the survey. The plots are overlaid with the measured maximum foreset angle (α) on each section. The location of each of the profile transects is shown in the seismic survey map at the top-right corner of the plots. See Figure 3b for more details on the measured parameters. (f) Grouped plot depicting the changes in the strike oriented geometry and location of the shelf edge from surfaces R1 to R4. The clustering of the encircled-dashed points, represent the greatest uniformity of the prograding margin (and hence the shelf-edge) in relatively recent geologic time, and the connected dashed points, represent the highest curvilinear geometry of the prograding margin of a relatively older succession. (g-h) Two types of progradational styles (Progradational Style A and Progradation style B) based on the S_c+d_{Rx} versus depth (in time) trends observed in (a, b & d) and (c & e).

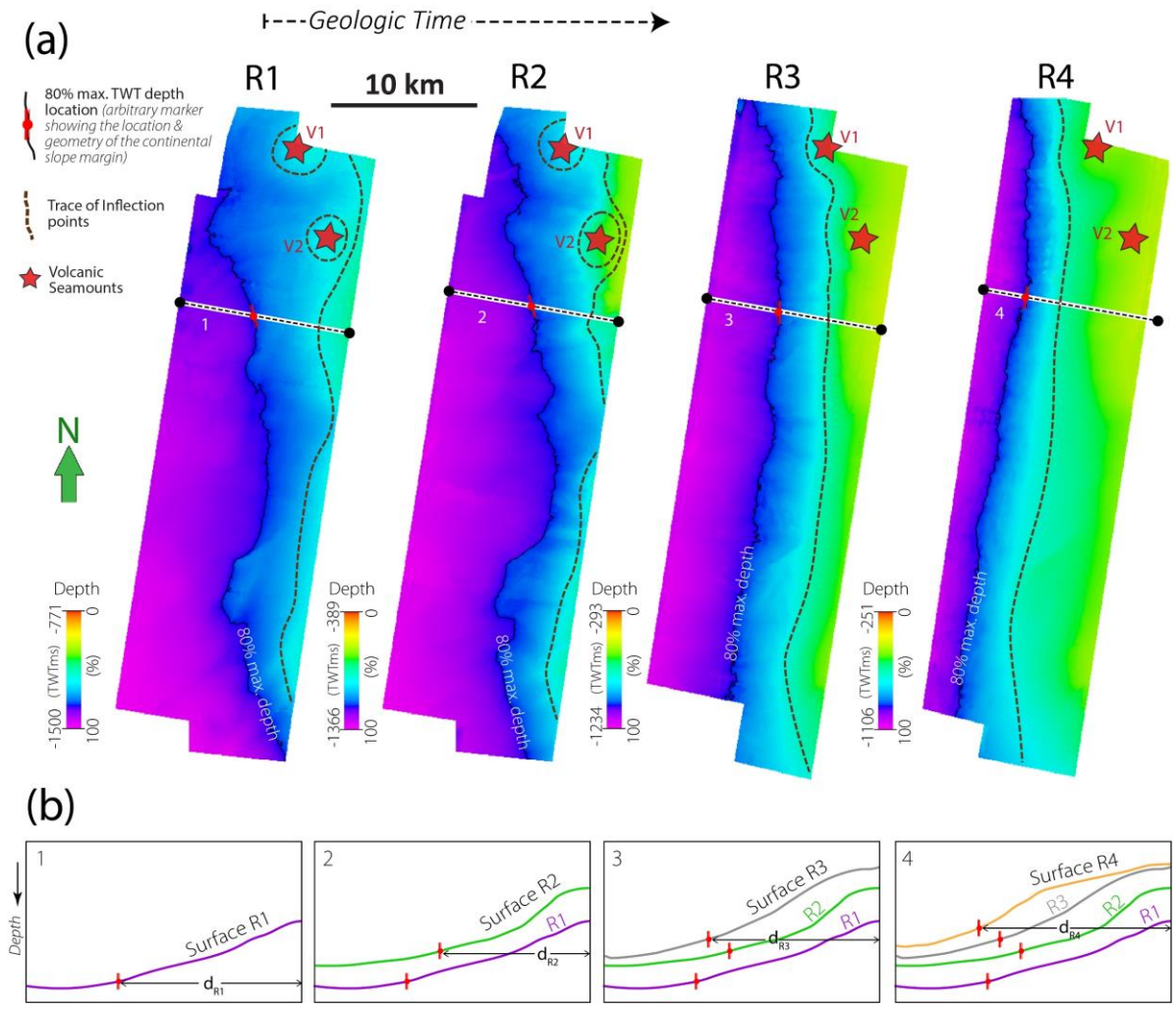

Figure B-7. Spatio-temporal changes in the location and geometry of the Continental Slope Margin in the post-extension sequences. (a) Surfaces R1 to R4 showing the changes in the location and plan-view geometry of the toe-of-slope inflection across the survey. The surfaces are mapped on Two-Way-Travel time. The volcanic seamounts are located and tracked with respect to each surface (red stars). The influence of the volcanic edifices are most significant on the deeper horizon surfaces (R1 and R2). A max. depth contor line is used to further represent the geometry of the continental slope margin. (b) Representative interpretation cross-sections showing the migration toe-of-slope inflection point over time. See Figures 3b and 6a-f for more details on the quantification of the spatio-temporal location and geometry of the toe-of-slope inflection points.

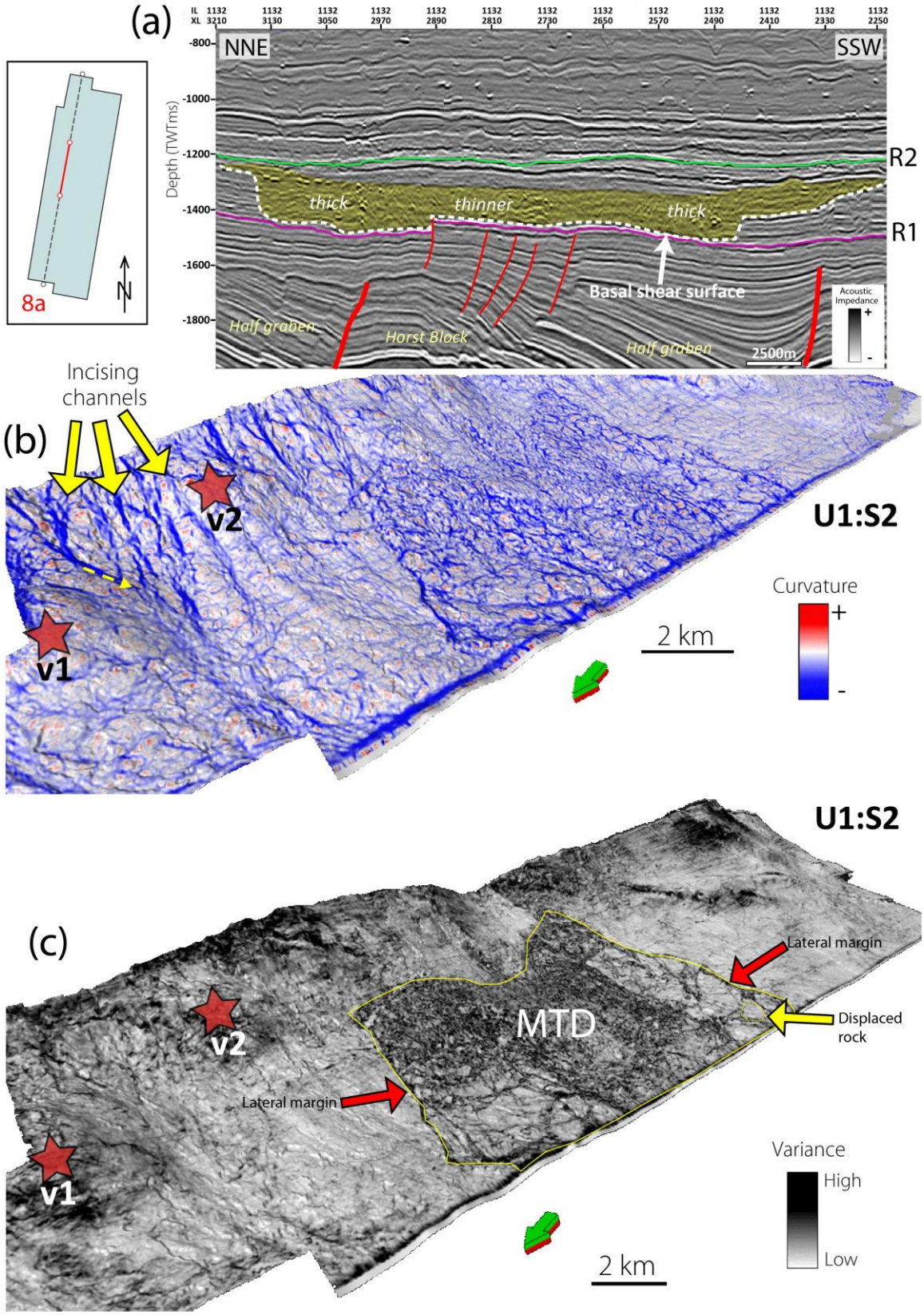
(a)
NNE
SSW
Depth (TWTms)
thick
thinner
thick
R2
R1
Basal shear surface
Half graben
Horst Block
Half graben
2500m
Acoustic Impedance
8a
N
(b)
Incising channels
v2
v1
U1:S2
Curvature
2 km
(c)
U1:S2
MTD
Lateral margin
Displaced rock
Lateral margin
v2
v1
Variance
High
Low
2 km

Figure B-8. Spatial distribution of progradational system elements in the post-rift sequences. (a) Cross-section showing a chaotic mid-high amplitude seismic package in the post-rift sequence (orange polygon), interpreted as a mass transport deposit (MTD) and its basal shear surface truncating continuous parallel reflectors. (b) Perspective view of a deeper surface (U1:S2) (See Figure 2c) within Unit-1 interpolated with the negative structural curvature attribute, revealing channel like features feeding into the basin. The yellow block-arrows show the convergent flow direction of closely spaced channels incising into an over-steepened slope in the northern domain, overlaying the location of the buried paleovolcanoes. The yellow-dashed arrow indicates SW flow of an incising channel feature over one of the two volcanic seamounts, eventually converging into a general westward direction (c) Perspective view of the same surface in Fig. 9b interpolated with the variance attribute, showing the MTD in the central part of the study area and its associated features. It is bounded by its lateral margins, and follows a northwest-westward erosional trend.

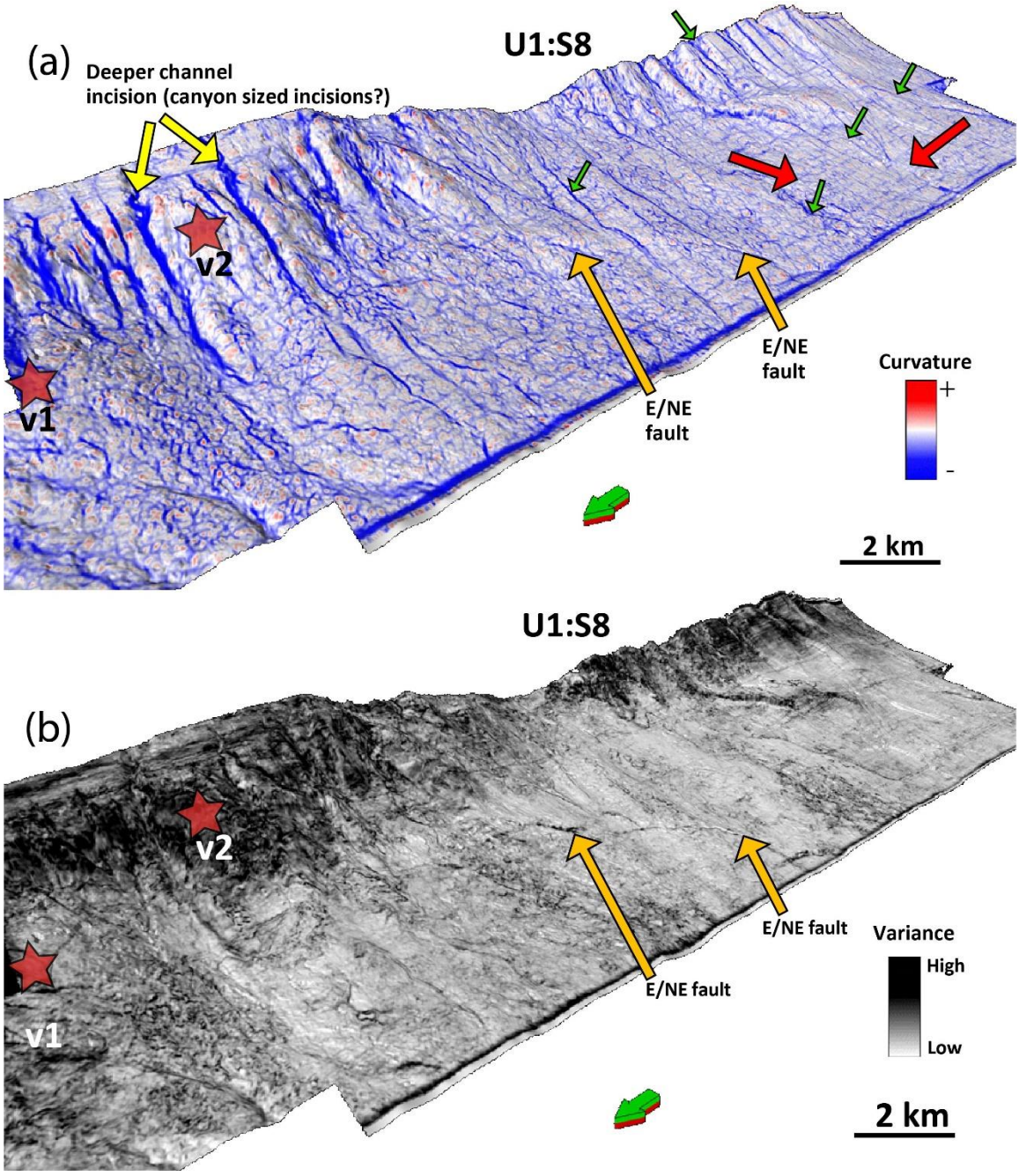

Figure B-9. Perspective view from the NW, of a shallower surface within Unit-1 (S8) interpolated with (a) negative structural curvature, and (b) variance seismic attributes. The images show the dominance of wider incising channels, as compared to Fig. 8b along the shelf-edge and onto the continental slope within the northern domain of the seismic survey where the igneous bodies are located (red stars). Green arrows point and more channel like features in the central and southern domain, that are either linked to more submarine canyons or gullies. Red arrows point an area where the channels are difficult to interpret due to interpolation of the surfaces. It is however

expected that the channels on upper slopes in the southern domain, migrate into the basin. Orange arrows point at an ENE-trending fault

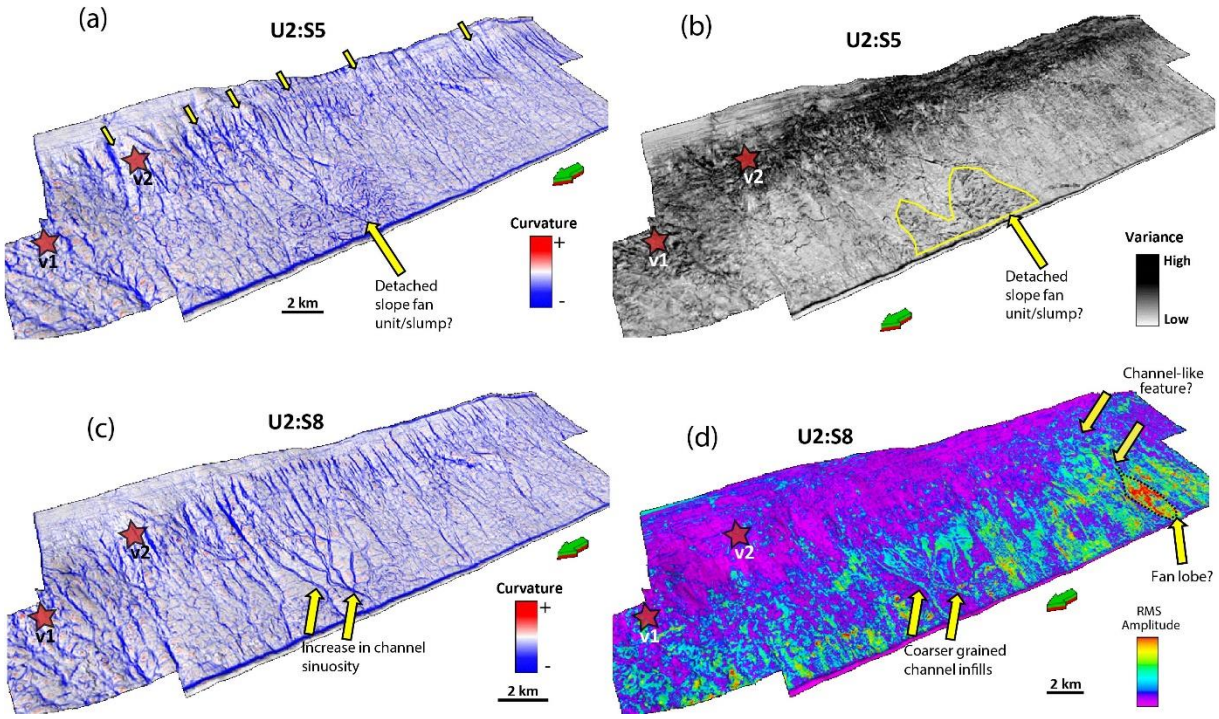

Figure B-10. (a - b) Perspective views of an intermediate-depth surface within Unit-2 (S5) co-rendered with (a) curvature, and (b) coherence surface attributes. The yellow block arrows point to the increase in the frequency of submarine channels across the survey and a potential detached slope fan/slump in (a) & (b). (c – d) Perspective views of the shallower Unit-2 surface (S8), co-rendered with (a)negative structural-curvature, and (d) RMS Amplitude seismic attributes. (c) indicates the event of sinuous channel-like features and (d) highlights high RMS geometrically linear features of potentially coarser-grained channel infills and an interpreted submarine fan lobe with high anomalous RMS amplitude values.

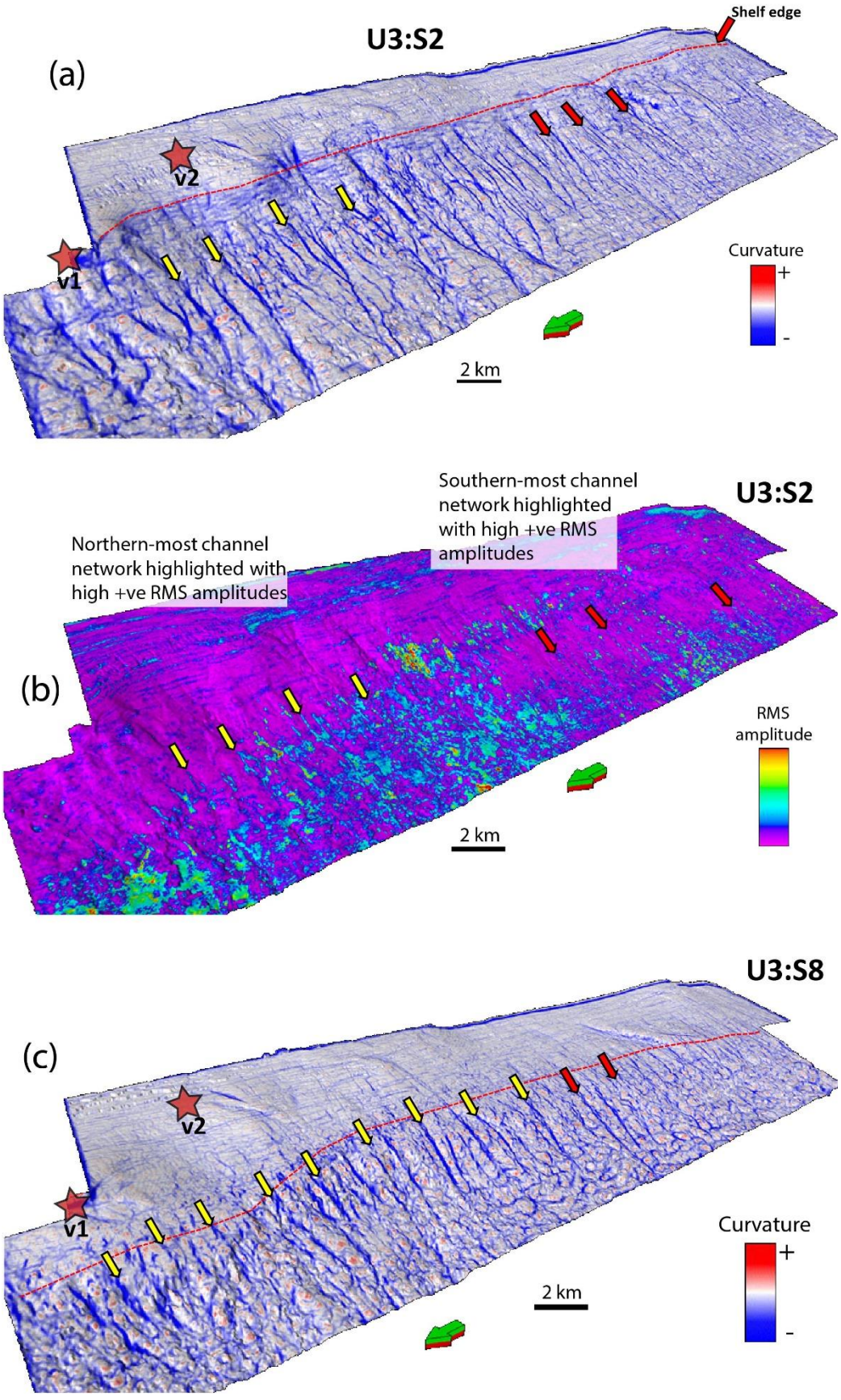
(a)
U3:S2
Shelf edge
v2
v1
Curvature
+
-
2 km
(b)
U3:S2
Southern-most channel network highlighted with high +ve RMS amplitudes
Northern-most channel network highlighted with high +ve RMS amplitudes
RMS amplitude
2 km
(c)
U3:S8
v2
v1
Curvature
+
-
2 km

Figure B-11. (a – b) Perspective views of a deeper surface (S2) within Unit-3 co-rendered with (a) curvature, and (b) RMS Amplitude seismic attributes. The dashed-red line represents the location of the shelf-edge at that point in time. The yellow block arrows point to the increase in frequency of interpreted submarine gullies in the northern domain across the survey into the southern domain indicated by the red block arrows. The linear geometry of these submarine channel features is revealed by the high RMS amplitude values, and as aforementioned are likely filled with coarser grained sediment (c) Perspective of the shallower surface S8 within Unit-3 co-rendered with curvature attribute. Channel frequency continues to increase as the observed shelf edge migrates northwest/westward across the basin.

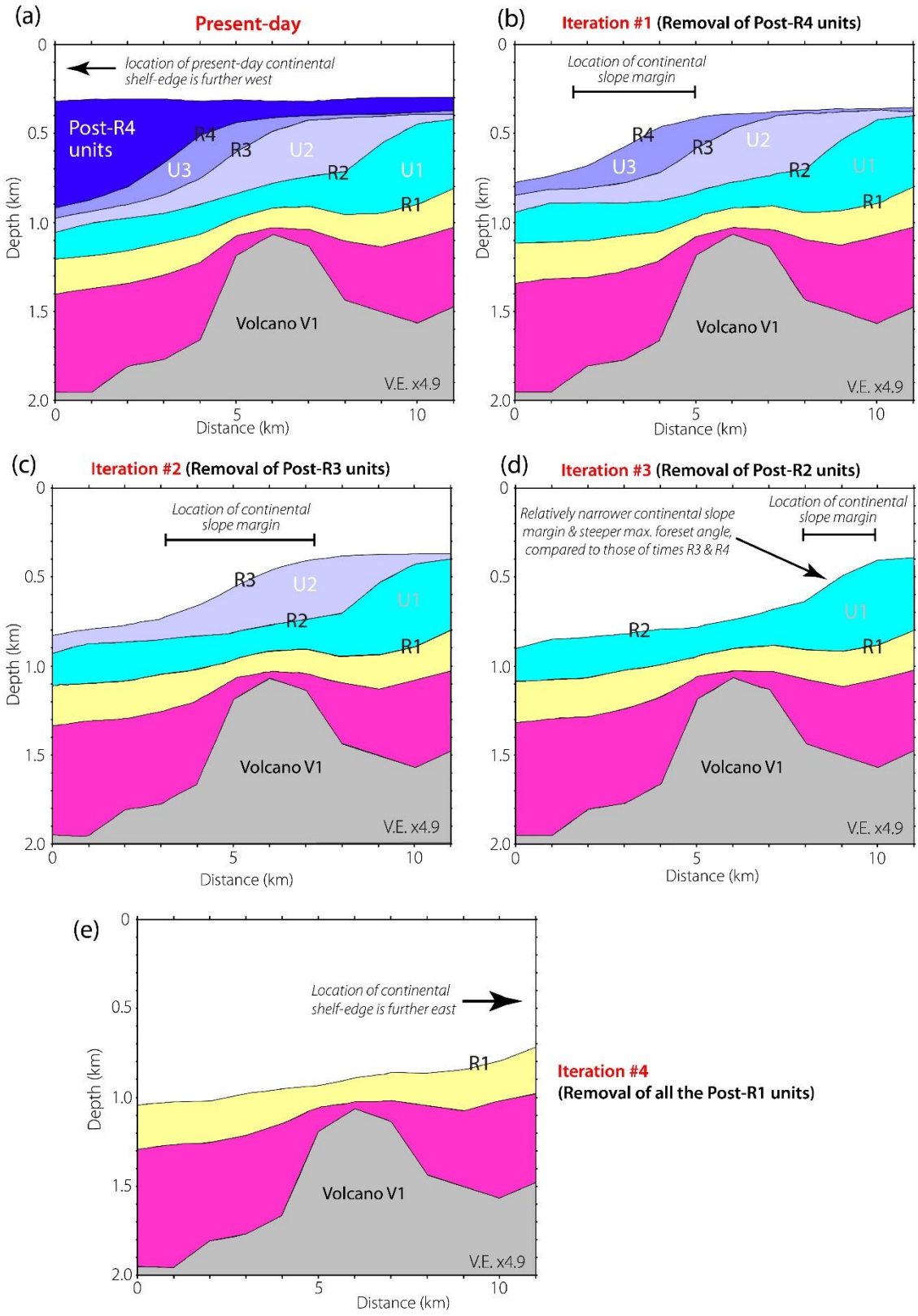
(a)
Present-day
location of present-day continental shelf-edge is further west
Post-R4 units
R4
R3
U2
U3
R2
U1
R1
Volcano V1
V.E. x4.9
Depth (km)
Distance (km)
(b)
Iteration #1 (Removal of Post-R4 units)
Location of continental slope margin
(c)
Iteration #2 (Removal of Post-R3 units)
Location of continental slope margin
(d)
Iteration #3 (Removal of Post-R2 units)
Relatively narrower continental slope margin & steeper max. foreset angle, compared to those of times R3 & R4
Location of continental slope margin
(e)
Location of continental shelf-edge is further east
Iteration #4
(Removal of all the Post-R1 units)

Figure B-12. 2-D decompaction model of the northern domain. (a - e) Cross-sections showing the sequential decompaction models for each of the major clinoform packages of interest. The sections show that the most significant influence of differential compaction about the volcanic edifice occurred at Time R2, with minor influence at time R1 and R3 as well as the position of the migrating slope margin with time. See Figure S2 for depth converted seismic cross section that was used to generated the present day model seen in 12a.

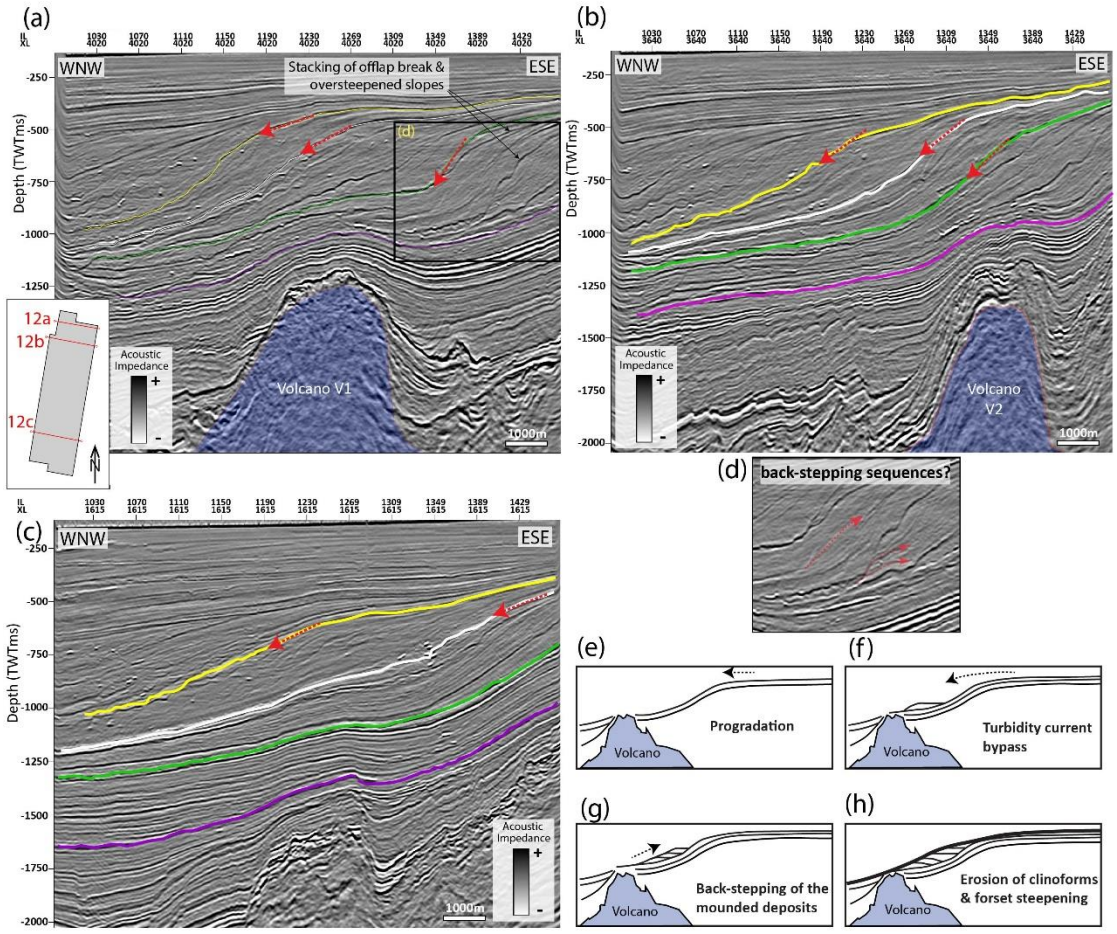

Figure B-13. Buried volcanic massifs and the overlying post-rift sequences. (a - b) Cross-sections in the northern domain of the seismic survey, showing the stacking of the offlap breaks and oversteepening of the foreset slopes above the buried paleovolcanoes. Dominant oversteeping in observed in the older surfaces (R1-R2) primarily in (b). (c) Cross-section in the southern domain of the seismic survey showing clinoforms with gently dipping progradational clinoforms and little- to no disturbance of underlain volcanics. (d) Zoom-in of 13b, highlighting short, weak amplitude reflectors subparrelel to the clinoform surfaces, that may indicate backstepping seismic facies (e-f). Cartoons illustrating the interpreted mechanisms of clinoform development, the backstepping process and the effects of oversteepening of the shelf margin, imposed by a buried volcanic mound (after Johnston et al., 2010).

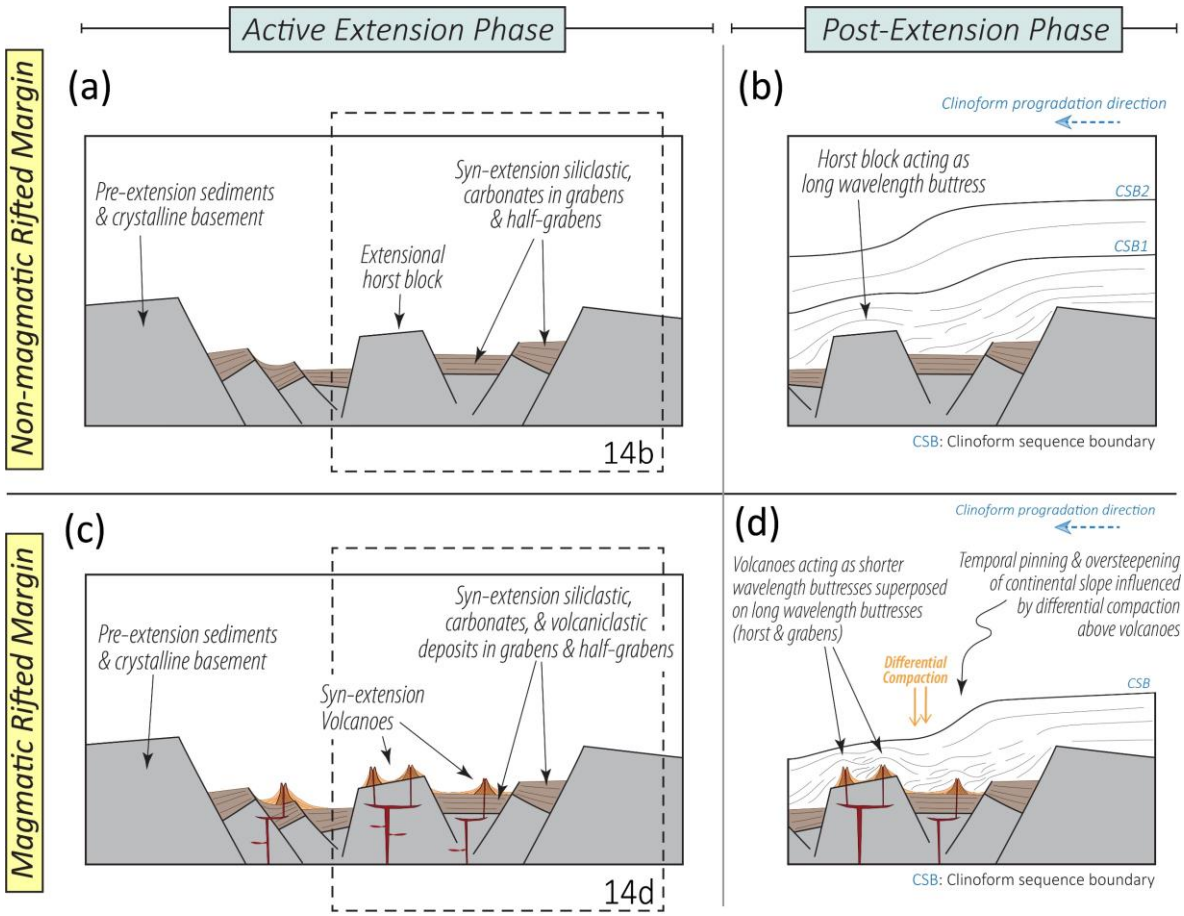

Figure B-14. **Implications for magmatic and non-magmatic continental margins: Example of rifted margins.** Cartoon showing a conceptual comparison between the geometries of prograding sequences in post-extension phases within magmatic and non-magmatic rifted continental margins, with an emphasis on differential compaction influencing clinoform geometry above the volcanic mounds.

APPENDIX C

MASS TRANSPORT DEPOSIT OR COMPLEX CHANNEL SYSTEM? A CASE STUDY OF THE 3D NIMITZ SEISMIC SURVEY, TARANAKI BASIN, NEW ZEALAND

Roberto Clairmont and Heather Bedle

The University of Oklahoma, School of Geosciences

This section was published online on 20 November 202, in SEG journal Interpretation, Special section: Interesting features seen on seismic data

https://doi.org/10.1190/INT-2020-0034.1

Geological Feature: Braided Channel System

Seismic Appearance: Splayed structurally controlled feature, with internally abundant, continuously lineated patterns on horizon slice

Alternative Interpretations: Erosional scour

Features with similar appearance: Mass Transport Deposit

Formation: Whenuakura

Age: Pleistocene – Recent

Location: Offshore Taranaki Basin, North Island, New Zealand

Seismic data: Nimitz 3D Seismic Survey. Obtained by Origin Energy Ltd and reprocessed by authors

Analysis tools: Variance and curvature attributes

ABSTRACT

The Taranaki Basin is well known for studies examining the seismic stratigraphy, depositional and erosional features, and tectonic frameworks linked to the New Zealand (NZ) continent. We have examined a “funny looking thing” (FLT) that we associate to be consistent with that of a braided channelized system. We observe this feature within the 3D Nimitz survey, located in the northern Taranaki Basin, off the western continental coast of North Island, NZ. The FLT occurs within Quaternary deposits of the Whenuakura Formation, which are interpreted to reflect shelfal topset sediments. It is underlain by the Giant Foresets Formation of Pliocene to Pleistocene age, which are described as large-scale progradational and aggradational continental successions that migrated west to northwest in a basin-ward direction. It comprises a shelf-to-slope succession of claystone to siltstone with argillaceous sandstone in-tervals defining an overall coarsening-upward succes-sion. The FLT within the Whenuakura Formation is characterized by chaotic facies in cross section, which shares characteristics with potential mass-wasting events. However, further analysis using seismic attributes improved the spatial and stratigraphic architecture of the FLT, which favored a complex channelized system interpretation over a mass transport deposit complex.

SEISMIC DATA

The 3D Nimitz Survey was acquired using the ship, Pacific Titan, owned by Swire Pacific Offshore, and operated by Compagnie Générale de Géophysique (CGG). It covers an area of approximately 432 km^2 with a recording length of 6500 ms. The sampling rate is recorded at 2ms and crossline and inline interval dimensions have a measurement of 12.5 meters and 25 meters respectively. With a dominant frequency of ~ 45Hz measured within the area of interest and an average velocity of 1710 m/s between the top of the log at 454.6 meters and a Mean Sea Level datum (O’Leary et al., 2010), the vertical resolution for this shallow area is ca. 10 m.

APPEARANCE IN SEISMIC DATA

Seismic characteristics of MTDs (Mass Transport Deposits)

Mass Transport Deposits (MTDs) are common geological components found globally in the stratigraphic record of ancient and modern deep marine settings. They are gravity-induced events comprising of the downslope transportation and redeposition of remobilized sediments (Moscardelli et al., 2006; Dugan and Stigall, 2010). They can be triggered by rapid sea level fall, seismicity, gas hydrate destabilization and high sedimentation rates (Moscardelli et al., 2006; Moscardelli and Wood, 2008; Dugan and Stigall, 2010; Rusconi, 2017). Distinct seismic characteristics associated with mass transport deposits/complexes, help in their identification within seismic data. Frey-Martinez (2010) examines four geological features important for identifying MTDs (i.e. the; basal shear surface, internal architecture, headscarp and toe region). The basal shear surface is an erosional plane along which sediment traction decreases, and movement of mass downslope is identified in seismic cross section via truncation of parallel/subparallel reflectors (Bull and Cartwright, 2010; Frey-Martinez, 2010). The internal architecture of MTDs are generally characterized by chaotic/disturbed seismic facies with a wide range of seismic amplitude responses from low-to-high (Moscardelli et al., 2006). The head escarpment is the highest section of the slope (likely the shelf-break region) where the erosional event initiates, experiencing extensional forces that generate listric faulting (Frey-Martinez, 2010). The toe region represents the lower-slope extent of the MTD, where sediment accumulation creates thickening of the deposits in the stratigraphic section compared to the feature's proximal region, and can be identified in seismic cross section by minor imbricate thrusts and folds (Frey-Martinez, 2010). Compressional thrust faulting within the MTD can also be identified by low coherence and linear discontinuous grooving, that trend perpendicular to flow direction (Bhatnagar et al., 2019).

Due to the lateral extent of the seismic volume, limiting full coverage of the FLT, we utilize a couple of these common geological elements to aid in associated MTD interpretation.

Seismic characteristics of complex channelized systems

Many studies utilize seismic interpretation methods to explore ancient and modern deep-marine channelized systems (Wescott and Boucher, 2000; Kolla et al., 2007; Janocko et al., 2013; Berlin, 2014) to identify the complexities in the processes that shape their depositional styles and the observed architectural elements. Along cross sections, these systems can be described by a list of seismic elements including u and v shaped facies of valley incision into the underlying strata, the occurrence of a high amplitude erosional base (Kolla et al., 2007) and a chaotic channel infill seismic signature (Berlin, 2014).

FUNNY LOOKING THING

In cross-section, the ~3km wide FLT shows a pattern of internally deformed, partially chaotic seismic facies with low-mid-high seismic amplitudes, and lateral truncation via the base of the FLT, of the underlying parallel strata (Figure C-3). V/U shaped seismic facies describing channel incision can be interpreted within the FLT, correlating with similar seismic facies identified below the FLT (Figure C-3a). From time slices, it is evident that the FLT consists of very low positive to low negative seismic amplitude responses, which have splayed curvilinear-like architectures (Figure C-3b). Comparison to cross-sections shows these curvilinear-like features reflect the channel incisions and have widths ranging from 100-170m. Similar channel-like features outside the FLT boundary are observed a little to the southwest and can be compared to for further analyses (Figure C-3b).

SEISMIC ATTRIBUTES

Further characteristics are obtained using seismic attributes, e.g. seismic attributes: structural curvature and variance. The curvature attribute, a 2D second-order derivation of inline and crossline structural components, can aid in identifying channel geometry. The structural positive curvature (k1) reflects dome shaped features, whilst the negative curvature (k2) reflects valley/bowl-shaped features (See Figure C-4) (Chopra and Marfurt, 2007). The schematic gives a clear representation of how k1 and k2 curvature attributes are co-located with the lateral geometrical changes across the channel's axis (Figure C-4b). Structural positive curvature clearly corresponds to the 'dome-shaped' banks/levees on either side of channel, whilst the negative structural curvature corresponds with the 'valley-shaped' channel incision (Figure C-4a). The variance attribute, measures the unconformity in neighboring signal traces, and as such can identify abrupt changes across edges (Randen et al., 2001). As such, it can assist in identifying sudden discontinuities in the seismic response.

Evidence for mass transport deposit

The next step in our analyses, involves the interpretation of unambiguous channel features (Figure 4) and an MTD (Figure C-5) within deeper stratigraphic units observed by Clairmont at al. (2020). The deeper identified MTD shows a very chaotic internal seismic facies, that laterally truncate parallel reflectors (Figure C-5a). The erosional basal-shear surface, separates the overlain chaotic facies with the underlain continuous undisturbed seismic facies. Small-scale thrust faults in addition to few normal faults are visible, indicating the compressional forces associated with the

downslope translation of the sediment mass. The coherent blocky sediment features likely correlate with the observed minor thrust and normal faulting (Figure C-5b). Additionally, time slices (TS – 1368ms) of both the variance and co-rendered structural curvature attributes, further support an overall non-coherent chaotic internal character (Figures C-5b and C-5c), of the ca.14km wide, enclosed body. The more coherent blocky features identified along the variance attribute times-slice can represent more rigid, displaced boulder-sized rock. Clairmont et al. (2020) briefly evaluates the mechanisms that likely contributed to the occurrence and emplacement of this exact MTD, its chaotic internal character and also provides an idea of its longitudinal extent along surface horizons in a shelf-to-basin-ward direction. Curvilinear-like features, typical for the FLT, are not observed this bounded MTD as evident from both variance and structural curvature attributes (Figures C-5b and C-5c) whereas the internal character of the FLT does not show patterns of discontinuity as observed in the MTD (Figures C-5, C-6). However, the FLT shows along cross-sectional strike, a pattern of internal, partially chaotic seismic facies with low-mid-high seismic amplitudes, lateral-truncation of the underlying parallel strata and what we infer may reflect a basal-shear surface or an erosional surface.

Evidence for complex channelized system

Co-rendering of the positive and negative structural curvature attributes of the unambiguous deeper channel system, reveals the lateral changes in shape across the axis of the channel geometry with widths of the confined channel geometries ranging between 80-200 meters (Figure C-4a). Similar characteristics are observed within the FLT (Figure C-6a), although it is difficult to discern the continuity of the positive curvature responses along edges given the complexity of the system. Furthermore, the variance attribute may indicate some apparent chaotic facies, however, we observe that the curvilinear patterns have similar characteristics of the channel-like features to the

southwest, with high variance responses along the edges (Figure C-6b). Interpretations reflecting a channelized system can therefore suggest that the base of the system is an erosional surface.

A COMPLEX CHANNELIZED SYSTEM

In conclusion, our observations reveal a partially weak chaotic internal seismic response (Figure C-3a and C-3b), the absence of fault structures (i.e lack of/no compressional/extensional forces), and that the curvilinear features incise into the underlying strata (Figures C-3a and C-3b) and share more characteristics with the deeper channel syste, than the MTD. The distinct curvilinear features of the FLT do not coincide with the geological elements of observed MTD's (Frey-Martinez, 2010; Bhatnagar et al., 2019; Clairmont et al., 2020) and show a pattern of partially meandering channel type features, growing toward the direction of the modern day NZ coast. We suggest that the observed FLT is a complex channelized system. It is also likely that the bottom limit of the FLT is an erosional base similar to interpretations by Kolla et al. (2007) associated with these systems. Additionally, the amplitude responses of the FLT can differ from other complex channel systems interpreted with seismic reflection data (eg. Kolla et al., 2007), based on its relatively shallow depth. The weak seismic signatures associated with its base and its internal character likely corresponds to limited burial, and hence poor compaction of the strata. Furthermore, deposition of the sediments following the GFF commenced in local Castlecliffian stage (~ 1.63 Mya) and continued to present day, in which the boundary between the GFF and the Whenuakura formation is interpreted as being time-transgressive, with no single continuous event (O'Leary et al., 2010). Although the Quaternary marks the onset of glaciation and associated low-stands, rising sea levels during interglacial periods and associated transgressive systems tract can explain the time-transgressive nature of this boundary. Given that the likely direction of the growth of the channel

system complex was toward the modern day coast and its sudden termination, based on 3D visualization of the seismic data, this may reflect its drowning as sea levels were rising following the last glacial maximum (Miller et al., 2005). This suggests that the complex channel system formed in a subaerial paleo-environment during a glacial low-stand with high fluvial gradients resulting in a braided river pattern. We infer from the seismic geomorphological character that resembles that of a modern day subaerial braided-channel system (eg. Figure C-6 inset: The Brahmaputra River, originating in Tibet).

ACKNOWLEDGMENTS

We would like to take this opportunity to thank New Zealand Petroleum & Minerals and Origin Energy New Zealand Pty Ltd for providing the 3D dataset, Schlumberger and the ASSPI consortium for the licenses offered to the University of Oklahoma. We also thank the Editor Florian Smit, reviewer Andrew Newton and the two anonymous reviewers for their helpful and insightful comments.

REFERENCES

Anell, Ingrid, and Ivar Midtkandal. 2017, The Quantifiable Clinothem - Types, Shapes and Geometric Relationships in the Plio-Pleistocene Giant Foresets Formation, Taranaki Basin, New Zealand. Basin Research **29** (February): 277–97. https://doi.org/10.1111/bre.12149.

Berlin, Taylor Landry. 2014, Channel-Levee Complexes and Sediment Flux of the Upper Indus Fan, LSU Master's Theses. 61.

Bhatnagar, Paritosh, Sumit Verma, and Ron Bianco. 2019, Characterization of Mass Transport Deposits Using Seismic Attributes: Upper Leonard Formation, Permian Basin. Interpretation **7** (4): SK19–32. https://doi.org/10.1190/INT-2019-0036.1.

Bull, S and Cartwright, J. 2010, Small-Scale Insights into Seismic-Scale Slumps: A Comparison of Slump Features from the Waitemata Basin, New Zealand, and the Møre Basin, Off-Shore Norway. In: Mosher DC, Shipp RC, Moscardelli L, Chaytor JD, Baxter CDP, Lee

HJ, Urgeles R, Submarine Mass Movements and Their Consequences. Springer, Netherlands: 257-266. https://doi.org/10.1007/978-90-481-3071-9

Chopra, Satinder, and Kurt J. Marfurt. 2007, Volumetric Curvature Attributes Add Value to 3D Seismic Data Interpretation. The Leading Edge **26** (7): 856–67. https://doi.org/10.1190/1.2756864.

Clairmont, Roberto, Folarin Kolawole, Abah P. Omale, and Heather Bedle. 2020, Controls of Pre-existing Structures on Clinoform Architecture and the Associated Progradational System Elements. Basin Research, July, bre.12487. https://doi.org/10.1111/bre.12487.

Dugan, B. and Stigall, J. 2010, Origin of overpressure and slope failure in the Ursa region, northern Gulf of Mexico. In: Mosher DC, Shipp RC, Moscardelli L, Chaytor JD, Baxter CDP, Lee HJ, Urgeles R, Submarine Mass Movements and Their Consequences. Springer, Netherlands: 167–178. https://doi.org/10.1007/978-90-481-3071-9

Frey-Martínez J. 2010, 3D Seismic Interpretation of Mass Transport Deposits: Implications for Basin Analysis and Geohazard Evaluation. In: Mosher D.C. et al. (eds) Submarine Mass Movements and Their Consequences. Springer, Netherlands: 553-568. https://doi.org/10.1007/978-90-481-3071-9

Hansen, Rochelle J, and Peter JJ Kamp. 2002, Evolution of the Giant Foresets Formation, Northern Taranaki Basin, New Zealand, 17.

Janocko, M., W. Nemec, S. Henriksen, and M. Warchoł. 2013, The Diversity of Deep-Water Sinuous Channel Belts and Slope Valley-Fill Complexes. Marine and Petroleum Geology, **41,** (March): 7–34. https://doi.org/10.1016/j.marpetgeo.2012.06.012.

Kolla, V., H.W. Posamentier, and L.J. Wood. 2007, Deep-Water and Fluvial Sinuous Channels—Characteristics, Similarities and Dissimilarities, and Modes of Formation. Marine and Petroleum Geology, **24,** (6–9): 388–405. https://doi.org/10.1016/j.marpetgeo.2007.01.007.

Miller, K. G. 2005. "The Phanerozoic Record of Global Sea-Level Change." Science, **310,** (5752): 1293–98. https://doi.org/10.1126/science.1116412.

Moscardelli, Lorena, Lesli Wood, and Paul Mann. 2006, Mass-Transport Complexes and Associated Processes in the Offshore Area of Trinidad and Venezuela. AAPG Bulletin, **90,** (7): 1059–88. https://doi.org/10.1306/02210605052.

Moscardelli, Lorena, and Lesli Wood. 2008, New Classification System for Mass Transport Complexes in Offshore Trinidad. Basin Research, **20,** (1): 73–98. https://doi.org/10.1111/j.1365-2117.2007.00340.x.

O'Leary, R, F Luft, and W Mogg. n.d, Offshore Taranaki Basin New Zealand November 2010. 401.

Randen, Trygve, Stein Inge Pedersen, and Lars Sønneland. 2001, Automatic Extraction of Fault Surfaces from Three-dimensional Seismic Data. In SEG Technical Program Expanded Abstracts 2001, 551–54. Society of Exploration Geophysicists. https://doi.org/10.1190/1.1816675.

Rusconi, Francisco Jose. n.d, 3D Seismic Interpretation of a Plio-Pleistocene Mass Transport Deposit in the Deepwater Taranaki Basin of New Zealand: M.S. thesis, University of Arkansas. 62.

Shumaker, Lauren E., Zane R. Jobe, and Stephan A. Graham. 2017, Evolution of Submarine Gullies on a Prograding Slope: Insights from 3D Seismic Reflection Data. Marine Geology, **393**, (November): 35–46. https://doi.org/10.1016/j.margeo.2016.06.006.

Wescott, William A., and Paul J. Boucher. 2000, Imaging Submarine Channels in the Western Nile Delta and Interpreting Their Paleohydraulic Characteristics from 3-D Seismic. The Leading Edge, **19,** (6): 580–91. https://doi.org/10.1190/1.1438662.

FIGURES

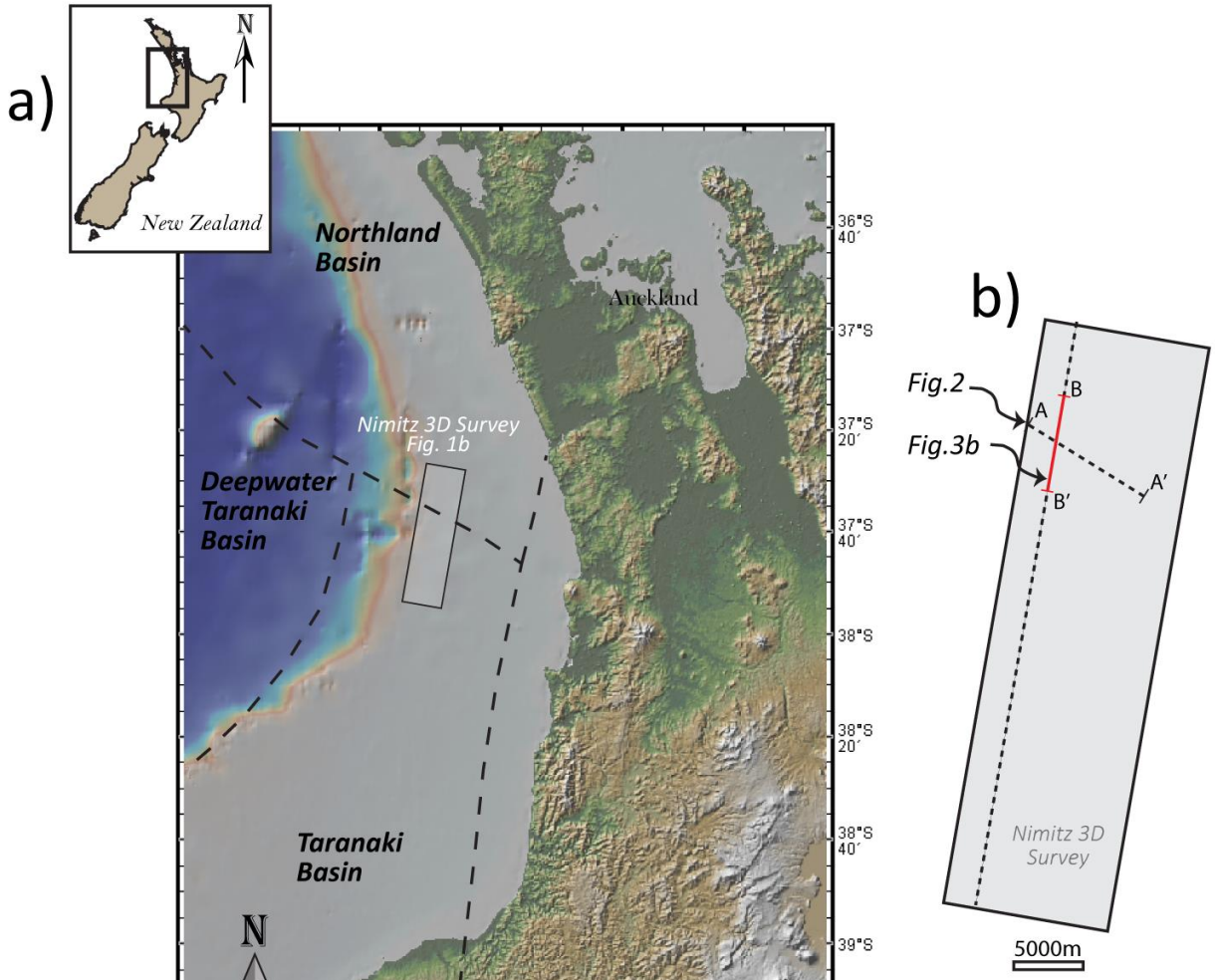

Figure C-1. (a) Topographic map of northern New Zealand showing the Taranaki, deepwater Taranaki, and Northland basins. The location of the study area (Nimitz 3D seismic survey) is shown in the black rectangle. (b) Map of the Nimitz survey with reference lines to the figures interpreted in this paper.

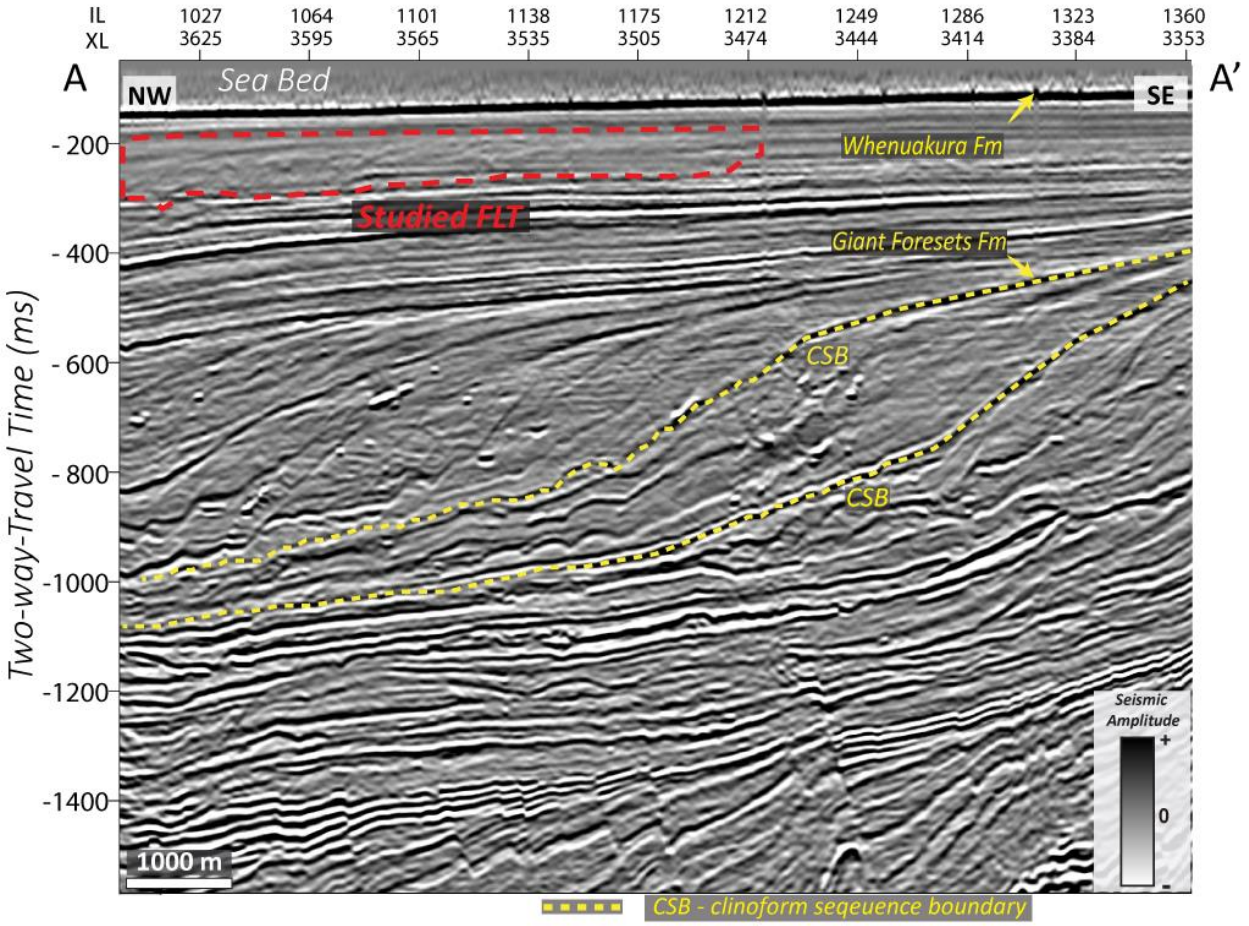

Figure C-2. Composite cross section showing the top of the GFF and Whenuakura Formation according to interpretations by O'Leary et al. (2010). The dashed yellow lines represent the clinoform sequence boundaries describing the dipping shelfto- slope migration of the prograding system. The observed FLT is also highlighted by the enclosed dashed red line, within the Whenuakura Formation, right below the seabed at approximately 300 ms.

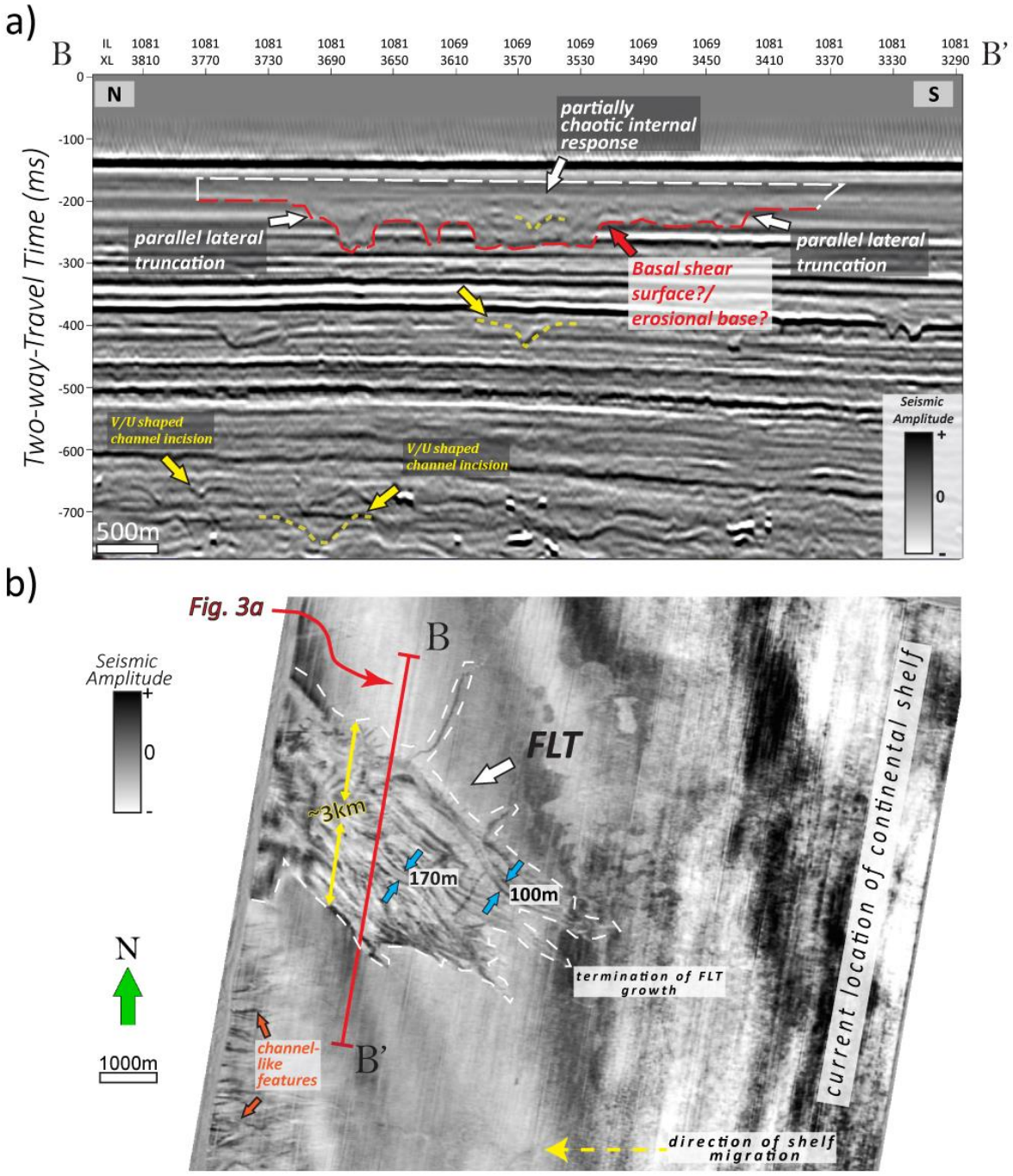

Figure C-3. (a) Interpreted seismic cross section of the studied FLT and initial interpretations associated with MTDs and channel-like features. (b) Seismic amplitude time-slice intersection (TS −224 ms) showing the FLT as a splayed structurally controlled feature (i.e., with an approximate width of 3 km), with internally abundant, continuously lineated patterns. The width of the curvilinear features ranges between 100 and 170 m.

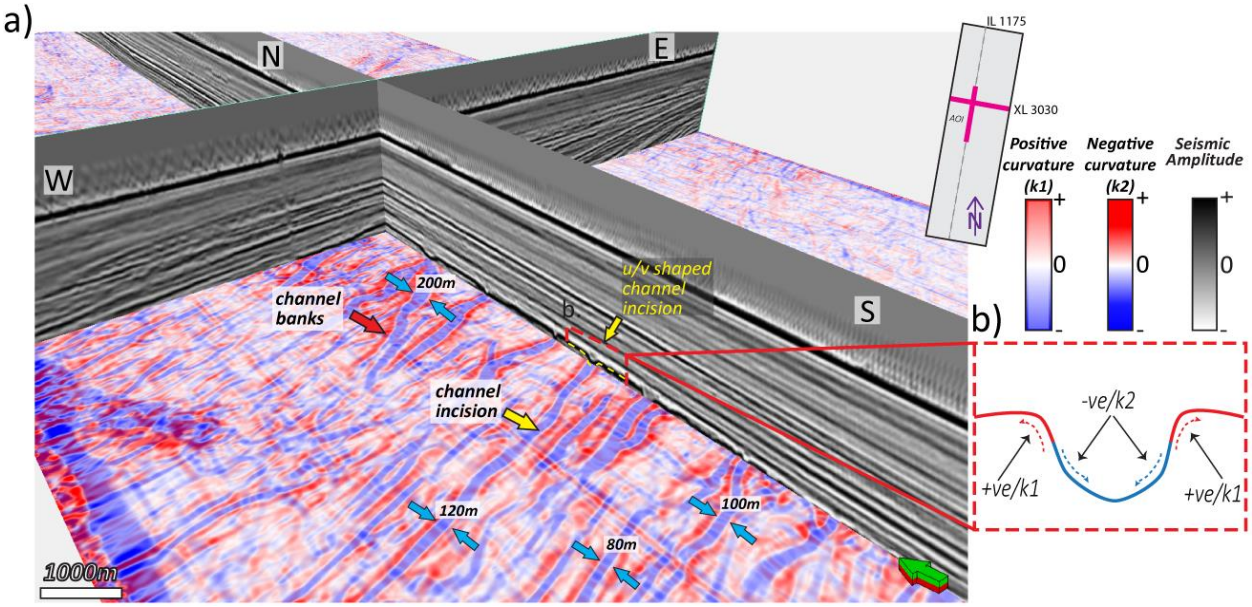

Figure C-4. (a) Corendered positive and negative structural curvature attributes along time slice −408 ms and the seismic amplitude inline (IL 1175) and crossline (XL 3030) sections. The positive structural curvature highlights the banks/levees of the channels, and the negative structural curvature highlights the incisedvalley axes. The widths range from 100 to 200 m. (b) Schematic representing correlating the structural curvature attributes with the shape of the geometry, laterally across the channel.

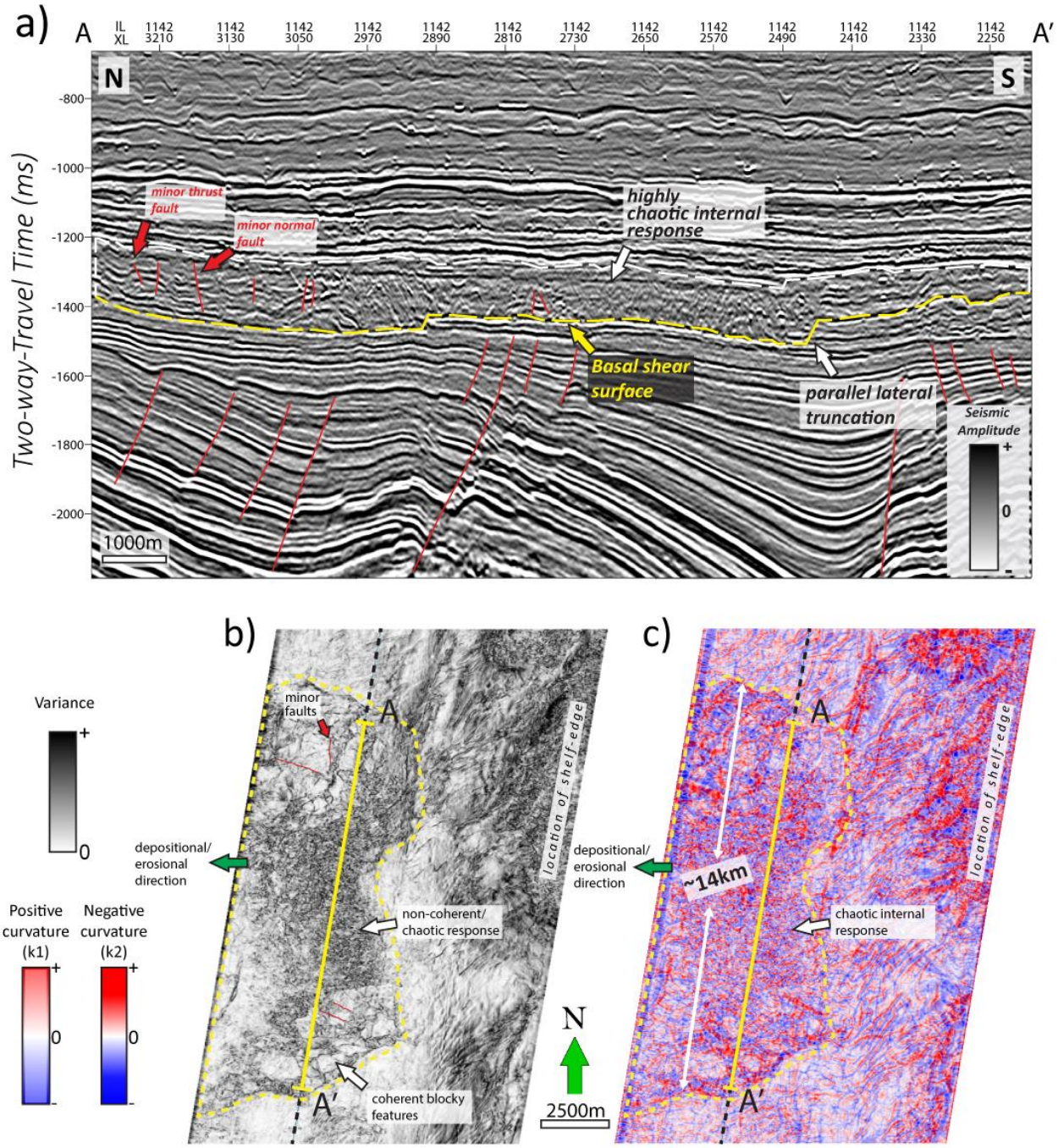

Figure C-5. (a) The observed MTD within deeper strata of the seismic survey. We identify internal chaotic seismic facies with a wide range of seismic amplitude response, a basal-shear surface, and parallel lateral truncation of underlain strata. The red lines indicate faulting within and below the MTD. Time-slice intersection (TS −1368 ms) (b) along the variance attribute indicate a

predominantly chaotic signature of high variance with blocky, low-variance features and (c) corendered positive and negative structural curvatures.

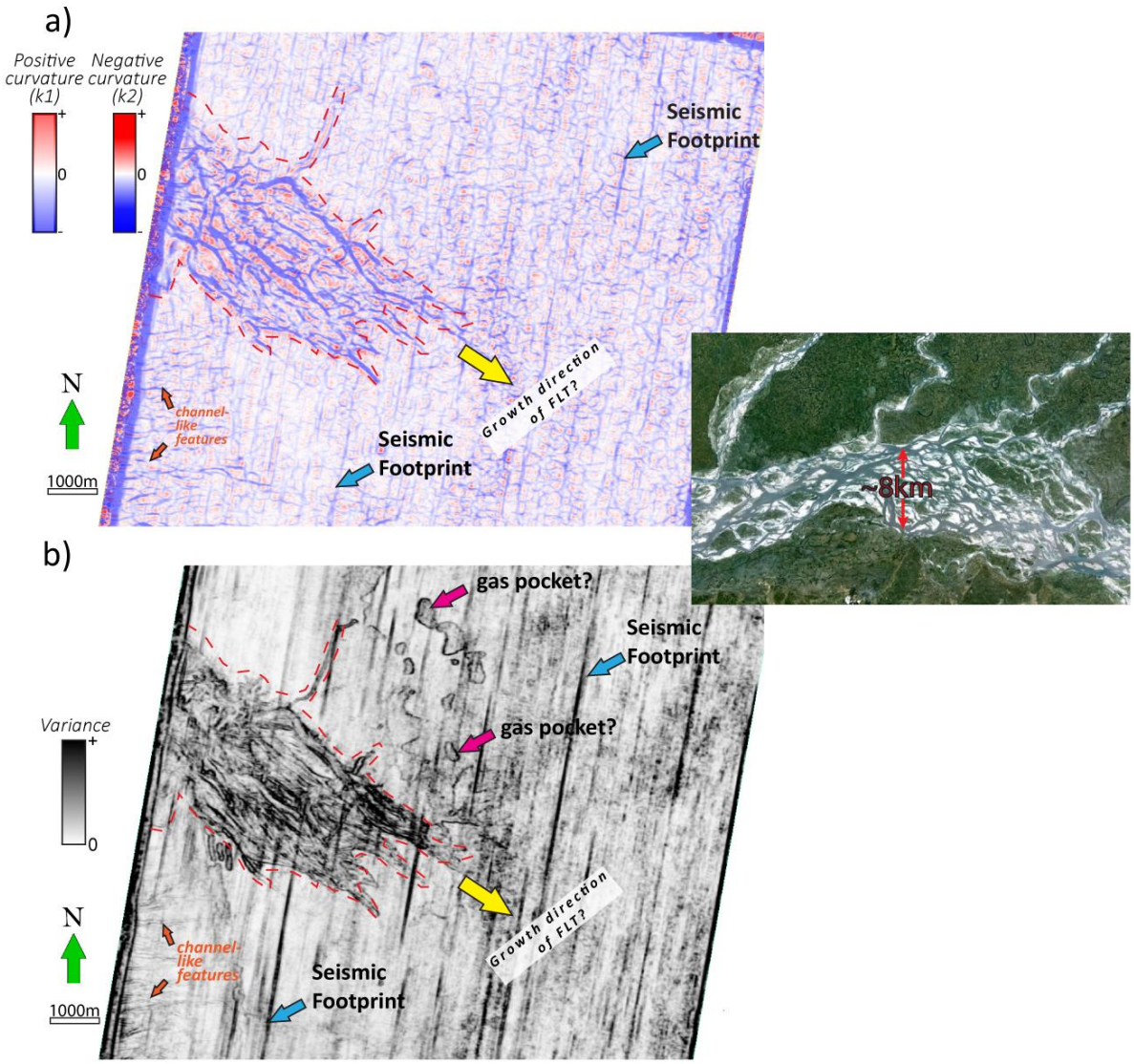

Figure C-6. Seismic attributes (a) structural curvature and (b) variance of the FLT (bounded dashed lines) along the time slice (TS −224 ms). The time slices highlight the edges of the curvilinear features and the absence of a strong discontinuous internal character.We identify other features along the time slice such as potential gas pockets (the magenta arrows) and seismic footprint (the blue arrows). The inset shows a modern-day analogue of a braided river system that originates in Tibet, flowing through India and Bangladesh (Courtesy, GoogleEarth/patternsofnatureblog. com).